

ICES REPORT 15-10

April 2015

Toward Predictive Multiscale Modeling of Vascular Tumor Growth: Computational and Experimental Oncology for Tumor Prediction

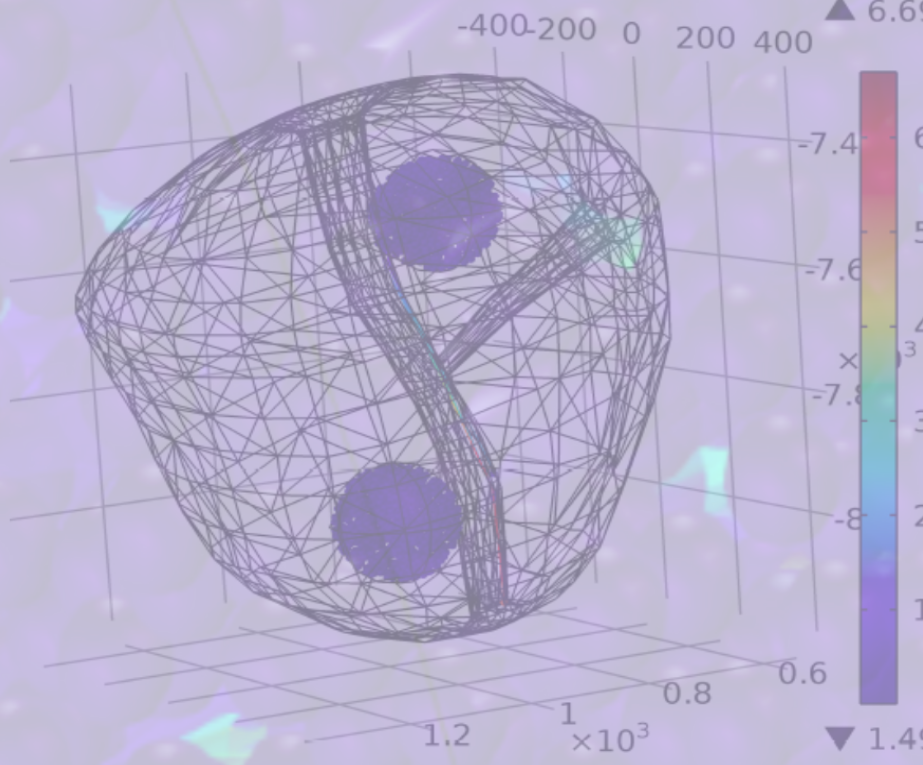
by

ICES Tumor Modeling Group (J.T. Oden, Group Leader)



The Institute for Computational Engineering and Sciences
The University of Texas at Austin
Austin, Texas 78712

Reference: ICES Tumor Modeling Group (J.T. Oden, Group Leader), "Toward Predictive Multiscale Modeling of Vascular Tumor Growth: Computational and Experimental Oncology for Tumor Prediction," ICES REPORT 15-10, The Institute for Computational Engineering and Sciences, The University of Texas at Austin, April 2015.



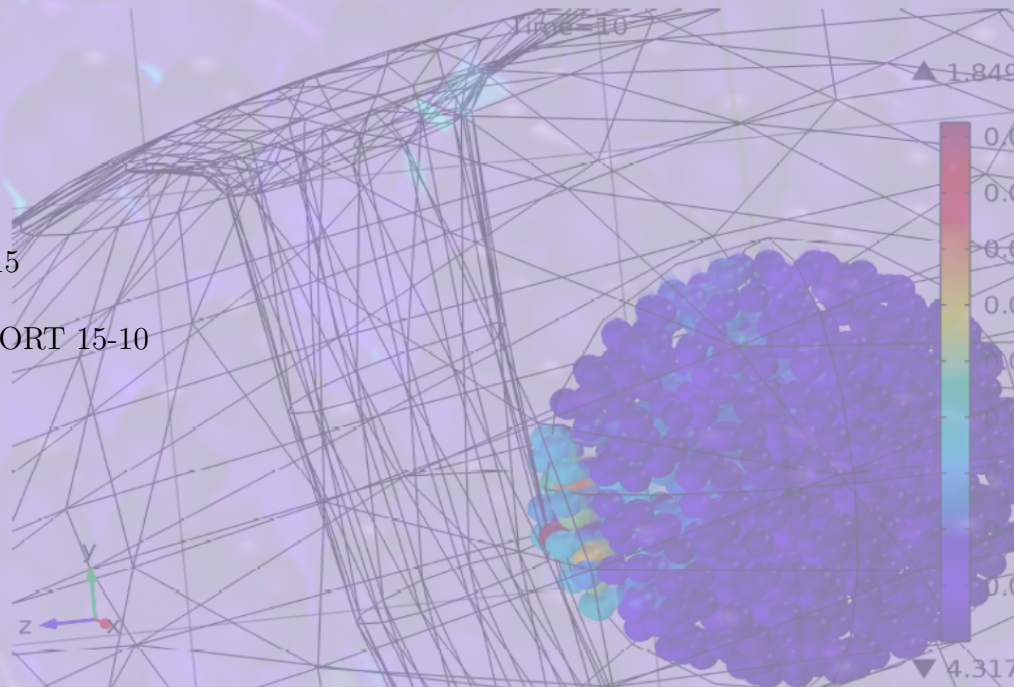
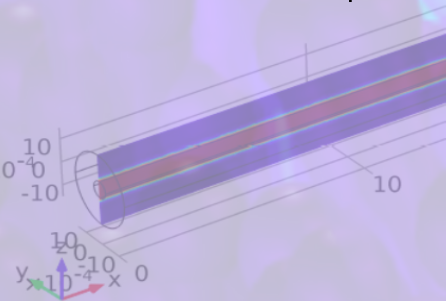
**Toward Predictive
Multiscale Modeling of
Vascular Tumor Growth:**

**Computational and Experimental Oncology
for Tumor Prediction**

**The Tumor Modeling Group
Institute for Computational Engineering and Sciences
The University of Texas at Austin**

Spring, 2015

ICES REPORT 15-10



Cover Illustration: computer simulation obtained by Dr. Sarah Boukhris' dissertation work [20] on modeling cancer cell migration phenomenon along the urethra along which malignant cells escaped from tumors inside a prostate. The tail of each cell represents velocity of cell motion.

Foreword

The ICES Tumor Modeling Group

A research group has been organized at the Institute for Computational Engineering and Sciences consisting of faculty and research scientists from UT Austin, UT MD Anderson Cancer Center (MDACC), and UT San Antonio that is focused on the development, calibration, validation and use of predictive models of tumor growth at all relevant scales. The group has worked on these issues for several years, and made significant progress in developing the principal components of predictive models of tumor growth: multiscale, multispecies models of tumor morphology, a unique laboratory for experimental calibration and validation of parametric models, imaging modalities and inverse algorithms for *in vivo* observations of complex biomedical systems, statistical methods for model selection and validation in the presence of uncertainties and groundbreaking simulations of tumor growth, tumor decline and tumor response to various environments including chemotherapies. An important component of this work is the ongoing development of a laboratory for *in vitro* experiments of the emergence and growth of several types of cancer cells. Another important component is access to imaging data and technologies at MDACC for non-invasive validation of models of tumor growth in relevant organ systems. All of the work is focused on the fundamental problems of developing valid models of tumor growth modeling, determining key model parameters, and predictions of *in vivo* phenomena using imaging data. The scope of the research agenda is broad, including high-fidelity 3D models of angiogenesis, microscopy, and design of experiments to deliver predictions with quantified uncertainties. The work considers models of events at many different spatial and temporal scales, signaling models, cell models, and continuum models of heterogeneous media. This document summarizes our current thinking on tumor modeling and presents open problems that are to be the focus of future work.

This Report

This document has been written and compiled by the ICES Tumor Modeling Group so as to provide an overview of the current status of predictive modeling of tumor growth, to survey relevant literature, and to identify promising areas for future research.

The TMG

- Almeida, Regina C., Ph.D.; Professor and Visiting Scholar, ICES; National Laboratory for Scientific Computing (LNCC)
- Dewitt, Matthew R.; Graduate Research Assistant, Virginia Tech
- Faghihi, Danial, Ph.D.; ICES Postdoctoral Fellow
- Feng, Yusheng, Ph.D.; Professor, UT San Antonio
- Fuentes, David, Ph.D.; Assistant Professor, Dept of Imaging Physics, UT MD Anderson Cancer Center
- Gadde, Manasa; Graduate Research Assistant; UT Austin
- Lima, Ernesto A. B. F., Ph.D.; ICES Postdoctoral Fellow
- Oden, J. Tinsley, Ph.D.; Director of ICES
- Rahman, Mohammad M.; Graduate Research Assistant; UT San Antonio
- Rylander, Marissa Nichole, Ph.D.; Associate Professor, Dept of Mechanical Engineering, UT Austin
- Zhou, J. Cliff; Graduate Research Assistant; UT Austin

Contents

1	Introduction	1
1.1	The Emergence of Predictive Medical Science	1
1.2	Predictive Modeling of Tumor Growth	2
2	Multiscale Models of Tumor Growth	6
2.1	The Hallmarks of Cancer	6
2.2	Mathematical and Computational Models of Tumor Growth	7
2.3	Cellular Automata Models	9
2.4	Agent Based Models	10
2.4.1	An Agent Based Model for Ductal Carcinoma <i>in Situ</i>	11
2.5	Phase-Field and Mixture Theory Models	13
2.5.1	A Six-Species Phase-Field Model of Tumor Growth	15
2.6	Models of Mechanical Stress and Deformation of Anisotropic Vascular Tumor	18
2.7	Signaling Models	23
2.8	Angiogenesis Models	33
2.8.1	A Hybrid Ten-Species Phase-Field Model of Tumor Growth	35
2.9	Stochastic Models	40
2.9.1	A Stochastic Six-Species Phase-Field Model of Tumor Growth	42
2.10	Multiscale Computational Methods and Challenges [50]	44
2.10.1	Proposed Multiscale Modeling Framework	47
3	Model Calibration, Validation and Selection in the Presence of Uncertainties	49
3.1	Parameter Sensitivity	51
3.2	A Bayesian Framework for Calibration, Validation and Pre- diction	52
3.3	Model Selection: Posterior Plausibilities of Parametric Model Classes	53
3.4	The General Bayesian filtering	54
3.5	Example: Selection of Models of Tumor Growth	55
4	Experimental Calibration and Validation of Tumor Growth Models: The Rylander Tumor Engineering Laboratory	58
4.1	3D Solid Tumor Platform	58
4.1.1	Cell Viability, Proliferation and Morphology:	59

4.1.2	Experimental Depictions of Angiogenesis	60
4.1.3	Hypoxia Measurement	62
4.2	Single Channel Vascularized Platform	62
4.2.1	Matrix Composition	63
4.2.2	Cellular Composition	65
4.2.3	Hemodynamics	66
4.2.4	Endothelial Permeability	67
4.3	Dual Channel Vascularized Platform	68
4.4	Surrogate Models of Branching Vascular Networks	70
5	Image Processing: Data Collection for the Validation Scenario, S_V	72
5.1	Image Processing Measurements	74
5.1.1	Histopathology	74
5.1.2	Image Processing	74
5.2	Image Registration	76
5.2.1	Diffeomorphic Registration	76
5.3	Random Forest [37, 91]	79
6	Numerical Algorithms and Parallel Computing	81
7	The Future: Challenges and Opportunities	84
	References	86

1 Introduction

1.1 The Emergence of Predictive Medical Science

Science may be defined as the activity or enterprise concerned with the systematic acquisition of knowledge. But exactly how knowledge is acquired has been the subject of debate for millennia. Aristotle, over 2,000 years ago, more or less put forth the correct answer when he attributed knowledge acquisition to “demonstration and reasoning”, later more sharply described by eighteenth century scholars as the two pillars of science: observation, including experiments designed to acquire and interpret data, and theory, the construction of hypotheses on the causes of natural events based on inductive logic. In the last half century, both pillars have been enormously enhanced by the advent of the computer, leading in recent times to the explosion of big data, data analytics, and bioinformatics on the observation side and high-fidelity computer models and algorithms on the other. So successful have these new technologies been that some say a new pillar of science has emerged: computational science, the multidisciplinary field that uses computer models to predict events and to study and interpret large data sets.

Until very recently, medical science has been heavily weighted on the observational side of science – relying on statistical data as a basis for discovery of causes of disease, the development of various therapies, the design of new drugs, and on explaining many aspects of the complex behavior of biomedical systems. In very recent times, largely over the last decade, a fundamental change has gradually emerged in which computational models have been developed to predict patient-specific behaviors and responses to medical treatment. Brought about by dramatic advances in scientific computing, mathematical modeling, drug design and delivery systems, and mathematical statistics, the new medicine is emerging as a sub-discipline of model-based predictive science, a field realized through the use of high-fidelity predictive models.

The use of the term “predictive science” may, at first, seem to be redundant: has not all science been considered predictive from time immemorial? Is not prediction at the heart of inductive reasoning, a foundational pillar of science itself, involving the development of hypotheses to explain physical observations and then extrapolating those explanations to similar events in the future or in the past? The dramatic advances in computational and computer science over the last two decades have enabled the scientific community to push its prediction capabilities to the limit. The result has been the realization that effective predictive models cannot arise from brute-force

applications of computer models. A host of new technologies must be developed to cope with the inevitable uncertainties in data, in model selection, in model parameters, and, finally, in the target predictions themselves. The term “*model-based predictive science*” has been coined to refer to the body of knowledge essential in making the sophisticated models of complex systems truly predictive. We now know in medical science that new data must be acquired, not to simply indicate trends in large populations of patients, but to inform, validate, and calibrate predictive models.

The role of uncertainties in science is well summed up in the monumental treatise by E.T. Jaynes, *Probability, the Logic of Science*, wherein the interplay between data, theory, and parameters in scientific prediction is made clear. The probability of a physical event, such as the metastasis of cancer cells, can be predicted in a broad statistical sense by traditional diagnostic methods by collecting data from a large number of samples, often leading to a nearly flat probability distribution as indicated in Figure 1.1. In the new medicine, these data may provide priors, the initial information on parameters. A validated predictive model can map parameters into patient-specific data to sharply increase the probability of the likelihood of an event, as suggested in the figure. The term “precision medicine” has also appeared in recently literature to describe these aspects of the new medicine.

The breadth of work on predictive medicine is large and growing and ranges from oncogenic signaling of molecular structures to intra-sculpturing of the genome, stochastic models covering stem cell homeostasis, a spectrum of models ranging from agent-based models to continuum models of cell migration and sprouting angiogenesis. Most exciting in this general area is the acquisition of new experimental methods that will supply missing data needed to make the existing models and new models relevant and, ultimately, more predictive. New experimental setups have been designed, or are in the process of being designed, which are not based on merely collecting big data for diagnostics, but are aimed at collecting data for informing models and determining parameters for patient-specific models of cancer. This new medical science will not abandon the traditional diagnostic-based science governed by observation but will, in fact, exploit the experience and data accumulated to inform and validate parametric models of a wide range of phenomena concerned with cancer.

1.2 Predictive Modeling of Tumor Growth

The last half-decade has seen an explosion in literature on mathematical and computational models of the invasion and growth of tumors in living tissue. Recent accounts on the status of multiscale modeling of cancer have

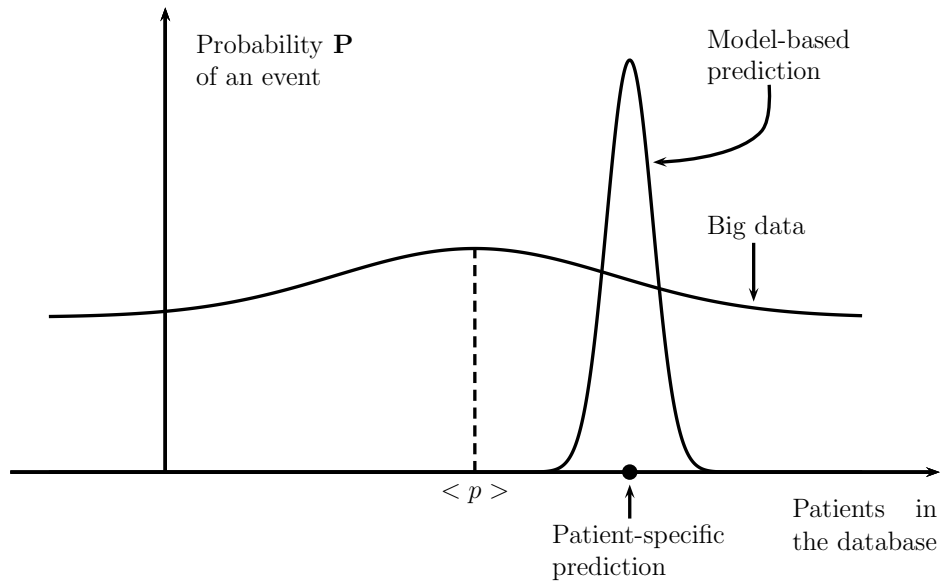


Figure 1.1: The push and pull of observational data and model-based predictions. With big data, statistical information (e.g. mean values and variances) is used to make decisions on large populations of patients. With model-based predictions, parametric computational models are “informed” by the data, making possible increased probability of events for fewer patients - even specific patients when valid models are employed and when one accounts for parameter uncertainties.

been compiled by Deisboeck and Stamatakos [44] and Cristini and Lowengrub [39], the latter listing over 700 articles and 25 literature surveys, some citing early modeling methods going back over a half century, but much of it pertaining to very recent years.

The reasons for this awakening on the great potential of TGMs (Tumor Growth Models) are multifaceted. Firstly, there is increasing consensus in the medical science community on the principal mechanisms leading to various cancer types. The highly-cited *Hallmarks of Cancer*, laid down by Hanahan and Weinberg [57] in 2000 and updated in 2011 [58], provide a broad view of the key biological processes that may be targets of computers simulations. Secondly, progress in understanding the role of genetics in encoding proteins that form phenotypes and molecular alterations at the gene, cell, and tissue level over the last decade have lead to new families of models that could greatly increase our understanding of the origins and growth of cancer and on new therapies to combat it. These advances have lead to a flurry of new multiscale models that depict events at many spatial and temporal scales,

from sub-cellular to cellular to tissue to organ levels (e.g. [39, 44]). Thirdly, and perhaps most importantly, is the gradual emergence of predictive medical science, the body of knowledge rooted in mathematical statistics, probability theory, experimental science, and computing that addresses in depth the actual validity and, equivalently, the predictability of various models in the presence of uncertainties. This vital discipline has come to the forefront because the indispensable data needed to calibrate and validate TGMs has only recently become accessible. Fourthly, the enormous technological and mathematical advances in high-performance computing, in big data analytics and data-intensive computing, in imaging technologies, and in new modeling paradigms, ranging from agent-based algorithms, phase-field models, models of stochastic systems, to molecular models, all have brought into play an arsenal of new tools that have great potential for developing realistic high-fidelity simulations of cancer cell behavior.

Our work, some of which is reviewed in this document, has touched all of these areas. Following this introduction, we describe a class of phenomenological TGMs based on phase-field versions of mixture theory, following [38, 52, 60, 77, 139, 150]. We also describe discrete-cell agent-based models, subcellular models that incorporate molecular-scale signaling, and hybrid multiscale models that attempt to capture events at the subcell-cell- and tissue levels.

The foundations of predictive science, set in a Bayesian framework, are discussed in Chapter 3, together with new algorithms for implementing statistical calibration and validation methods and assessing sensitivity of model outputs to parameters. There we discuss the fundamental questions of model selection; of all the possible TGMs, which are valid and which best fit observational data? The fundamental questions of reliability of model predictions is, unsurprisingly, at the center of research in TGMs.

In Chapter 4, we describe a unique laboratory under constructive designed to provide special data critical to calibrating a large group of TGMs. The TEL (Tumor Engineering Laboratory) is to be the first of its kind, with facilities specifically created to rigorously calibrate and validate models of tumor invasion and growth within the context of predictive medicine - enabling the quantification of uncertainties in model parameters and ultimately in the model predictions themselves.

Chapter 5 summarizes recent advances in imaging processing, non-intrusive data collection, and new sampling algorithms that are invaluable in model validation.

In Chapter 6, we provide a brief exposition on the challenging field of numerical methods for solving the enormously complex models of tumor growth, including parallel algorithms and algorithms for solving stochastic models.

New formulations of robust numerical algorithms are needed to treat the special features and challenges inherent in the structure of many TGMs. Here we also describe extraordinary parallel high-performance computing resources available to the team at TACC, the Texas Advanced Computing Center.

Conclusions, open problems, and future work are discussed in a final chapter.

2 Multiscale Models of Tumor Growth

2.1 The Hallmarks of Cancer

A tumor, or neoplasm, is a mass of tissue that results from any abnormal growth of cells [88]. Tumors can be separated into two categories: benign (not a cancer) or malignant (cancer). The main difference between these two is that malignant tumors may acquire the potential to spread to other parts of the body (metastasis), while benign tumors cannot invade surrounding tissues and may not necessarily be life threatening [62, 88, 93].

During the cell cycle, some mutations may occur; luckily, only a small proportion of these mutations can persist due to the efficiency of the DNA repair mechanisms [62]. Carcinogenesis is a multistage process developed through stochastic proliferation and differentiation from a single cell which has sustained several genetic changes [136]. According to Hesketh [62], between five and fifteen mutations in critical genes are required for the development of cancer. Hanahan and Weinberg [58] were able to summarize eight common traits shared by all, or at least the majority of types of cancer, which are depicted in Figure 2.1

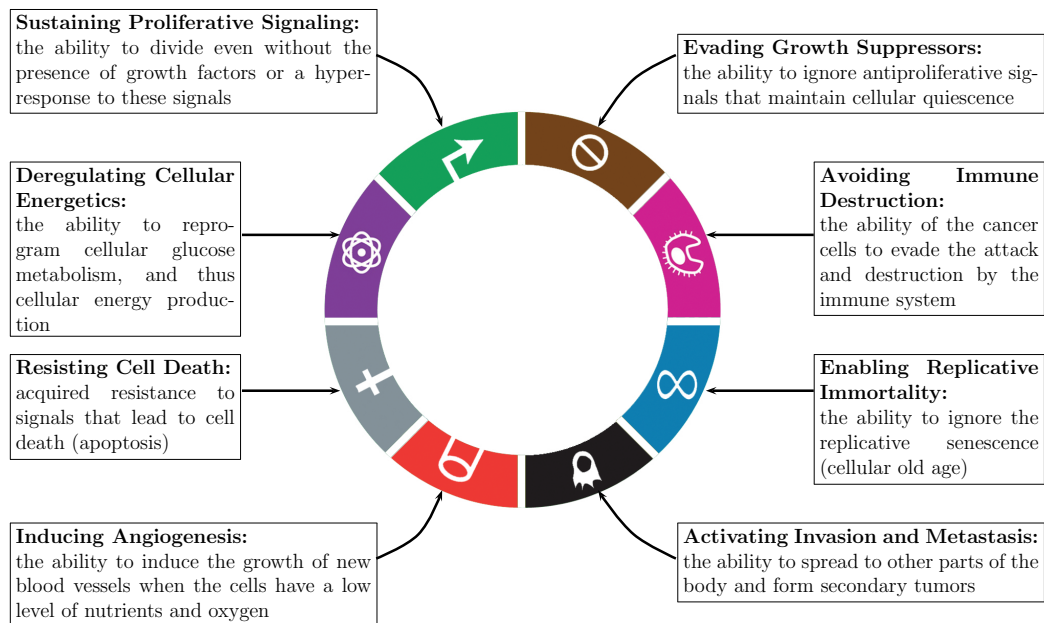


Figure 2.1: The eight hallmarks of cancer discussed in Hanahan and Weinberg [58]. Schematic description inspired by the account in Hanahan and Weinberg [58].

These hallmarks in tumor growth are only possible due to two enabling characteristics: genome instability and mutation and tumor-promoting inflammation. According to Hanahan and Weinberg [58], nearly all cancer contains immune cells present in some density. The immune cells can cause inflammations while trying to eradicate the tumor, that avoid the immune destruction. However, inflammations can help the acquisition of several hallmark capabilities by supplying growth factors, enzymes that contribute to modify the extracellular matrix for the angiogenesis, survival factors that help to avoid apoptosis and other chemicals that can accelerate the mutations in cancer cells. The manifestation of each of the eight hallmarks can occur in different orders depending on the time that each mutation occurs [57, 58].

Tumor growth is also affected by a series of phenomena that occur basically at three scales: subcellular, cellular and tissue level. At the subcellular scale there are phenomena that occur within the cell or at the cell membrane, such as DNA synthesis and degradation, nutrient uptake, activation or inactivation of receptors and regulation of cellular activities. At the cellular level, complex interactions and signaling between cells such as tumor, fibroblasts, and endothelial cells and their matrix occur. Finally, the tissue level phenomena are typical of continuous systems and involve such event as cell migration, diffusion and convection of nutrients, interactions with external tissues, metastasis and others [102].

There is a very complex interplay of various factors within these three scales. Events that happen at a certain scale are related to those that happen at other scales. As an example, the detachment typical of metastasis is directly related to the adhesion properties of the cells [102]. Thus, understanding how events at these different scales are connected and the mechanisms that are behind tumor growth is essential in the development of predictive models of cancer.

2.2 Mathematical and Computational Models of Tumor Growth

The diversity of biological scales involved in tumor growth and the heterogeneous nature of the tumor microenvironment pose substantial modeling challenges. Modeling usually focuses on a series of key biological and mechanical events and associated physical, temporal and biological scales. One feature that differentiates tumor growth models is whether or not they include models of the vasculature [102]. The initial phase of tumor growth (avascular phase) can be studied by laboratory experiments that capture the

first stages of tumor development *in vivo*. In this phase, cells grow into a tumor mass that can achieve a few millimeters in diameter. Cells at the center of the tumor may eventually be deprived of key nutrients and oxygen and are starved and die, forming a central necrotic core [29].

Avascular models are used to describe the early stages of tumor growth. Among the simplest are those which consider the growth of the mass of the tumor as an exponential function such that the cell growth is limitless, since all nutrients and growth factors are available. These types of models can give accurate results for the first stages of tumor growth, but they are not able to reproduce the saturation observed during experiments *in vitro* [102]. A classical way to overcome this drawback is to use a Gompertz function to model the growth rate. This function depicts the exponential growth of the tumor during the first stages and saturation when the number of cells reaches the capacity that the environment can support [4, 82, 94, 95, 102].

Vascular models must take into account the angiogenesis process, the process in which new vasculature structure is formed from existing blood vessels in order to provide the tumor with nutrients. Tumor neovasculature is marked by precocious capillary sprouting, convoluted and excessive vessel branching, distorted and enlarged vessels, erratic blood flow, microhemorrhaging, leakiness, and abnormal levels of endothelial cell proliferation and apoptosis [58]. Tumor induced angiogenesis is a cancer hallmark, and follows the avascular phase when tumor cells are starving for nutrients. Tumor cells become hypoxic due to this nutrient starvation and start to secrete tumor angiogenesis factors (TAFs). The TAFs are responsible for initiating sprouting angiogenesis [90]. The growth factors diffuse from tumor hypoxic cells to the nearby blood vessels and initiate several processes. The endothelial cells (ECs) that form the blood vessel walls are activated by TAFs concentration, inducing them to proliferate and migrate chemotactically towards the tumor [87]. These steps of the angiogenesis process are followed by the maturation of new capillaries, providing structural stability for the new blood network.

Several different forms of models have been developed in attempts to obtain better agreement with experimental results [38, 39, 53, 59, 84, 151]. These are generally divided into three categories: discrete models, continuum models, and hybrid models, which have characteristics of both continuum and discrete models [59]. Discrete models have the advantage of capturing individual cell behavior and interactions among cells, but can be limited by the computational cost [38, 59, 98]. This class of models encompasses cellular automata models and agent based models, and can be used to model interactions between cells that include phenomena such as mitosis, apoptosis and angiogenesis [94, 95]. Continuum models can capture the evolution of the tumor generally involving partial differential equations, disregarding the

behavior of each individual cell [38, 98]. Finally, hybrid models can model the cells in a discrete way as well as other dynamics, such as nutrients dispersion, with differential equations [59, 98]. One example of a hybrid model is that proposed by Macklin et al. [84], where an agent-based model is used to capture cell-cell and cell-basement membrane interactions, and the oxygen is modeled by a reaction-diffusion equation that averages the density of cells at each point to couple the discrete model with the continuum model [39, 84].

2.3 Cellular Automata Models

Cellular automata (CA) are mathematical models that, by well defined rules, simulate complex systems or processes by means of a discrete dynamical system, i.e., time and space are discrete, with a regular spatial lattice in which at any point, each cell has a value, or state, and interacts with neighboring cells. The state of the cell is updated at each timestep based on the previous states of its neighbors using predefined rules.

Several tumor growth models have been developed using the CA framework in order to model cell-cell interactions. Kansal et al. [69] modeled the growth of a specific brain tumor called glioblastoma multiforme (GBM), in which the median survival time for patients was 8 months [28]. Their model overcomes the size limitation imposed by the computational cost by allowing more than one cell at each point of the lattice, which allows the CA model to represent a small tumor with 1000 cells up to 10^{11} cells. It also uses an adaptive grid lattice that allows small tumors to be simulated with greater accuracy, while still allowing the tumor to grow to a large size [69, 70]. The model accounts for the effects of mechanical confinement pressure on the chance of how the proliferative cells divide. Simple three-dimensional CA models have been developed that, with just four parameters, are able to predict the composition and dynamics of malignant brain tumor in agreement with experimental and clinical data [69, 70].

Piotrowska and Angus [101] developed a CA model that, as in Kansal et al. [69], uses the “many-to-one” assumption, where each lattice site has a volume that can contain N cells. In their work, Piotrowska and Angus [101] examined if the production of toxic waste (H^+ ions) by tumor cells would be enough to cause necrosis prior to the sub-viable nutrient-deficient stage of tumor development being reached. The model predictions suggest that the production of toxic waste is not sufficient to produce necrosis and the main cause of necrosis during the simulations is a drop of nutrient levels.

In [94], a tumor growth model was developed to study the effect of tumor shrinkage after the death of the cells. It is assumed that when tumor cells die due to necrosis, the volume of the necrotic cells occupy nearly one third

of volume of the proliferative cells. Better computational and experimental agreement is achieved when removing one third of the necrotic cells from the simulations. One question that may appear when defining the CA rules is how to treat the proliferation of a cell surrounded by other cells? In [94], two algorithms are explored. The first consists of a chain shifting along a straight line after cell division, and the second seeks a position for a newborn cell not near the mother cell, but on the surface of the tumor. Naumov et al. [94] conclude that both algorithms have agreement with experimental data and with each other, and that the second algorithm can be used as a substitute for the first due to its simplicity. In Naumov et al. [95] several mitosis rates are successfully studied and led to the validation of their model for simulating in vitro growth of the LoVo cells obtained by Demicheli et al. [45]. Experimental and computational results of tumor growth can also be reproduced by the Gompertz law, which suggest that at least 55% of inner proliferating tumor LoVo cells may divide in the proliferation process [95].

2.4 Agent Based Models

Another family of discrete models designed to capture events at the cell level is the so-called agent based models (ABM). They are designed to overcome the requirement that cells be constrained to a mesh by representing cells as agents that interact with each other. Each cell is modeled individually as a bounded domain, an agent, endowed with its own properties (e.g. position, volume, state, radius, time in that state). ABMs are supplied with rules that define the interactions between agents and their environment. Most of the tumor models that employ ABMs are hybrid models, in which changes in the microenvironment are modeled by systems of differential equations of the type occurring in various tissue models, described in the next section [42, 63, 84, 85, 97, 108].

Ramis-Conde et al. [108] studied the effects of the production of chemoattractant by tumor cells and degradation of the extracellular matrix (ECM) on cells motility. Tumor cells are modeled as discrete individual entities which interact with other agents. Cells secrete enzymes that degrade the extracellular matrix, facilitating cells migration. Tumor cells also release chemoattractant that drive other tumor cells forward the chemoattractant gradients. The behavior of the extracellular matrix, matrix degrading enzymes and degraded stroma are governed by partial differential equations [108]. The model is able to demonstrate the importance of chemoattractant gradients in the invasion process. In this model, invasion of surrounding tissue occurs after the tumor reaches a certain size and has the appearance of fingers which extend from the tumor's peripheral rim. In some computa-

tional results, it is possible to observe the formation of fingers in degraded areas of the ECM with high concentrations of chemoattractant.

In [97], ductal carcinoma *in situ* (DCIS) is modeled. DCIS is a non-invasive tumor and the most prevalent precursor to invasive ductal carcinoma (IDC) [84]. It is purely an ABM, i.e., a discrete model without partial differential equations is used for modeling the cell environment. In [97], cells are considered to be spheres, with a fixed size, and each is subject to a series of forces due to cell-cell interactions (e.g., repulsion and attraction). As the model in [97] does not take into account the nutrient concentration, necrosis is defined by the distance from the cell and the myoepithelial cell layer. Mechanical stress due to overcrowding in the apoptosis rate is also considered. It is worth mentioning that with all the simplifications in the model and the simple set of transitions rules, the model is able to reproduce the four morphological subtypes of DCIS found in the literature by balancing the apoptosis and mitosis rates. Numerical simulations indicate that the morphology observed at an instant in time can progress to others over time [97].

Macklin et al. [84] developed an hybrid ABM in order to model the DCIS. The ABM is used to model cell-cell and cell-basement membrane (BM) interactions. Contrary to the model proposed by Norton et al. [97], they model the nutrient concentration by a reaction-diffusion equation. The transitions between cell states are modeled as stochastic events governed by random variables that are related to the cell's state and the microenvironment [84]. The model is calibrated with patient-specific clinically-accessible histopathology data. In Hyun and Macklin [63], the calibration method is presented. The model is able to predict calcification and tumor sizes that quantitatively closely correlate clinical data. In [42], the ABM is extended by introducing a model of mechanical cell-BM-ECM interactions, where the basement membrane is subject to elasto-plastic forces. These deformations play an important role in the transition from DCIS to IDC. With these new assumptions, the membrane deformations and time-varying membrane properties can be depicted in numerical simulations.

2.4.1 An Agent Based Model for Ductal Carcinoma in Situ

To give more insights about the agent based approach, we described the model developed by Macklin et al. [84] with more details. In this model each agent is a cell that has the following properties: cell, nuclear and action radius, cell state (proliferative, apoptotic, necrotic, quiescent, hypoxic, calcified or motile), calcification degree, position and velocity. The forces considered in the model are shown in Figure 2.2. The repulsion and attraction occurs

between cell-cell and cell-basement membrane.

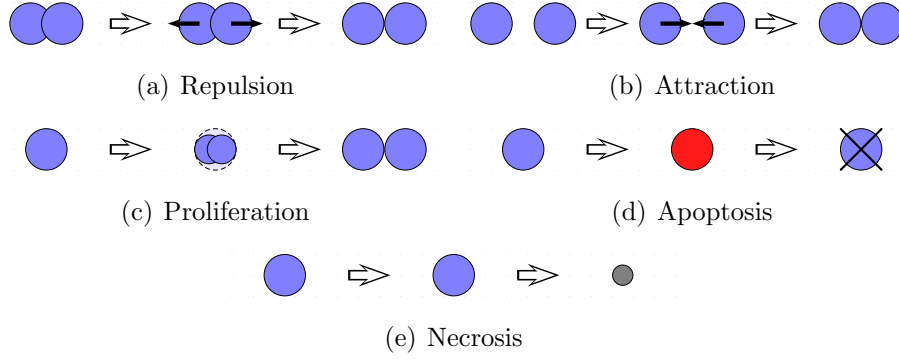


Figure 2.2: Representation of repulsion, attraction, proliferation, apoptosis and necrosis used in the model. Schematic description inspired in Norton et al. [97].

Cell-cell adhesion and repulsion are modeled through the potentials φ and ψ , respectively. Let R_A be the maximum adhesive interaction distance and $|\mathbf{r}|$ the distance between cell-cell or cell-membrane basement. For any $n \in \mathbb{N}$ define:

$$\nabla\varphi(\mathbf{r}; R_A, n) = \begin{cases} \left(1 - \frac{|\mathbf{r}|}{R_A}\right)^{n+1} \frac{\mathbf{r}}{|\mathbf{r}|}, & 0 \leq |\mathbf{r}| \leq R_A; \\ \mathbf{0} & \text{elsewhere.} \end{cases} \quad (2.1)$$

Similarly, if m is a fixed nonnegative integer, R_N is the nuclear radius, R is the cell's radius, and $M \geq 1$ is the cell's maximum repulsive force, define:

$$\nabla\psi(\mathbf{r}; R_N, R, M, m) = \begin{cases} -\left(M + c \frac{|\mathbf{r}|}{R_N}\right) \frac{\mathbf{r}}{|\mathbf{r}|}, & 0 \leq |\mathbf{r}| \leq R_N; \\ -\left(1 - \frac{|\mathbf{r}|}{R}\right)^{m+1} \frac{\mathbf{r}}{|\mathbf{r}|}, & R_N \leq |\mathbf{r}| \leq R; \\ \mathbf{0} & \text{elsewhere,} \end{cases} \quad (2.2)$$

where

$$c = \left(1 - \frac{R_N}{R}\right)^{m+1} - M. \quad (2.3)$$

The attraction and repulsion forces are given by equations 2.1 and 2.2, respectively, multiplied by constants depending on the interaction (i.e., cell-cell or cell-membrane basement). It is assumed that the forces equilibrate quickly (“inertialess” assumption) and, the forces are used to find the cell velocity.

The transitions between cell states are modeled as stochastic events governed by exponentially distributed random variables that are linked to the cell’s genetic and proteomic state, as well as the microenvironment (oxygen). It is a multiscale model where, at the macroscopic scale, oxygen transport is modeled by:

$$\frac{\partial \sigma}{\partial t} = \nabla \cdot (D \nabla \sigma) - \lambda(\mathbf{x}, t) \sigma, \quad (2.4)$$

where σ is oxygen, D is its diffusion constant, and λ is the uptake/decay rate. The couple between the discrete and continuous model is given by the variable λ . Tumor and host cells are assumed to uptake oxygen at rates λ_t and λ_h , respectively. Elsewhere, the oxygen “decays” at a low background rate λ_b . By considering that at each time t and space position \mathbf{x} , tumor cells, host cells, and stroma (non-cells), respectively, occupy fractions f_t , f_h , and f_b , such that $f_t + f_h + f_b = 1$, $\lambda(\mathbf{x}, t)$ is given by:

$$\lambda(\mathbf{x}, t) \approx f_t \lambda_t + f_h \lambda_h + f_b \lambda_b, \quad (2.5)$$

i.e., the uptake rates with weighting according to the tissue composition near \mathbf{x} .

In Figure 2.3 it is shown some results obtained by Rocha et al. [110] at different time steps. This experiment is capable of reproducing the effects of the repulsion, attraction and proliferation at cell scale.

2.5 Phase-Field and Mixture Theory Models

The tumor environment is composed of many constituents, among them we can cite proliferative, hypoxic and necrotic cells, nutrients, tumor angiogenesis factors, the extracellular matrix, and healthy cells. Continuum mixture theory is used to model such multiphase systems, in which multiple constituents can exist at each point of the medium and their presence is defined by different volume fractions of each constituent [17, 98]. For multiphase systems, the interface between constituents can be characterized by a gradient term in the energy of the system, in analogy with the Cahn-Hilliard (CH) equation [98].

The CH equation was originally developed to model processes of phase separation in binary alloys, which typically happen when an alloy is quenched to a critical temperature level at which the homogeneous mixture can no longer exist in equilibrium [51]. Roughly speaking, the CH equation defines a phase-field model, driven by a gradient system corresponding to an energy function that is always time-decreasing [76]. It has been recently used to

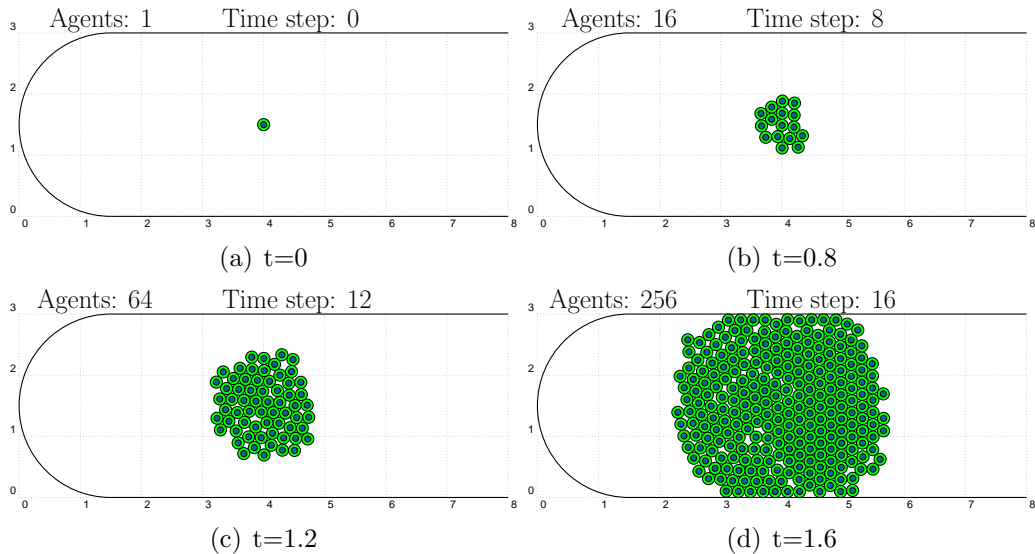


Figure 2.3: Growth of a tumor at different time steps considering just the repulsion, attraction and proliferation. Scale $1 = 0.1mm$.

model a variety of phenomena such as cancer growth [38, 59], among other applications involving moving interfaces. It is a nonlinear parabolic equation, fourth order in the spatial variables. The Cahn-Hilliard equation can be considered the prototype of a large class of nonlinear systems encountered in tumor growth models based on continuum mixture theory. Its primary feature of interest is that it depicts the complex interactions of two (or more) constituents without the need to track their interfaces, which are diffused over boundary layers developed automatically as a feature of the solution. Numerical solutions of the CH equation have been intensively studied and many finite difference, finite volume, finite element and spectral methods have been developed to obtain numerical solutions [47, 48, 49]. Many of the finite element methods are built based on a mixed variational formulation. A comparative study of different mixed finite element schemes for the 1D Cahn-Hilliard equation is found in Lima and Almeida [76], where it is shown that the computational cost can vary substantially depending on properties of the spatial approximations of the model and other parameters in the scheme.

Phase-field or diffuse-interface models provide a general framework for modeling multiphase materials in which the interface between phases is handled automatically as a feature of the solution [98]. A general derivation of continuum theory of mixtures with diffuse-interfaces is provided in Oden et al. [98], where general forms of constitutive equations are discussed as well as their roles on tumor growth models. Phase-field models have been applied

to several tumor growth works (see, e.g., Cristini et al. [38], Frieboes et al. [52], Hawkins-Daarud et al. [60], Lima et al. [77], Travasso et al. [139], Wise et al. [150] and references therein).

A two-species tumor growth model is developed in Cristini et al. [38]. In this model, the tumor growth is modeled by the Cahn-Hilliard equation for a binary system, composed by tumor and healthy cells. This equation is coupled to a transport equation for the nutrient concentration that is necessary for the growth of the tumor. This model describes the first stages of carcinogenesis, that is, the avascular stage. As the model does not consider the dead cells as a separate constituent, when the cells inside the tumor die because of the lack of oxygen, healthy cells assume their position, without representing the characteristic necrotic core.

The model developed by Wise et al. [150] also considers the evolution of the nutrient as a reaction-diffusion equation, but splits the tumor into viable and dead cells. With this modification, it is possible to reproduce the volume fraction of dead cells inside the tumor due to the lack of nutrients and oxygen. In the model developed by Hawkins-Daarud [59], the mixture is composed of four constituents, in which the tumor and healthy cells are considered as two constituents, and the extracellular water is divided into nutrient rich and nutrient poor extracellular water. Although the nutrient is incorporated as part of the mixture, the model does not reproduce the necrotic core inside the tumor.

Lima et al. [77] developed a hybrid ten-species phase-field model of tumor growth. In their model the tumor cells are divided into proliferative, hypoxic and necrotic cells and, as in [59], the nutrient is incorporated into the mixture. The avascular phase of tumor growth is coupled with an agent based model of angiogenesis, in which the tumor angiogenesis factor and the endothelial cells are treated in the phase-field formalism and the growth and branching of the blood vessels are discrete. The model is able to reproduce the growth and branching patterns of new blood vessels due to the lack of nutrients inside the tumor. These new sources of oxygen and nutrients increase the growth rate of the total tumor.

2.5.1 A Six-Species Phase-Field Model of Tumor Growth

The model developed in [77] is able to represent both the avascular and vascular stages of the tumor growth. The particular avascular model can be obtained by simplifying [77] as performed in [78]. In the latter work a material body composed of $N = 6$ constituents such that a proportion of each constituent exists at a given point in the body at the same time [59, 61, 98]. For a differential volume dv containing a point (\mathbf{x}, t) , let dv_i

be the proportion occupied by the constituent i determined by the volume fraction of each constituent so that $\phi_i(\mathbf{x}, t) = \frac{dv_i}{dv}$ is the volume fraction of the i th constituent [59]. For a closed system, the sum of all volume fractions from all the constituents of the mixture at a point must be equal to one, i.e.,

$$\sum_{i=1}^N \phi_i = 1. \quad (2.6)$$

The mixture is composed of the following ten species volume fractions:

- ϕ_P - proliferative tumor cell;
- ϕ_H - hypoxic tumor cell;
- ϕ_N - necrotic core;
- ϕ_σ - nutrient-rich extracellular water;
- ϕ_{σ_o} - nutrient-poor extracellular water;
- ϕ_C - healthy cell.

The mass balance for the volume fractions for all constituent i , $1 \leq i \leq N$, for all (\mathbf{x}, t) , $\mathbf{x} \in \Omega \subset \mathbb{R}^d$ ($d = 1, 2, 3$), assumes the form

$$\frac{\partial \rho_i \phi_i}{\partial t} + \nabla \cdot (\rho_i \phi_i \mathbf{v}_i) = S_i - \nabla \cdot \mathbf{J}_i, \quad (2.7)$$

where ρ_i is the mass density per unit volume (we assume $\rho_i = \rho = \text{constant}$), \mathbf{v}_i is the velocity, S_i is the mass supplied to constituent i by other constituents and \mathbf{J}_i is the mass flux. The species mass flux accounts for the mechanical interactions among constituents and is assumed to be of the form

$$\mathbf{J}_i = - \sum_{j=1}^N M_{ij} \nabla (D_{\phi_i} E_j), \quad (2.8)$$

where M_{ij} is the mobility of constituent j in phase i , the functional derivative with respect to ϕ_i is denoted by $D_{\phi_i}(\cdot)$, and E_j is the energy of species j given by the Ginzburg-Landau energy associated with the interactions among mixture constituents defined on a domain $\Omega \subset \mathbb{R}^3$,

$$E_i = \int_{\Omega} \left[\Psi_i(\phi_1, \dots, \phi_N) + \phi_i \sum_{j=1}^N \chi_{ij} m_j + \sum_{j=1}^N \frac{\epsilon_{ij}^2}{2} |\nabla \phi_j|^2 \right] d\mathbf{x}, \quad (2.9)$$

where m_j denotes the concentration of chemical factors that interact with ϕ_i , χ_{ij} are the corresponding chemotactic coefficients and ϵ_{ij}^2 measures the interfacial strength among constituents interactions. The bulk energy of the constituents due to local interactions is modeled by the potential Ψ_i [150]. Finally, the chemical potential μ_{ij} is given as a function of the free energy E_i according to

$$\mu_{ij} = \frac{\partial E_j}{\partial \phi_i} - \nabla \cdot \frac{\partial E_j}{\partial \nabla \phi_k}. \quad (2.10)$$

The local dynamics of the tumor growth depends on the nutrient availability. We define σ_{PH} , σ_{HP} and σ_{HN} as the nutrient thresholds involved in the transfer from proliferative to hypoxic cell states, from hypoxic to proliferative cell states and from hypoxic to necrotic cell states, respectively. The associated transition rate from this stages are given by λ_{PH} , λ_{HP} and λ_{HN} . The proliferating tumor cells can grow when consuming nutrient with a constant rate of cellular mitosis λ_P and also when the nutrient level increases, which allows the hypoxic cells to return as proliferating cells. They also decay owing to natural death of cells at the apoptosis rate λ_A . Moreover, when the level of nutrient drops below the hypoxic threshold σ_{PH} , the proliferating cells enter the hypoxic class. The hypoxic cells are in a resting (quiescent) state in which they do not proliferate. The volume fraction of hypoxic cells decays due to apoptosis or by the return of hypoxic cells to the proliferative state as the nutrient level increases to values higher than σ_{HP} . They also can irreversibly become part of the necrotic core as the nutrient level drops below the necrotic threshold. The necrotic core of the tumor can never decrease as we consider the calcification process. Cells that die by apoptosis increase the nutrient-rich extracellular water volume fraction. Figure 2.4 depicts the main hypothesis forming the basis of the model. With these assumptions, the source terms proposed in Lima et al. [78] are given by

$$\left. \begin{aligned} S_P &= \lambda_P \phi_\sigma \phi_P - \lambda_A \phi_P - \lambda_{PH} \mathcal{H}(\sigma_{PH} - \phi_\sigma) \phi_P \\ &\quad + \lambda_{HP} \mathcal{H}(\phi_\sigma - \sigma_{HP}) \phi_H, \\ S_H &= -\lambda_A \phi_H + \lambda_{PH} \mathcal{H}(\sigma_{PH} - \phi_\sigma) \phi_P - \lambda_{HP} \mathcal{H}(\phi_\sigma - \sigma_{HP}) \phi_H \\ &\quad - \lambda_{HN} \mathcal{H}(\sigma_{HN} - \phi_\sigma) \phi_H, \\ S_N &= \lambda_{HN} \mathcal{H}(\sigma_{HN} - \phi_\sigma) \phi_H, \\ S_\sigma &= -\lambda_P \phi_\sigma \phi_P - \lambda_{P_h} \phi_\sigma \phi_H + \lambda_A (\phi_P + \phi_H). \end{aligned} \right\} (2.11)$$

Assuming that the tumor volume fraction is given by $\phi_T = \phi_P + \phi_H + \phi_N$, the system can be written as

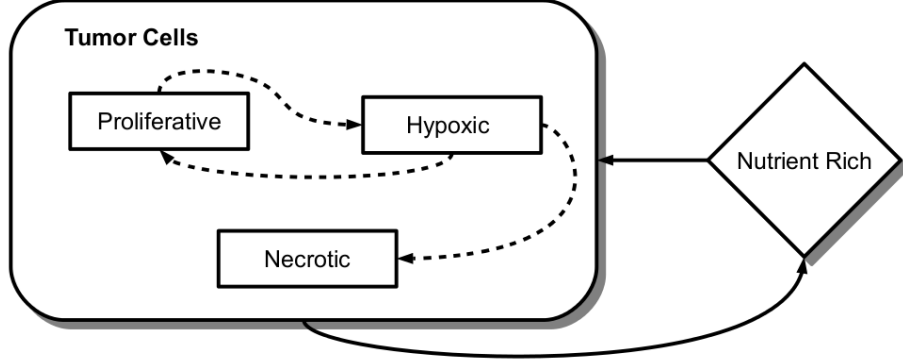


Figure 2.4: Conceptual scheme of the tumor growth model. The dynamics of tumor cells depends on the nutrient availability (after [77]).

$$\left. \begin{aligned}
 \frac{\partial \phi_\sigma}{\partial t} &= \nabla \cdot M_\sigma \delta_\sigma^{-1} \nabla \phi_\sigma - \nabla \cdot M_\sigma \chi_0 \nabla \phi_T + S_\sigma, \\
 \frac{\partial \phi_T}{\partial t} &= \nabla \cdot \mathcal{M}(\phi_T, \phi_H, \phi_N) \nabla \mu + S_T, \\
 \mu &= \Psi'(\phi_T) - \epsilon_T^2 \Delta \phi_T - \chi_0 \phi_\sigma, \\
 \frac{\partial \phi_H}{\partial t} &= \nabla \cdot \bar{M}_H \phi_H^2 \nabla \mu + S_H, \\
 \frac{\partial \phi_N}{\partial t} &= \nabla \cdot \bar{M}_N \phi_N^2 \nabla \mu + S_N,
 \end{aligned} \right\} \text{in } \Omega \times (0, T), \quad (2.12)$$

where $S_T = \lambda_P \phi_\sigma (\phi_T - \phi_H - \phi_N) - \lambda_A (\phi_T - \phi_N)$. Concentration dependent mobilities are assumed for tumor cells [77] so that $\mathcal{M}(\phi_T, \phi_H, \phi_N) = \bar{M}_P (\phi_T - \phi_H - \phi_N)^2 + \bar{M}_H \phi_H^2 + \bar{M}_N \phi_N^2$, $M_H = \bar{M}_H \phi_H^2$ and $M_N = \bar{M}_N \phi_N^2$, where \bar{M}_P , \bar{M}_H and \bar{M}_N are positive constants. Moreover, the first equation in (2.12) is obtained by substituting $D_{\phi_\sigma} E$ into the flux $\mathbf{J}_\sigma = -M_\sigma \nabla D_{\phi_\sigma} E$. By setting the mobility for the nutrient-rich constituent $M_\sigma = \delta_\sigma D$, $D > 0$, we notice that the dynamics of the nutrient constituent is simply governed by diffusion, disregarding other interactions. Finally, typical boundary conditions are listed as follows:

$$\left. \begin{aligned}
 \nabla \phi_T \cdot \mathbf{n} = \nabla \mu \cdot \mathbf{n} = \nabla \phi_H \cdot \mathbf{n} = \nabla \phi_N \cdot \mathbf{n} = 0, \\
 \phi_\sigma = 1,
 \end{aligned} \right\} \text{on } \Gamma \times (0, T). \quad (2.13)$$

Figure 2.5 shows the volume fraction for the tumor, hypoxic and necrotic cells and nutrient-rich extracellular water. The characteristic lack of nutrient inside the tumor is reproduced using the hypoxic threshold $\sigma_{PH} = 0.4$ and necrotic threshold $\sigma_{HN} = 0.2$ at $t = 13$. The initial condition represents a cluster of three small tumor masses.

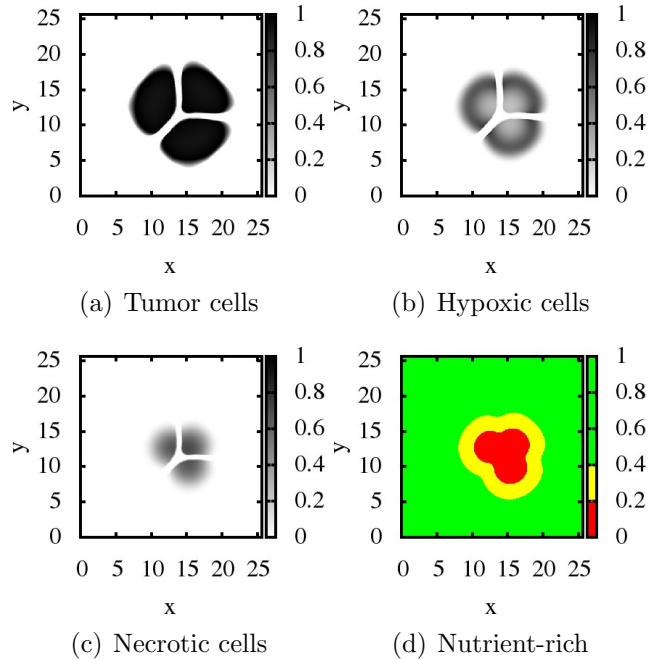


Figure 2.5: Volume fraction for tumor, hypoxic and necrotic cells and nutrient-rich at $t = 13$ (after [78]).

2.6 Models of Mechanical Stress and Deformation of Anisotropic Vascular Tumor

There have also been some recent studies accounting for heterogeneity and anisotropy in tumor growth. A finite differences based framework for the anisotropic, heterogeneous and 3D diffusive tumor growth model has been developed [111]. A recently developed heterogeneous 3D avascular tumor model have used lattice gas cellular automata employing a particle lattice structure where the movement and transition of cells are determined by a set of local rules [121].

Moreover, the growth process of the tumor can induce morphological instabilities and surface wrinkling behavior [27]. To be more specific, the mobility of tumor cells at nutrient gradients may drive fingering instabilities

[38]. The transport limitations of cell nutrients along with the growth factors may lead to morphological instability, fingering and fragmentation of tumor [83].

Some of the recent findings indicate the importance of the mechanical force and stress exerted by the solid tumor along with the interstitial fluid pressure in the evolution of tumor [10, 24, 30, 106, 125, 126, 130, 142, 149, 152]. By a quantitative analysis of both a biophysical agent-based and a continuum mechanical model, Byrne and Drasdo (2009) have shown that the cell proliferation is controlled by mechanical stress [24]. Experimental evidence shown that the shape of tumor is dictated by the surrounding solid stress field [30]. Both experimental and theoretical studies have identified the interstitial fluid pressure as a critical elements in solid tumor growth [152]. Abundance of leaky blood vessels (that causes excessive fluid loss) and lack of functional lymphatic vessels (which could have absorbed the excess fluid) lead to abnormally high interstitial pressure in tumor [130]. Voutouri *et. al.* (2014) found that the evolution of stress and the growth rate of the tumor are independent from the selection of the constitutive equation, but depend strongly on the mechanical interactions with the surrounding host tissue [142]. The generated compressive mechanical stress plays an important role in the growth and spread of tumor [142]. On one side, it can limit the size of tumor, thus adversely affecting the tumor growth process [30, 142]. On the other hand, it also causes a net outward flow of plasma-like fluid through the interface between the tumor and healthy tissue and thus impedes the delivery of drug [106]. The resulting mechanical force is capable of compressing blood and lymphatic vessels can cause hypoperfusion and hypoxia promoting immune evasion.[65, 125]. Moreover, the high permeability and tortuousness of the blood vessels also contribute to the metastasis process [65, 142]. Experimental results also suggests that the lack of nutrient can enhance the invasive behavior of a tumor [38]. In a comprehensive review on metastasis, Wirtz *et. al.* (2011) explained the key role played by mechanical forces and physical interaction on cell motility and cancer spread [149]. Some pharmacologic and biologic agents, and physical manipulation methods are known to reduce tumor pressure that contribute to the treatment of cancer [10]. Stylianopoulos *et. al.* (2012) presented a method to measure the solid stress accumulated during the tumor growth process generalized for human and animals [125]. Although the compressive radial and circumferential stress is present at the center of the tumor, there is tensile circumferential stress at the interface between solid and healthy tissue [112, 126].

Returning to the mixture models of Section 2.5, we focus on the simplified case of a three-constituent mixture comprised of tumor, healthy, and water

constituents (i.e. $\alpha = T, H, W$),

$$d_a \frac{\partial c_N}{\partial t} + \underbrace{\nabla \cdot (-c \nabla c_N)}_{\text{diffusion}} + \underbrace{\mathbf{v}_W \cdot \nabla c_N}_{\text{convection}} = \underbrace{S_N}_{\text{nutrient consumption}}, \quad (2.14)$$

where c_N is the concentration of nutrient, c is the diffusion coefficient, \mathbf{v}_W is the velocity of the water constituent, $S_N = -c_c \hat{\rho}_T$ is representing the consumption of nutrient by the tumor tissue, and d_a is the damping or mass coefficient. The balance of momentum equation can be written as

$$\nabla \cdot \mathbf{T}_\alpha + \rho_\alpha \mathbf{b} + \hat{\mathbf{p}}_\alpha = \hat{\rho}_\alpha \mathbf{v}_\alpha. \quad (2.15)$$

where \mathbf{T}_α is the partial Cauchy stress tensor, and the term $\rho_\alpha \mathbf{b}$ is the volumetric body force. The expression $\hat{\rho}_\alpha \mathbf{v}_\alpha$ represents the exchange of linear momentum through the density supply $\hat{\rho}_\alpha$, and $\hat{\mathbf{p}}_\alpha$ describes the interaction force from other constituents, which is an internal force within the mixture.

One example of a model in this class of deformable-solid models is that of a transversely isotropic biological tissue featuring a preferred direction, where the material symmetry imposes conditions on any tensor that describes properties in the domain. The preferred direction can be either fixed or a time dependent based on the availability of nutrients. In three dimensions, this direction can be described by a unit vector, $\mathbf{A} = (A_x; A_y; A_z)^T$, and introducing the structural tensor $\mathbf{M} = \mathbf{A} \otimes \mathbf{A}$. The entropy inequality for the mixture yields the following constitutive relations for the partial Cauchy stress tensors of the combined (healthy and water) and tumor constituents

$$\left. \begin{aligned} \mathbf{T}_S &= -n_S \lambda \mathbf{I} + \mathbf{T}_S^E, & n_S &= n_T + n_H, \\ \mathbf{T}_W &= -n_W \lambda \mathbf{I}, \end{aligned} \right\} \quad (2.16)$$

where, the subscript s denotes the solid constituents (i.e., the tumor and healthy constituents), λ is the fluid pressure, \mathbf{I} is the identity tensor, \mathbf{F}_S is the deformation gradient of s , $\mathbf{T}_S^E = 2\rho_S \mathbf{F}_S \frac{\partial \phi_S}{\partial \mathbf{C}_S} \mathbf{F}_S^T$ is the effective stress of the solid constituents s . where, $\mathbf{C}_S = \mathbf{F}_S^T \mathbf{F}_S$ is the right Cauchy-Green tensor of s and ϕ_S is the Helmholtz free energy of the solid skeleton that can be divided into isotropic and transversely isotropic parts as following [109],

$$\phi_S = \left(\frac{n_S}{n_S^0} \right)^n \phi_{S,iso}(I_1, I_2, I_3) + \phi_{S,ti}(J_4, J_5), \quad (2.17)$$

where, $I_{1,2,3}$ are the principal invariants of \mathbf{C}_S , $J_{4,5}$ are the basic invariants of the argument tensors \mathbf{C}_S and \mathbf{M} , $\mathbf{M} = \mathbf{A} \otimes \mathbf{A}$ is the Structural tensor,

$\mathbf{A} = [A_x \ A_y \ A_z]^T$ is a unit vector in the preferred direction of the transversely isotropic solid tumor tissue.

After some lengthy calculations, stress in the solid constituent is derived as,

$$\mathbf{T}_S^E = 2\rho_S \mathbf{F}_S \frac{\partial \phi_S}{\partial \mathbf{C}_S} \mathbf{F}_S^T = J_S \frac{n_S}{n_S^0} \left[\left(\frac{n_S}{n_S^0} \right)^3 \mathbf{T}_{S,iso}^E + \mathbf{T}_{S,ti}^E \right], \quad (2.18)$$

where,

$$\begin{aligned} \mathbf{T}_{S,iso}^E &= \frac{1}{J_S} [2\mu_S \mathbf{K}_S + \lambda_S (\log J_S) \mathbf{I}], \\ \mathbf{T}_{S,ti}^E &= \frac{1}{J_S} \alpha_1 \alpha_2 [\text{tr}(\mathbf{C}_S \mathbf{M}) - 1]^{\alpha_2 - 1} \mathbf{F}_S \mathbf{M} \mathbf{F}_S^T. \end{aligned} \quad (2.19)$$

Herein, $\mathbf{K}_S = \frac{1}{2}(\mathbf{F}_S \mathbf{F}_S^T - \mathbf{I})$ is the Karni-Reiner strain tensor, and $\alpha_1 \geq 1$ and $\alpha_2 > 1$ are parameter due to the stiffness of the preferred direction \mathbf{A} . The interaction force $\hat{\mathbf{p}}_W$, i.e. the force applied by the combined solid (tumor and healthy) constituents on the water constituent, is obtained from the entropy inequality

$$\begin{aligned} \hat{\mathbf{p}}_W &= \lambda \nabla n_W - \mathbf{S}_W \mathbf{w}_{WS}, \\ \mathbf{S}_W &= \frac{\mu_{WR}}{k_S^0} \left(\frac{n_W}{n_W^0} \right)^m (\beta_1 \mathbf{I} + \beta_2 \mathbf{M})^{-1}, \end{aligned} \quad (2.20)$$

where, $\mathbf{w}_{WS} := \mathbf{v}_W - \mathbf{v}_S$ is the seepage velocity, \mathbf{S}_W describes the permeability tensor of water constituent in connection to the relative velocity, m denoting a dimensionless material parameter, μ_{WR} the shear viscosity of the fluid, $k_S^0 = k_S^0(n_H)$ the intrinsic permeability, β is the parameter to quantify the relative importance of transversely isotropic symmetry compared to isotropy. Based on the entropy inequality, mass exchange is proportional to the difference between the chemical potentials of tumor and healthy constituents.

Results of calculations performed in a model problem consisting of a finite element model with 75000 degrees of freedom depicting a growth of an anisotropic tumor mass, initially spherical, over a period of 28 days are given in this section. The computational domain is represented by a 10 cm \times 10 cm \times 10 cm cubic shaped control volume (as shown in Figure 2.6). There is a sphere with a radius 0.6179 cm located at the center of this geometry that represents the tumor domain Ω_T while the region outside the spherical tumor domain represents the healthy tissue domain Ω_H . The magnitude of the tumor radius is calculated from the experimental volume of the tumor in [14] after 7 days of a human head and neck squamous cell carcinoma (HNSCC) xenograft inoculation is performed in nude rats. The parameters are

obtained from the literature and experimental calibrations. The volumetric growth of tumor at various time is compared (shown in Figure 2.7) with the literature and used it to calibrate model parameters. Temporal evolution of the tumor morphology is also shown in Figure 2.7 using 3D contour plots of tumor volume fraction n_T . The interface between tumor and healthy tissue is observed to become irregular in Figure 2.7 because of the tissue anisotropy (transverse isotropy) and neo-Hookean tissue behavior although it started as a smooth sphere at $t = 7$ day. The volume of the tumor domain is seen to be increasing over time. In Figure 2.7 the simulation and experimental results show similar trend. Both of them are showing exponential increase in the tumor volume. Moreover, the 3D contour plots of tumor volume fraction n_T at different time points serve as a visual representation of the tumor volume which is increasing over time. The interface between tumor and healthy tissue is seen to gradually become irregular because of the gradient of the nutrient concentration c_N , tissue anisotropy (transverse isotropy) and neo-Hookean tissue behavior although it started as a smooth sphere at $t = 7$ day.

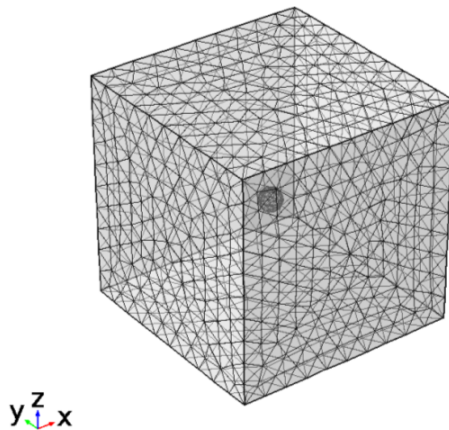


Figure 2.6: Finite element mesh of the 3D computational domain.

A 3D contour plot of tumor volume fraction n_T at the final ($t = 24$) day is shown in Figure 2.8. To better understand the morphological instability, fingering and fragmentation - a 2D cross sectional view of the volume fraction n_T is shown in Figure 2.9(a). While growing, the tumor tissue consumes nutrient. The 2D cross sectional view of nutrient concentration c_N in Figure 2.9(b) clearly showed depletion near the tumor core. This result gives an indication about the necrotic core although the dead tumor cells are not modeled explicitly. As mentioned, the concentration gradient of nutrient (shown in Figure 2.9(c)) is an important contributor to the amorphous shape of the

tumor along with the tissue anisotropy and neo-Hookean behavior. Because of the concentration gradient of nutrient, different portions of the proliferative tumor constituents consume different amount of nutrient, leading to the fingering instabilities. As a result, in Figure 2.9(d)), spatially variable mass exchange rate between tumor and healthy constituents is observed.

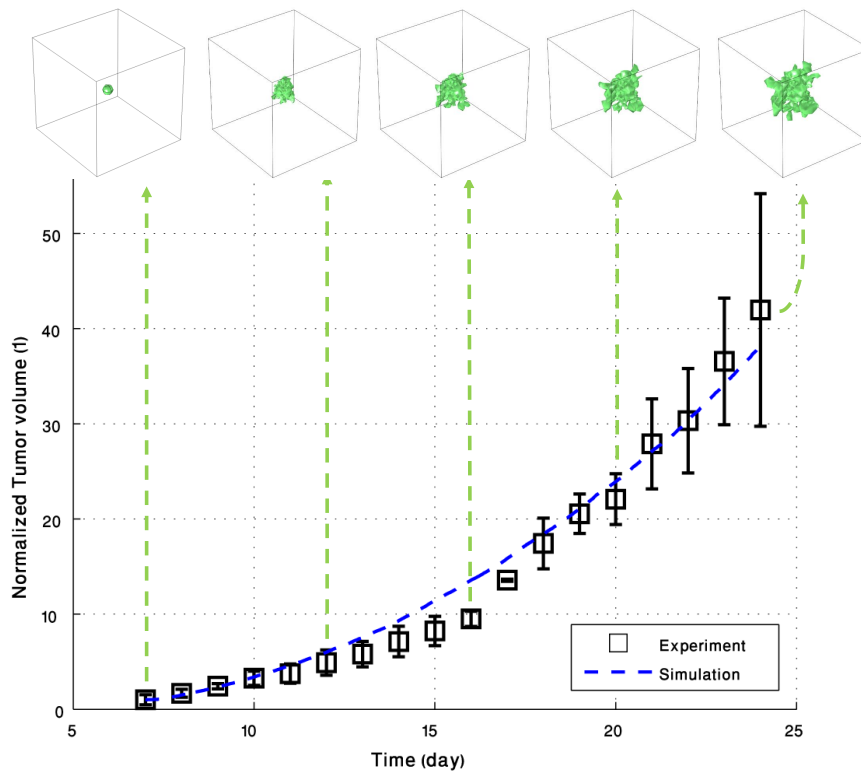


Figure 2.7: Comparison with the experimental data from [14] and the temporal evolution of the tumor morphology

2.7 Signaling Models

Multicellular organisms rely on complex biochemical communication signaling systems for their organization and functioning and each individual cell plays a specific role in the system. All cell processes are mediated by intercellular and intracellular communication, which is carried out through a highly integrated network of finely tuned pathways, that ultimately elicit a target response. Those signaling networks consist, in general, of a large

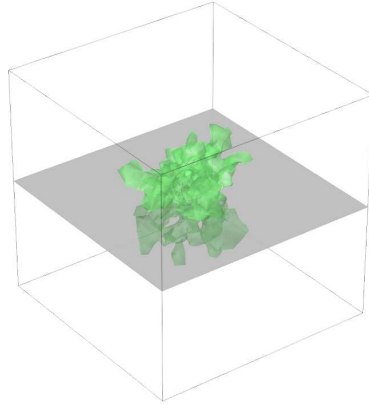


Figure 2.8: On the final ($t = 24$) day the 3D view of the tumor and the location of the cross-sectional plane.

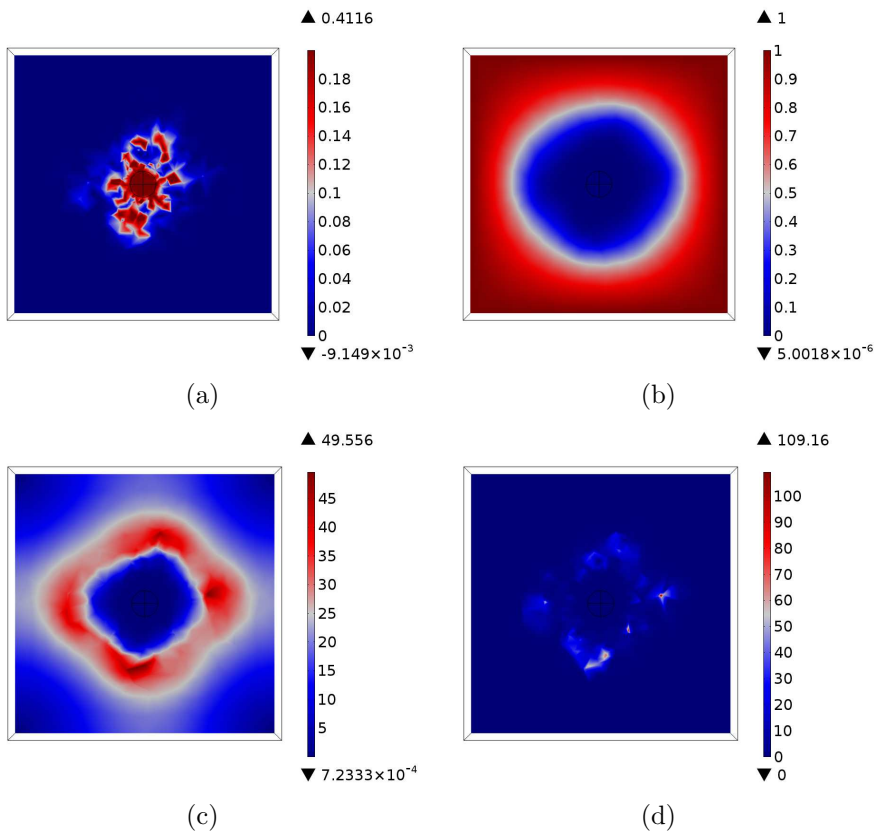


Figure 2.9: On the final ($t = 24$) day the cross-sectional plane for the (a) volume fraction of tumor constituent n_T , (b) concentration of nutrient c_N , (c) gradient of the concentration of nutrient c_N , and (d) rate of mass exchange between tumor and healthy constituents $\hat{\rho}_T$.

number of different proteins and molecules that biochemically interact in a strongly nonlinear way to produce appropriate response to environmental and physiological conditions. The network processes are very complex, interconnected through crosstalk mechanisms, in which the extracellular information is received, amplified, spread, and ultimately alters gene expression, cell proliferation, differentiation and apoptosis, and metabolism [56]. The type of flow of chemicals towards a target characterizes the type of signaling, as schematically depicted in Figure 2.10. Direct signaling occurs through gap junctions that connect neighboring cells, allowing the transfer of signaling molecules by a cell-to-cell contact. In autocrine signaling, the cell targets itself or a similar cell. Local and fast extracellular communication, over short distances, characterizes paracrine signaling, while endocrine signaling is longer extracellular communication over large distances. The type of the final response as well as the presence of some specific mechanisms define the type of signaling network.

The control of gene expression that keeps appropriate expression levels at specific times in certain types of cells to assure their functioning are performed by gene regulatory networks. A generic schematic description of a gene regulatory network is shown in Figure 2.11. Generally, the term signaling pathway is usually used to refer only to a part of intracellular reactions network that is responsible for processing the signal of interest. It starts with a cell receiving an extracellular stimulus/information/signaling through an adequate surface receptor. This receptor triggers a biochemical process in which the information is converted into a chain of other chemical forms that ends up creating a response to information from the environment. According to [74], once activated, these receptors start signaling pathways (or signal-transduction cascades), which ultimately determine the response of the cells. Moreover, this flow of information is not linear and one or more components of one pathway may affect or be affected by another pathway. Also, one receptor can activate several different pathways as in the metabolic networks, where there is not only signal flow but the production and consumption of mass flow.

The signaling pathways can be viewed as molecular circuits that detect, amplify, and integrate a variety of external signals to generate responses. The response may be in the form of either rapid non-genomic effects, such as changes in enzyme activity, or slower genomic responses such as changes in gene expression. Once a cell has completed its response to a signal, the signaling process must be terminated or the cell loses its responsiveness to new signals [18]. Many pathological states may appear due to disruption of signaling pathways. Also, it is well recognized that many cancers are linked to signaling processes that are not properly terminated [18]. In particular,

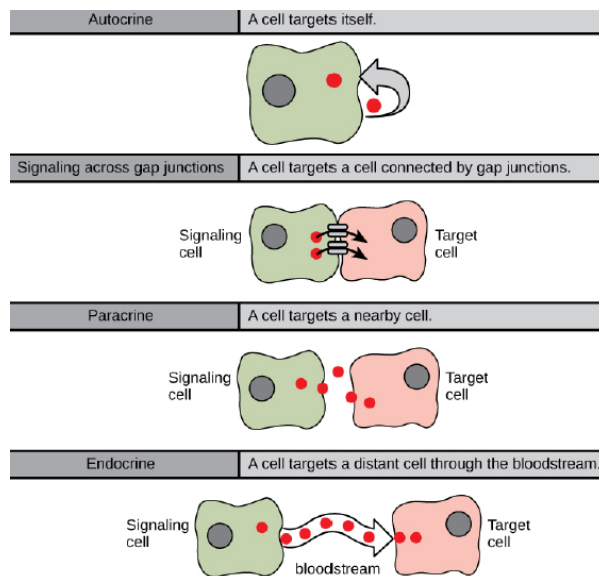


Figure 2.10: Generic schemes of different types of signaling (extracted from <https://www.boundless.com/biology/textbooks/boundless-biology-textbook/>).

the tumor glycolysis involved in the altered metabolism of cancer cells, one of the hallmarks of cancer, is now considered a target for cancer therapies [54, 58, 117, 143].

An attempt to understand the connection between the signaling networks in a cell and the hallmarks of cancer is described in [57] in a form of an integrated circuit. This description is segmented into distinct subcircuits later in [58], in which it proposed that each subcircuit be related to a specific hallmark characteristic of cancer cells. Only a few capabilities of modern signal models are described in [58] since many remain poorly understood, as pointed out by the authors. The model is considered to be still a somewhat simplistic model by the authors since it disregards many crosstalk and extracellular signal from a variety of different stimuli within the tumor microenvironment.

Thus, an integrated understanding of these mechanisms and their dynamic interplay is now recognized to play an important role in cancer development as well as significantly impact the design and improvement of therapeutic strategies to control cancer progression. However, many mechanisms remain unknown. Mathematical modeling can help to elucidate the dynamics of signaling pathways, its key components and the cross-talk among different pathways at different scales. Moreover, can give insight on how to intervene

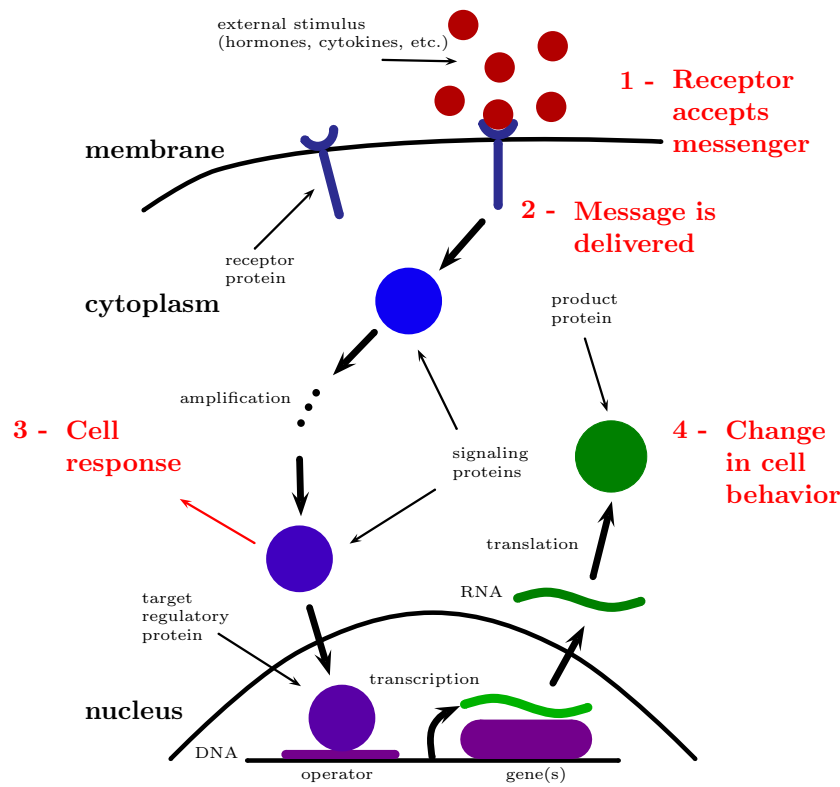


Figure 2.11: Generic scheme of a cellular signaling pathway. Inspired by Rybinski [114].

and promote new strategies to treat the disease. Under this perspective, experimental approaches are combined with mathematical modeling to understand complex behavior of signaling pathways. The level of detail of the mathematical model is driven by the main focus of the investigation and by the type of available data to calibrate and validate the model.

The modeling studies of signaling pathways can broadly be classified as continuum and discrete studies. A typical discrete dynamic model is based on Boolean networks, which were initially proposed for modeling gene regulatory networks [138, 144]. In this approach, the protein-protein interactions are described qualitatively so that the kinetics of individual protein interactions are not taken into account. The signaling network is represented as a graph in which the nodes represent the signaling molecules and the edges represent their interactions. They are described through Boolean functions, one assigned to each node, and ultimately define the binary state of the node. As this approach is parameter-free and qualitative, it is suitable for qualita-

tively analyzing complex large-scale systems, to infer regulatory interactions and activity changes of components following a perturbation [144].

The more conventional mathematical approach to model signaling pathways is through a continuum perspective that considers ordinary differential equations (ODEs). The ODE network is a set of coupled ODEs built assuming that the signaling molecules are highly abundant in the cell under well-mixed conditions, at concentrations high enough to disregard individual stochastic behaviors. The main rationale is posed by the law of mass action that states that the rate of a reaction is proportional to the product of the concentration of the reactants. Each ODE in the network expresses such mass balance, that depends on the mentioned rates of reactions, which are model parameters that have to be estimated on the lights of available data. One of the main challenges of this approach is to select the model granularity to represent the desired pathway, which ultimately defines the number of parameters to be calibrated. Direct measure of parameters is very limited and usually the parameters are estimated mainly through regression procedures so as to achieve the design goals. However, the experimental acquisition of enough high quality data to effectively constrain parameter values is challenging. This is the main reason why most biological pathway models remain poorly calibrated [5].

Spatially distributed signaling networks are used to describe the biochemical interplay among molecules that diffuse in the environment. In those cases, biochemical reactions can disrupt homogeneity and partial differential equations (PDEs) are the usual way to model the processes. A few examples of spatially distributed signaling is presented in [71], in which is highlighted how a flow quantity (concentration or activity) changes continuously in time and space and the relevance of the spatial organization on the network function. Stochastic models are also used if molecular fluctuations are relevant, what happens when the number of molecules is small enough and the likelihood of interaction between two molecules has to be taken into account. In [67] one may find an overview of typical methods used in systems biology today to take account of stochasticity. See also [31] for a new efficient way to deal with stochastic biochemical systems. Finally, discrete approaches, mainly agent (or multi agent) based methods, are rules-based modeling approaches that provide easier ways of representing the interactions between entities [92, 120]. Agent based modeling approaches have been used to study *in silico* how signaling molecules influence carcinogenesis. As an example, Wang et al. [145, 146, 147] investigated the role of signaling molecules and their cross-talk in two different pathways in the growth of a lung cancer. They showed how different external microenvironments stimuli influence the dynamics by triggering competing multicellular phenotypes. In

addition to enabling tracking of the tumor growth dynamics across different scales, this approach provided important insights on the therapeutic management by showing that the chemotherapeutic intervention against on one signaling pathway may be insufficient.

To convey the basic ideas of the ODE/PDE approach, consider a typical scenario of a cancer progression and invasion. It is a complex process involving an intricate interplay of a numerous signaling pathways, cell-cell and cell-microenvironment mechanical/chemical interactions. In order to grow, the tumor cells need to remodel their environment by inducing the growth of new blood vessels as a source of nutrients and interacting with the ECM. The interactions in the ECM include the degradation in order to facilitate the mobility and the regeneration in order to serve as a support to fix the cells. It is known that the degradation and regeneration of extracellular matrix (ECM) are regulated by paracrine signals, many of them due to proteolytic enzymes called metalloproteinases (MMPs), whose members express characteristics to either promote or suppress carcinogenesis. MMPs are secreted in their inactive forms by both tumor and normal cells. They interact to promote mutual activation and are balanced by endogenous tissue inhibitors of metalloproteinases (TIMPs). They can exhibit both pro- and anti-invasive characteristics and some are soluble (diffusible) and some are insoluble (membrane bound) [11]. Matrix destruction and regeneration is mediated by the paracrine signals between TIMPs and MMPs, and a protease-dependent model of cancer invasion was developed in [43] by considering this paracrine signaling pathway in a simple cancer cells - extracellular matrix interaction model. This model considers the role of two representative metalloproteinases, the collagenolytic membrane-bound MT1-MMP and the gelatinolytic soluble MMP2, and one endogenous tissue inhibitors of metalloproteinases, TIMP2. In the model, the paracrine signaling is further simplified by assuming that MT1-MMP is expressed in its active state, it is inhibited by the freely diffusive TIMP2 through the formation of a membrane bound complex which in turn is able to activate MMP2. The proteolytic activity of MT1-MMP is localized due to the cell bound and the more extensive tissue degradation is provided by the diffusible active MMP-2. The general scheme of the signaling interactions is depicted in Figure 2.12.

The stages 2,3 and 4 are simplified by considering the complex $f(x, t)$ that ultimately activates MMP2, yielding the following nondimensional system of

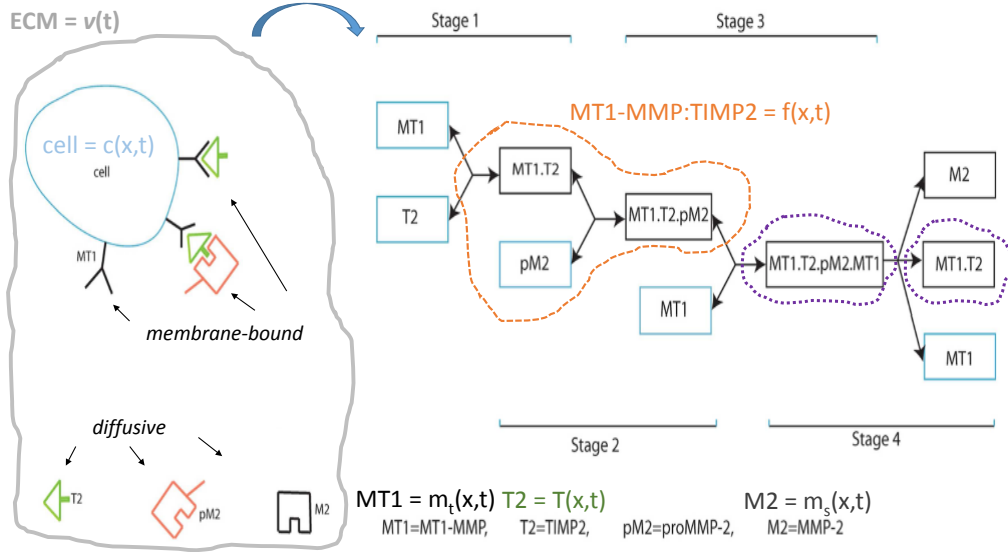


Figure 2.12: Schematic diagram of the paracrine pathway that regulates ECM (modified from [43]).

equations:

$$\begin{aligned}
 \frac{\partial c}{\partial t} &= \nabla \cdot (D_c \nabla c - \chi c (s - 1 + v) (1 - c - v) \nabla v) \\
 &\quad + \mu_c c (1 - c - v) \\
 \frac{\partial v}{\partial t} &= -\delta (s - 1 + v) (m_s + m_t) + \mu_v (1 - c - v) \\
 \frac{\partial m_s}{\partial t} &= \nabla \cdot (D_{m_s} \nabla m_s) - \phi_{31} T m_s + \phi_{32} m_t f - \beta_{m_s} m_s \\
 \frac{\partial m_t}{\partial t} &= m_t \nabla \cdot (D_c \nabla c - \chi c (s - 1 + v) (1 - c - v) \nabla v) \\
 &\quad - \phi_{41} T m_t + \phi_{42} - \beta_{m_s} m_t + \alpha_{m_t} c (1 + v) \\
 \frac{\partial T}{\partial t} &= \nabla \cdot (D_T \nabla T) - \phi_{51} T m_s + \phi_{52} T m_t + \phi_{53} f - \alpha_{Tc} c \\
 \frac{\partial f}{\partial t} &= f \nabla \cdot (D_c \nabla c - \chi c (s - 1 + v) (1 - c - v) \nabla v) \\
 &\quad + \phi_{61} T m_t - \phi_{62} f m_t - \phi_{63} f \\
 \frac{\partial s}{\partial t} &= -\delta_s (1 - s) m_t
 \end{aligned} \tag{2.21}$$

This model includes the matrix suitability modifier $s(x, t)$ that takes into account the volume fraction of the substrate that is available to be degraded.

The cancer cells can diffuse randomly in the medium and have the haptotactic movement up a gradient of extracellular matrix. They also proliferate according with competition for space with the ECM. This competition also drives the ECM remodeling, which is degraded by both MT1 and MMP2. MT1 is produced by cancer cells while MMP2 is activated by the complex f (MT1-MMP:TIMP2:proMMP2), they both are inhibit by TIMP2 and there is a natural decay of the enzymes (see [43] for details). Figure 2.13 shows a simulation of a tumor growth obtained in a two-dimensional domain where the top-half part is suitable for invasion. Accordingly, asymmetric invasion of the ECM is achieved by the cancer cells.

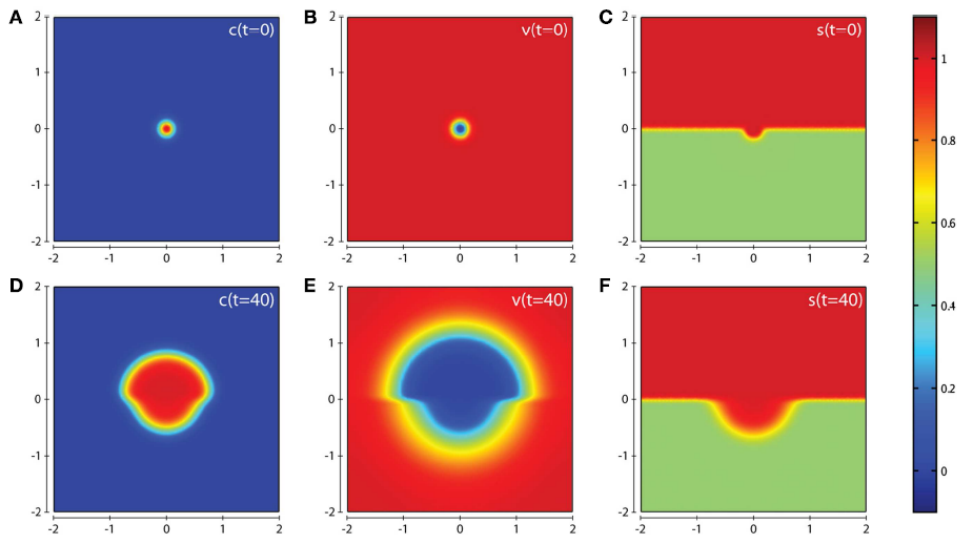


Figure 2.13: Evolution of a 2D tumor. Plots (A-C) show show the initial values of the cancer cell and ECM densities as well as the initial lay out of the matrix suitability modifier. Plots (D-F) show their resultant profiles at $t=40$. (Extracted from [43]).

The mathematical model characterized by (2.22) has 14 parameters associated with the local dynamics of the paracrine signaling pathway and more than 50% have to be estimated. Aiming to include the net effect of the matrix degrading enzymes on the tumor growth and on the extracellular matrix remodeling in such way that the amount of parameters is reduced, we consider a sub-class of the phase field tumor growth model developed in [77]. Suppose now consider that the mixture is composed of six constituents volume fractions:

- ϕ_T - tumor cell (proliferative, hypoxic and necrotic);

- ϕ_C - healthy cell;
- ϕ_σ - nutrient-rich extracellular water volume fraction;
- ϕ_{σ_0} - nutrient-poor extracellular water volume fraction;
- ϕ_{MDE} - matrix degrading enzymes (MDE) rich extracellular water;
- ϕ_{MDE_0} - matrix degrading enzymes (MDE) poor extracellular water.

As usual, the mixture is assumed saturated, i.e.,

$$\phi_T + \phi_C + \phi_\sigma + \phi_{\sigma_0} + \phi_{MDE} + \phi_{MDE_0} = 1.$$

Here ϕ_{MDE} represents the net balance between all active metalloproteinases and associated inhibitors while ϕ_{MDE_0} represents the inactive enzymes. Assuming similar hypothesis as in Section 2.5.1 and denoting by $v(x, t)$ the extracellular matrix density, the mass balance of mass defined in $\Omega \times (0, T]$ reads:

$$\left\{ \begin{array}{l} \frac{\partial \phi_T}{\partial t} = \nabla \cdot (M_T \phi_T^2 \nabla \mu - \chi \phi_T \nabla v) + \lambda_{prol}^T \phi_\sigma \phi_T - \lambda_{apop}^T \phi_T \\ \mu = \psi'(\phi_T) - \varepsilon^2 \Delta \phi_T \\ \frac{\partial \phi_\sigma}{\partial t} = \nabla \cdot D_\sigma(v) \nabla \phi_\sigma - \lambda_{prol}^T \phi_\sigma \phi_T + \lambda_{apop}^T \phi_T \\ \frac{\partial \phi_{MDE}}{\partial t} = \nabla \cdot D_{MDE}(v) \nabla \phi_{MDE} + \lambda_{prod}^{MDE} \phi_T (1 - \phi_{MDE}) \\ \quad - \lambda_{decay}^{MDE} \phi_{MDE} - \lambda_{decay}^{ECM} v \phi_{MDE} \end{array} \right. \quad (2.22)$$

The model is closed by adding the following differential equation for the extracellular matrix:

$$\frac{dv}{dt} = -\lambda_{deg}^{ECM} v \phi_{MDE} + \lambda_{rem}^{ECM} \phi_T (1 - v). \quad (2.23)$$

The tumor cells now grow according to the nutrient supply and die by natural apoptosis. The dead cells are assumed to be incorporated to the system immediately by lysing. Matrix degrading enzymes present a natural decay and are produced by tumor cells so that the growth levels off in regions where the ϕ_{MDE} approaches the maximal volume fraction. As in (2.21), the extracellular matrix is non-motile; it is degraded by the net action of the enzymes and is continuously remodeled by tumor cells if there is enough

space. Finally, the model points out to a dependence of diffusion coefficients on the ECM structure, a characteristic of heterogeneous ECM [72]. Figure 2.14 shows the evolution of the tumor as the result of similar conditions of the dynamics presented in Figure 2.13. Although the phase-field model requires only 3 parameters associated with the local dynamics, it is able to represent the general interplay among the matrix degrading enzymes and the extracellular matrix.

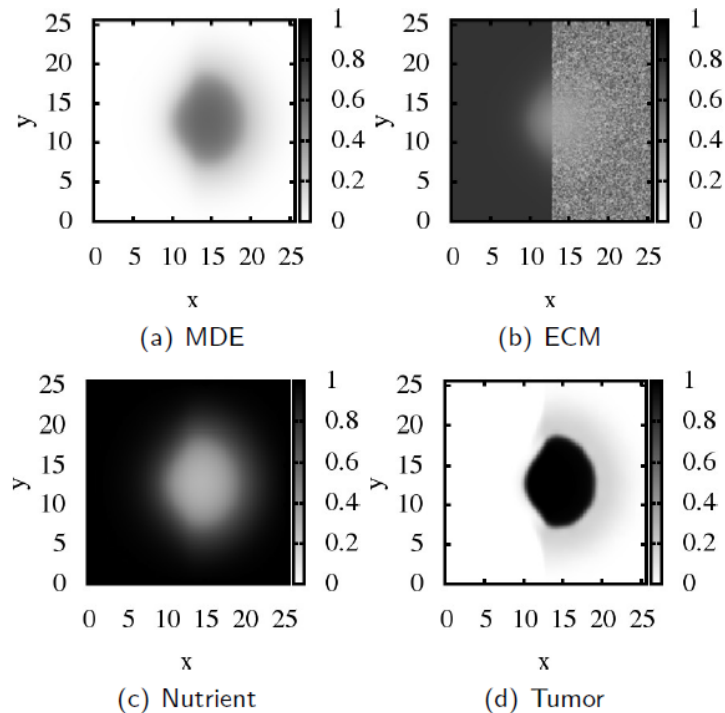


Figure 2.14: Evolution of a 2D tumor. Similar conditions as in Figure 2.13.

2.8 Angiogenesis Models

Angiogenesis, a physiological process through which new blood vessels are formed from a pre-existing vascular network, is involved in many pathological situations such as atherosclerosis, diabetes and cancer. As a cancer hallmark, it plays a critical role in almost all cancer progression and results from lack of nutrients and oxygen that halts the growth of avascular tumors and induces hypoxia. This gives rise to a complex interplay of paracrine signals, involving different types of cells, such as endothelial cells, and extracellular matrix, that ultimately lead to the establishment, maturation, and

remodeling of new blood vessels. [11] describes a series of distinct growth factors and inflammatory stimuli and their roles in endothelial cells activation and ECM degradation. Moreover, even when the role of this stimuli is recognized, the crosstalk among the pathways introduces huge complexity. Consider, for example, the VEGF: it is the main angiogenic factor in EC activation and VEGF signaling is itself mediated by two other endothelial cell-selective RTKs (receptor tyrosine kinases). It also worths mentioning that the complete angiogenic functions of VEGFs have not been totally dissected yet [11]. On the other hand, a full picture of the integration of these pathways is crucial for therapeutic exploration, as an intervention in one pathway may induce a wide range of consequences to other pathways [64].

There are many continuum and discrete mathematical models of angiogenesis available in the literature. The general mathematical methodologies of modeling angiogenesis can be found in Mantzaris et al. [87]. Recent accounts on the role of cell signaling, molecular aspects and whole organ modeling on the tumor angiogenesis is provided in [64]. In this section, which closely follows the work presented in [77], we review some modeling approaches and present a hybrid model developed by members of the TMG group. The first discrete model of angiogenesis was proposed in Stokes and Lauffenburger [124], in which each sprout is treated individually and the evolution of the tip velocity is modeled by a stochastic differential equation. This allowed to track the heterogeneity of the tumor vascular network. This feature is not prevalent in existing continuum models. Anderson and Chaplain [7] have followed a different approach involving first discretizing a two-dimensional continuum model using finite differences and then introducing a discrete algorithm that assigns probabilities of advancing vascular cell sprouts that accounts for progressive diffusion, chemotaxis, and haptotaxis. This methodology was incorporated in a phase-field tumor growth model in Frieboes et al. [53] to capture in a hybrid model the complex interplay of multiscale phenomena occurring at cellular-scales and their influence on tumor macro-scale as a mechanism that promotes morphological instability. An interesting continuum model was developed by Sun et al. [127, 128] that uses a capillary indicator function to describe the capillary network structure and account for heterogeneity and anisotropy of the conductivity of the extracellular matrix. Coupled with a discrete description of the tip cell and associated velocity, this model is able to represent the morphology of the new capillary network such as branching and anastomosis.

More recently, two hybrid models of sprouting angiogenesis were developed in Milde et al. [90] and Travasso et al. [139]. The former is based on a particle-mesh representation of the blood vessels which is combined with a continuum description through diffusion-reaction equations of vascular en-

dothelial growth factor, endothelial stalk cells, matrix metalloproteinases and fibronectin. As pointed out in the previous section, proteases and some proteins play important roles in the cleavage and remodeling of the extracellular matrix that ultimately influences the endothelial cell migration pattern. The hybrid model developed in Travasso et al. [139] is based on the phase-field approach which encompasses the concentration of tumor angiogenesis growth factor and the position of capillary sprouts, and the activation of the tip cell phenotype in endothelial cells and the definition of its position and velocity are tracked by a discrete agent model. Such activation mimics the hypoxia effect through concentration and gradient of the tumor angiogenesis factor. The focus of the model is the formation of a new vascular network and the tumor itself is not modeled. A full hybrid model that represents the vascular tumor growth is presented in the following.

2.8.1 A Hybrid Ten-Species Phase-Field Model of Tumor Growth

In Section 2.5.1 a six species phase-field model for an avascular model is described. That model is a simplification of the complete model for the vascular tumor growth proposed by Lima et al. [77], where the mixture is composed of $N = 10$ constituents and the following volume fractions are added into the mixture:

- ϕ_{TAF} - TAF-rich extracellular water;
- ϕ_{TAF_o} - TAF-poor extracellular water;
- ϕ_e - proliferative endothelial cell;
- ϕ_{e_o} - non-activated endothelial cell.

The net tumor angiogenesis factor produced by hypoxic cells at a rate λ_{TAF} is denoted by TAF-rich extracellular water volume fraction. This growth rate depends on the microenvironment and mixture conditions so that the growth levels off when TAF-rich extracellular water volume fraction approaches its maximum value. The TAF-rich extracellular water volume fraction triggers the endothelial cells activation, which proliferates according with an uptaken volume-action coefficient α_{TAF} during angiogenesis. Both the proliferative of endothelial stalk cells and the TAF-rich uptaken by endothelial cells are regulated by the discrete angiogenesis model so that they are activated whenever TAF-rich volume fraction is higher than the activation threshold ϕ_{TAF_c} . New endothelial cells are generated at the proliferation rate $\alpha_P(\phi_{TAF})$ that depends on ϕ_{TAF} . When $\phi_{TAF} < \phi_{ref}$, this rate is given by $\alpha_P\phi_{TAF}$. Otherwise, there is a saturation in the proliferation so that this

rate reaches its highest value, $\alpha_P \phi_{ref}$. Finally, the proliferative endothelial cells provide an increase of the nutrient amount at a rate α_R . The growth levels off in regions where the nutrient approaches its maximum volume fraction. The source terms can be seen in details in Lima et al. [77]. Figure 2.8.1 depicts a scheme that includes the main model hypothesis. The tip cell components of angiogenesis progression is described by a discrete model (shown in blue). In this model, it is assumed that the tumor angiogenesis factor - TAF - plays the role of the key regulator of the tumor angiogenesis. It is released by the hypoxic cells and activates quiescent endothelial cells. The discrete model takes into account the vascular development, such as tip endothelial cell (tip cells) activation and sprouting of new vessels, based on the work developed in Travasso et al. [139].

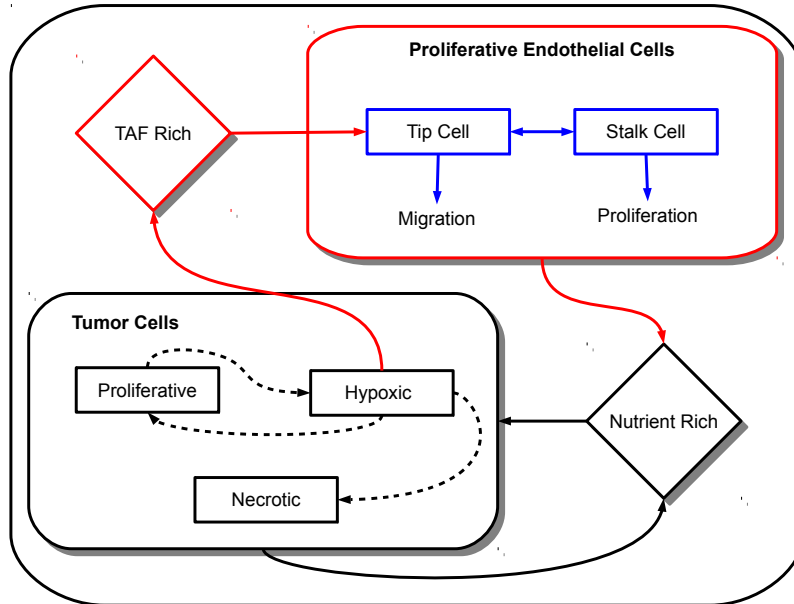


Figure 2.15: Conceptual scheme of the hybrid tumor growth model. The dynamics of tumor cells depends on the nutrient availability. In case of hypoxia, tumor growth factors are released. They eventually activate endothelial tip cell phenotypes, that promote the supply of nutrients to the tumor (after [77]).

The discrete part of the hybrid model is able to represent the angiogenesis process that leads to vascular remodeling is characterized by capillary sprouting, excessive, distorted and enlarged vessels branching, and large levels of endothelial cell proliferation [58], which are not captured by the continuum

model. The ABM takes into account the vascular development, such as tip endothelial cell (tip cells) activation and sprouting of new vessels [139]. In this discrete model, the activation of the tip cells is the result of their response to the environment through the TAF regulatory process [139]. Each activated tip cell is a movable discrete agent with associated velocity and path at a given time. As the sprouts migrate through the system, the stalk endothelial cells behind tip cells proliferate yielding sprout extension so that they define the morphology of the new growing sprouts, mediated by the extracellular matrix. Different types of tissues and layered orientation of the extracellular matrix have crucial role on the direction of the movement of the tip cell since they might exert stronger resistance for a sprout branching in some directions and weaker in others. Although the present model does not include the signaling mechanisms associated with the degradation and remodeling of the ECM, the mechanisms on the movement and further extension of capillary sprouts are included in the model through the heterogeneity and anisotropy of the conductivity tensor of the extracellular matrix, as proposed in [127, 128]

The mechanism associated with the tip cell activation and movement is then defined by quite simple rules. Each activated tip cell moves chemotactically with a velocity that is proportional to the gradient of the TAF. For the tip cell activation, both ϕ_{TAF} and ϕ_e have to be large enough. The latter condition guarantees that the tip cell is inside the blood vessel and the former guarantees that there is enough TAF in the neighborhood of the endothelial cells to trigger differentiation of the phenotype. There is a minimum value of the gradient of ϕ_{TAF} to drive movement. Thus, a tip cell is activated if the following conditions are met:

1. $\phi_e > \hat{\phi}_e$;
2. $\phi_{TAF} > \phi_{TAF_c}$;
3. $|\nabla\phi_{TAF}| > G_m$;
4. No other tip cell in a distance d_t .

The last condition models the cell-cell contact dependent mechanisms that prevent the activation of two neighboring tip cells, also known by notch signaling [139]. The distance d_t is associated with the diffusion of the sources of angiogenic factor in the tissue. From all possible new tip cells satisfying those conditions, just one is selected at a time to be a new tip cell (randomly).

Finally, the selected tip cell will move with cell velocity, \mathbf{v}_{tip} . The modulus of the tip cell velocity is proportional to $|\nabla\phi_{TAF}|$ up to a maximum value

G_{max} , being defined as

$$\mathbf{v}_{tip} = \mathbf{K} \left[\chi \nabla \phi_{TAF} \left(1 + \left(\frac{G_{max}}{|\nabla \phi_{TAF}|} - 1 \right) \mathcal{H}(|\nabla \phi_{TAF}| - G_{max}) \right) \right], \quad (2.24)$$

where χ is the chemotactic response of the endothelial cells and \mathbf{K} is the conductivity tensor of the extracellular matrix. We assume that the medium is heterogeneous and anisotropic, so the tensor this tensor \mathbf{K} varies within position $\mathbf{x} \in \Omega$ and is non-diagonal. The extracellular matrix heterogeneity and orientation of microstructure ultimately drives the tip cell movement and is independent of time, as proposed in [127, 128]. The general symmetric second order tensor \mathbf{K} is of the form,

$$\mathbf{K} = \begin{bmatrix} K_{xx} & K_{xy} & K_{xz} \\ K_{xy} & K_{yy} & K_{yz} \\ K_{xz} & K_{yz} & K_{zz} \end{bmatrix} = k_h \mathbf{H} + \frac{k_h}{k_a} \mathbf{A}, \quad (2.25)$$

where \mathbf{H} and \mathbf{A} are the conductivity heterogeneity and anisotropy of the extracellular matrix, respectively, and k_h and k_a the associated measures. Here, in the absence of specific experimental data, the conceptual model of \mathbf{K} is built by defining a random vector function $\mathbf{v} = (v_x, v_y, v_z)$ at each point of the domain, such that $|\mathbf{v}| = 1$. Then we set $\mathbf{H} = \mathbf{v}\mathbf{v}^t$ and the anisotropic matrix \mathbf{A} is obtained from \mathbf{H} by a rotation of 90° about the 3-axis. We also assume that k_h is fixed and k_a is random. With these definitions, the tensor \mathbf{K} for a tri-dimensional domain is written

$$\mathbf{K} = k_h \begin{bmatrix} v_x^2 & v_x v_y & v_x v_z \\ v_x v_y & v_y^2 & v_y v_z \\ v_x v_z & v_y v_z & v_z^2 \end{bmatrix} + \frac{k_h}{k_a} \begin{bmatrix} v_y^2 & -v_x v_y & v_y v_z \\ -v_x v_y & v_x^2 & -v_x v_z \\ v_y v_z & -v_x v_z & v_z^2 \end{bmatrix}. \quad (2.26)$$

For simplicity, the angiogenesis model is evaluated at some time intervals of the continuum model, denoted by $\Delta t|_{AM}$. Once \mathbf{v}_{tip} is obtained, the new position of ϕ_{etip} is obtained by

$$\mathbf{x}_{new} = \mathbf{x}_{old} + \Delta t|_{AM} \mathbf{v}_{tip}, \quad (2.27)$$

where \mathbf{x}_{old} and \mathbf{x}_{new} are the original and updated positions of the endothelial tip cell. Finally, the endothelial cells volume fraction inside the tip cell path (ϕ_{etip}) provides the coupling between the continuum and the discrete model. Whenever a tip cell is selected, the endothelial cells volume fraction is assumed to that inside the tip cell path, which is a subset of the computational domain defined by a ball of radius R_{tip} , centered at \mathbf{x}_{new} .

To show the behavior of the hybrid model, two different experiments are shown for different initial configurations of the parent vessel and a tumor

mass centred in the middle of the computational domain. In the first case, a vertical straight vessel close to a corner of the domain is considered. In the second case, a curved vessel is allowed to cross the domain. Figure 2.16 shows snapshots of the proliferative endothelial cells alone and together with the tumor cells at $t = 13$ (first row) and $t = 16$ (second row). At $t = 13$, the sprouts reach the tumor and at $t = 16$ the tumor has some protrusions towards the capillary network which is attached to the tumor, promoting metastasis. Both the model and the computational framework used easily deal with general positions for the vessel, as shown in Figure 2.17. As in the previous case, Figure 2.17 shows snapshots of the proliferative endothelial cells alone and together with the tumor cells at $t = 13$ (first row) and $t = 16$ (second row). Since the vessel is closer to the tumor compared with the previous experiment, the onset of the angiogenesis is earlier, so that more sprouts are present at $t = 13$. The additional capillary network speeds up the tumor growth, so that at $t = 16$ it is very well mixed to the tumor mass.

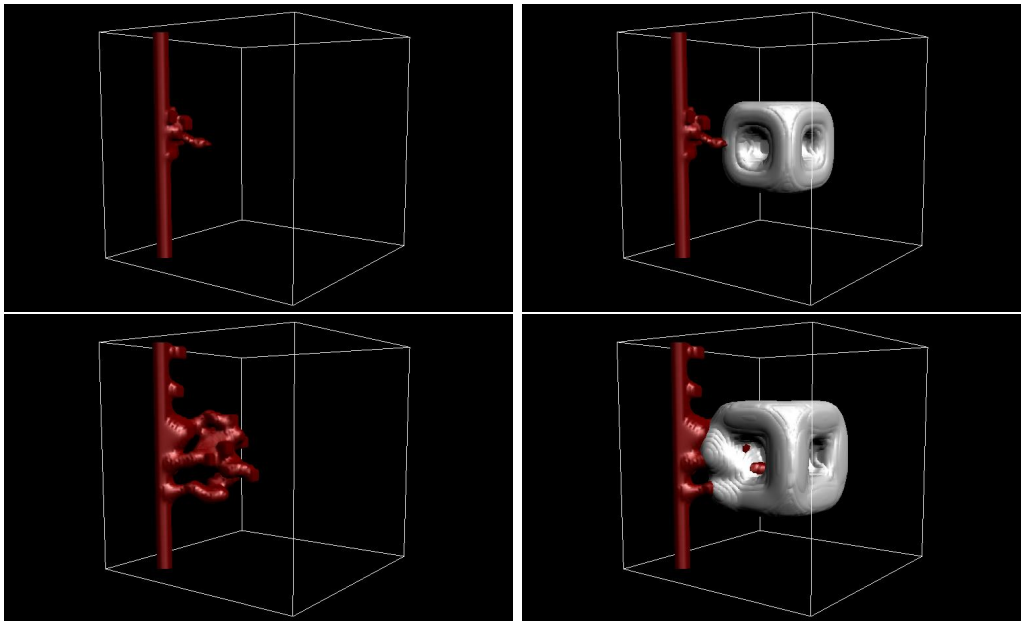


Figure 2.16: Angiogenesis in a three-dimensional domain with a straight parent vessel: snapshots of proliferative endothelial cells and ECs with the tumor cells at $t = 13$ (first row) and $t = 16$ (second row) (after [77]).

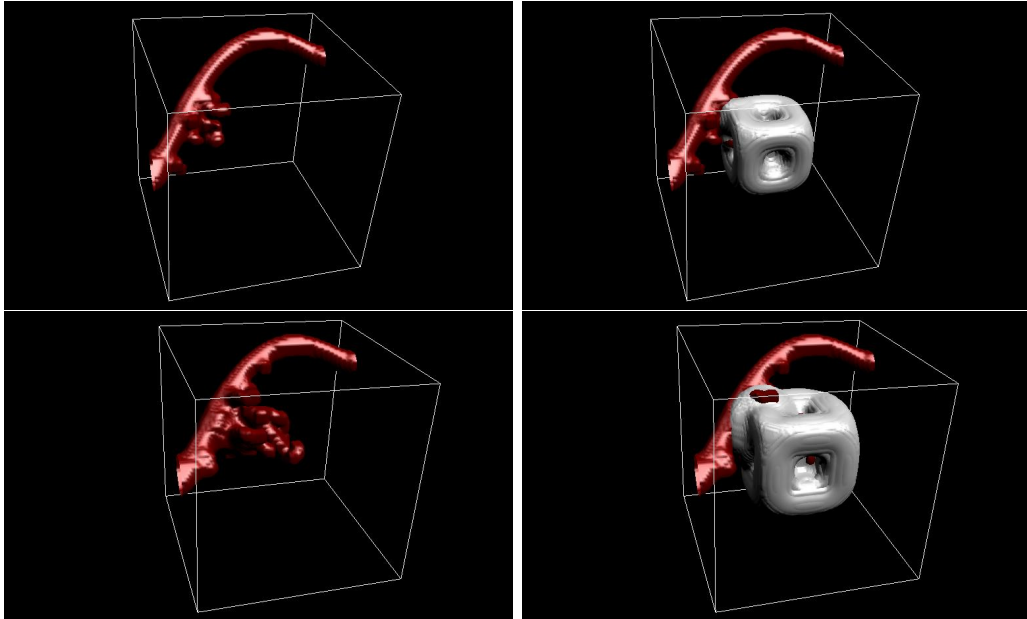


Figure 2.17: Angiogenesis in a three-dimensional domain with a curved parent vessel: snapshots of proliferative endothelial cells and ECs with the tumor cells at $t = 13$ (first row) and $t = 16$ (second row) (after [77]).

2.9 Stochastic Models

We now consider another important issue of the tumor growth: stochasticity. It is widely accepted that tumor growth can be regarded as a random process due to stochastic proliferation and differentiation of cells [136]. In fact, all biological processes are not purely deterministic since all systems are subject to random perturbations from the environment. Also, when modeling carcinogenesis, variables such as proliferation and apoptosis rates are approximated by data collected *in vitro*, that are intended to reproduce similar conditions *in vivo*. Obviously, these values are subject to many uncertainties. To disregard such uncertainties would lead to incorrect predictions which ultimately might suggest inadequate therapy. Consequently, to take into account such uncertainties, carcinogenesis should be modeled as a stochastic process [82]. Here, we review some works in the literature and present an efficient approach to deal with parametric uncertainties. This section closely follows the work presented in [78].

There are many ways to treat uncertainties in a variety of tumor growth stages [3, 4, 78, 79, 82, 84, 86, 94, 96, 107, 136]. Stochastic angiogenesis models are thought to be able to generate more realistic structures of capillary

networks [96]. Liotta et al. [79] developed a stochastic model of metastasis formation, that takes into account the fact that a great number of tumor cells can enter the circulatory system, but less than 0.1% survive to form metastasis. Mortality and natality rates can also be treated as random variables [82, 136]. In Lo [82], the action of various therapies was modeled to represent the suppression of growth of the tumor. In Naumov et al. [94], a cellular automata model for tumor growth was developed. In their work, the natural shrinkage in tumors is considered as a stochastic process. They assume that a cell size is reduced to one-third of its original size under necrosis. A stochastic rule is used to determine that only one-third of all cells become necrotic and, due to the accompanied shrinkage, the remaining empty space represents the reduction of the tumor size.

Hybrid stochastic models have also been proposed which employ cellular automata models with probabilistic transition rules [84, 86, 107]. In the model proposed by Macklin et al. [84], the cells transition rules from one state to another are stochastic, with the probability given by an exponentially-distributed random variable. Quaranta et al. [107] modeled tumor invasion of surrounding tissue through partial differential equations and a stochastic cellular automata model (*random-walk model*) to depict cell migration and cell-cell interactions. In Mallet and De Pillis [86], a hybrid cellular automata model combined with a model involving partial differential equations was presented to model the interaction between tumor cells and the immune system. In this model, a reaction-diffusion equation is used to describe the distribution of two chemicals necessary for mitosis and cell survival. Among the stochastic processes considered in the cellular automata, the death of tumor cells due to insufficient nutrients and actions of the immune system can be modeled as well as tumor and immune cell division and migration [86].

2.9.1 A Stochastic Six-Species Phase-Field Model of Tumor Growth

In [78], the effects of the uncertainties in some input parameters of a six-species phase-field model were studied. This kind of study helps to understand the impact of measurement errors and patient-specific data variation on the model. This idea is described here with more details. A sensitivity analysis of the model is performed in the attempt to identify the more influential parameters on the tumor mass growth. The uncertainty of the most influential parameter on the model output is then quantified by the stochastic model.

A model-free sensitivity analysis is performed by selecting only six parameters that are believed to yield relevant variations in the QoI (tumor

volume), in order to avoid increased complexity. The uncertainty analysis is performed through a \mathcal{N} -dimensional Monte Carlo analysis and the sensitivity analysis is performed by producing scatterplots through projections of the obtained \mathcal{N} values of the selected QoI against the \mathcal{N} sampled values of each parameter. Each resulting cloud of points yields a different pattern over the range of the uncertain parameter on the abscissa. A more uniform pattern indicates that the parameter plays a smaller role on the QoI while a more defined shape indicates higher correlation or higher influence of the parameter [115].

Lima et al. [78] conducted $\mathcal{N} = 300$ simulation runs that were enough to provide reasonable scatterplots shapes. Figure 2.18 shows the scatterplots for $t_2 = 10$. Clearly, they show that the tumor mass evolution is more sensitive to the rate of proliferative cellular mitosis λ_P than it is to the nutrient mobility. The dependence of the tumor mass evolution regarding the remaining parameters is less clear. Despite slight differences on the clouds patterns, all of them are almost equally less important.

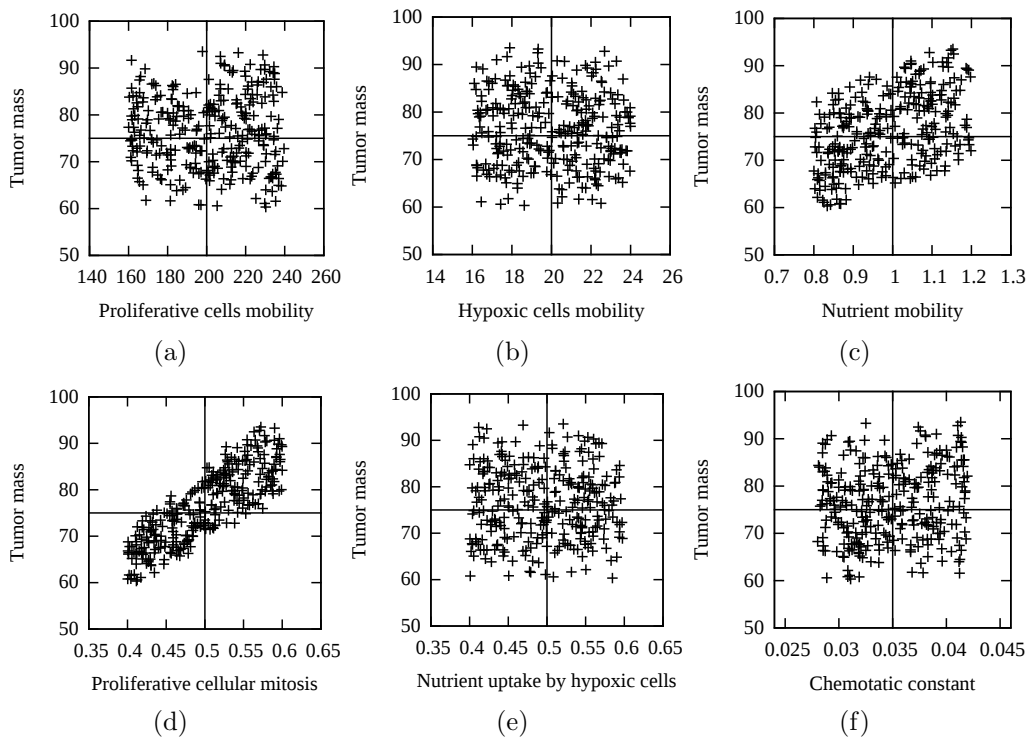


Figure 2.18: Scatterplots of tumor volume versus parameters at time $t_2 = 10$ (after [78]).

The Stochastic Collocation (SC) method is then used to solve the sys-

tem of stochastic partial differential equations (SSPDE). It is a non-intrusive methodology, basically involving a deterministic sampling [154] and the deterministic code is employed to obtain the result for each specific set of samples. Afterwards, the stochastic solution can be estimated. More details about the implementation and methodology can be seen in [78]. The uncertainty quantification is performed by considering that the rate of proliferative cellular mitosis has a uniform distribution $\mathcal{U}[0.4, 0.6]$. For the same problem defined in Section 2.5.1, Figure 2.19 compares the expected value of the tumor volume fraction resulting from the random proliferative cellular mitosis (in red) with that obtained by using a fixed value for the proliferative cellular mitosis (deterministic case (in green) with proliferation rate equal to 0.5) at $t = 13$. Clearly, the tumor volume fraction is underestimated in the deterministic case. This quite simple example highlights the fundamental role that uncertainty quantification plays on the quality (or confidence level) of model predictions. In this case, a smaller tumor volume fraction evolution characterized by the deterministic model would eventually lead to dosage errors in planning therapeutic strategies, possibly yielding underestimated treatment protocols.

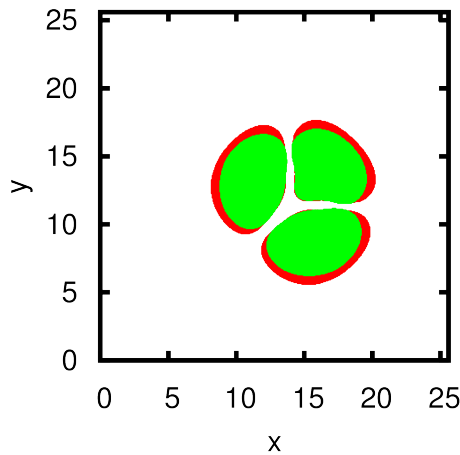


Figure 2.19: Tumor cells at $t = 13$. In red the mean result for the random problem, in green the deterministic problem when the proliferation rate is 0.5 (after [78]).

2.10 Multiscale Computational Methods and Challenges [50]

Multiscale methods are specially designed to develop models that are capable of linking molecular, cellular, and tissue scales. The common approach taken in constructing a mathematical model is to begin with a simple model. This model will preserve enough biology to be meaningful, but will include less parameters [116] as to not over complicate the modeling process. The advantage of this approach is that the model can be applied to understand many different biological systems. A mathematical model that incorporates multiple scales can serve at least two purposes: (1) when detailed information about the biological system is known, the model can be used to conduct *in silico* experiments in lieu of *in vitro* or *in vivo* experiments; and (2) when details are unknown, the model can serve as a tool to test a hypothesis and create a prediction. Extensions and complications can be included into the mathematical model, in the form of additional parameters, to better resemble the biological system [116]. However, it is necessary to avoid over-complicating the model.

The ultimate goal of multiscale mathematical modeling is to couple discrete particle methods (e.g., molecular dynamics) with models at the continuum level. However, coupling of these two methods is difficult because of the interaction between the interfaces between molecular dynamics and continuum regions. When applying the energy-conservation formulation, this discrepancy is amplified by causing heat generation in the molecular dynamics regime thereby polluting the solution. Another issue in coupling molecular dynamics and continuum methods is in connecting time scales in each region. Several researchers have developed multiscale methods to account for these issues to efficaciously bridge between temporal and spatial scales. The following is a brief overview of commonly used multiscale modeling approaches in the literature.

Bridging Scale Methods

The bridging scale method is a concurrent multiscale method that couples the atomistic and continuum simulation methods [81]. The feature of this method is that it is general and can be used in a full three dimensional domain. At its basic level, the bridging scale method includes the numerical calculation of the time history kernel in multiple dimension so that a two-way coupled coarse and fine molecular dynamics boundary condition is determined [81]. This approach is particularly suitable for dynamics systems with finite temperature [81].

Bridging Domain Methods

The bridging domain method uses molecular dynamics in localized regions then couples it with a continuum region that surrounds the atomistic region [153, 155]. A spatial region contains overlapping continuum and atomistic regions which is best demonstrated by two dimensional wave and crack propagation scenarios [81].

Quasi-Continuum Methods

Using the Cauchy-Born rule [129], which assumes that the continuum energy density can be estimated using an atomistic potential, the analysis at the atomic level is coupled to the continuum in the Quasi-Continuum method [134]. This approach is similar to an adaptive finite element method [100] which requires that the restriction that the deformation of the lattice of continuum point must be homogeneous [81].

Coupled atomistics and discrete dislocation

Coupled atomistics and discrete dislocation (CADD) is a method for quasi-static coupling [81]. This approach to multiscale modeling couples molecular statics with discrete dislocation plasticity [41, 118, 119], thus making it an especially useful tool in fracture mechanics. Defects such as dislocations generated within the atomistic region pass through to the continuum region where they are characterized by discrete dislocation mechanics [81, 141].

*Macroscopic, atomistic, *ab initio* dynamics*

The macroscopic, atomistic, *ab initio* dynamics (MAAD) multiscale method concurrently links tight binding, molecular dynamics, and finite element methods [1]. All three methods are computed simultaneously and dynamically share and receive information. The approach decreases the mesh size of the finite element mesh until it is on the order of the atomic spacing. Atomic dynamic are then governed by molecular dynamics, then tight binding is used to simulate the atomic bond breaking processes at an area of interest such as a crack tip [81].

Course-Grained Molecular Dynamics

Coarse-grained molecular dynamics (CGMD) is a multiscale approach similar to MAAD but instead couples only finite element and molecular dy-

namics [113]. It is possible to eliminate the tight binding analysis because the coarse-grained energy approximation converges to the exact atomic energy that is used to derive the governing equations of motion [81].

2.10.1 Proposed Multiscale Modeling Framework

A general multiscale tumor model can be constructed that spans three distinct scales. At the tissue level a continuum mixture model where the biological tissue is represented as a mixture of multiple constituents is introduced to describe the dynamics of the tissue (e.g. proliferative, hypoxic, necrotic, and healthy) and chemical (e.g. nutrient) and extracellular matrix. Each of such constituents, in their solid or liquid phase, are represented by either the volume fraction or the concentration. The constituents interact with each other through mass and momentum exchange. In Figure 2.20, the solid arrows indicate the mass and momentum exchange while the dotted arrows indicate information exchange. The interstitial fluid pressure is derived from the restriction applied by the volume fraction of the total mixture. The velocities of the solid tissue structure are solved using momentum balance equations accounting for both tissue anisotropy and nonlinear behaviors. The interstitial fluid velocity is solved using the balance of momentum in the quasi static Darcy formulation. The momentum exchange between the solid and liquid constituents is modeled based on the Coleman-Noll procedure by employing the entropy inequality [34, 35] so that the proposed model is thermodynamically consistent. The system of partial differential equations are solved using finite element techniques. To bridge the spatial scales, each finite element is discretized into virtual cells at the microscopic scale to model cellular growth by using agent-based statistical model to determine various cellular level activities such as the phenotypical alteration, cell division, etc. The geometry of each element and the local volume fraction and concentration of each constituents is solved at the tissue level are fed into the cellular level at each time step. In this level, the individual cell activity and viability are computed based on the availability of the nutrient and the signaling pathways computed at the sub-cellular level. The Viability factor will determine if each individual cell survives or not. The cell activity factor dictates if the cell proliferates or becomes hypoxic. If the cell activity reaches a certain threshold, the cell undergoes mitosis and divide into two. The spatial occupation i.e. the proliferation direction is dictated by the interstitial fluid pressure. At the sub-cellular geno-proteomic level, DNA/RNA-driven gene mutation and proteomic pathways related to cancer growth are accounted for. The individual cell activity and the local interstitial fluid pressure are used to determine the genetic mutation. The signaling pathways are then

triggered from the gene expression and a protein regulatory network. The signaling pathways control the growth factors to dictate the cell activity and viability and affect the cell phenotype.

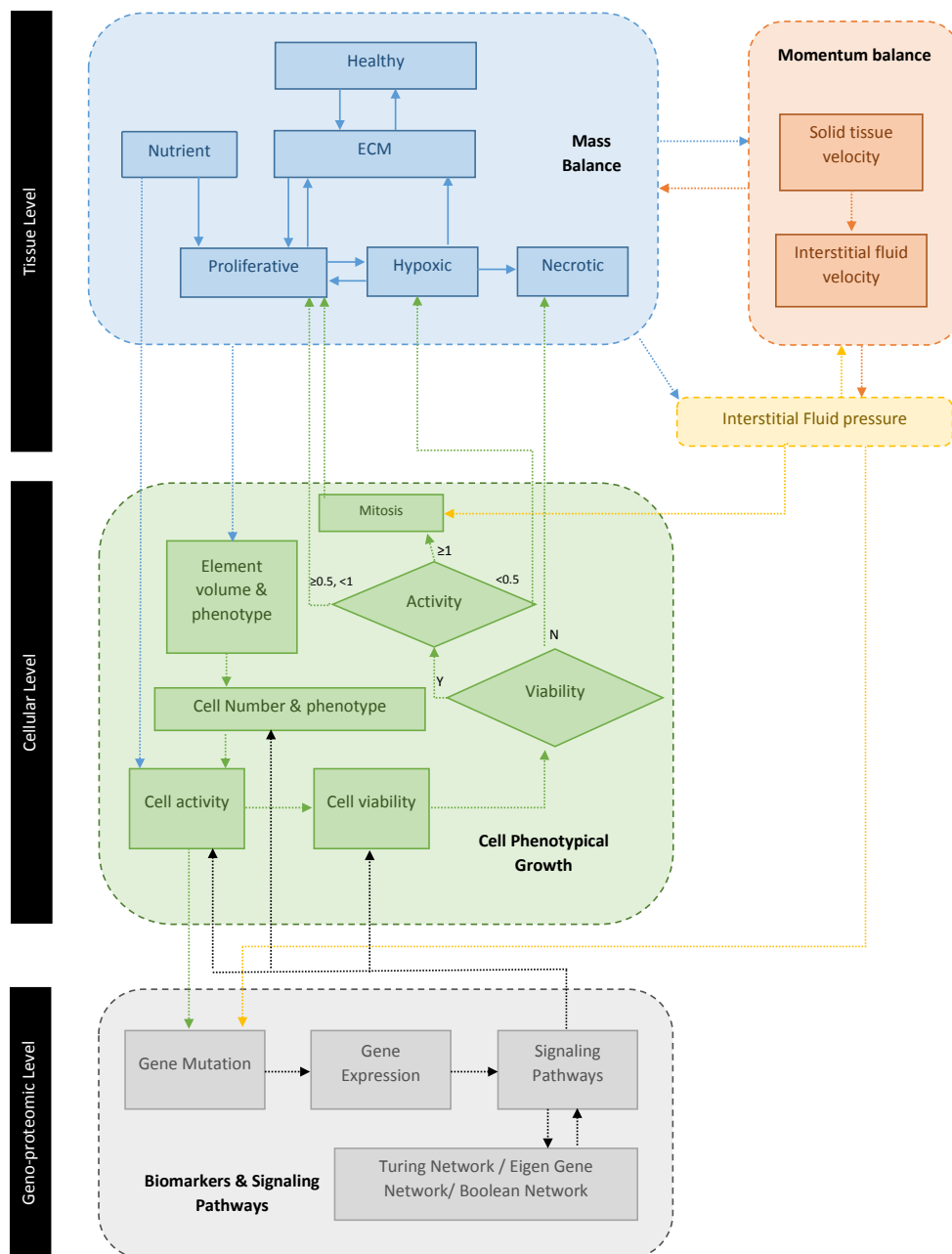


Figure 2.20: A framework for multiscale cancer modeling.

3 Model Calibration, Validation and Selection in the Presence of Uncertainties

Given the multitude of different models for events occurring at different spatial and temporal scales described in the preceding chapters, the inevitable question that arises is their reliability as a means of forecasting physical reality. This is a daunting question, as every phase of the prediction process must cope with uncertainties-in data, in parameters, and most importantly, in the selection of model itself. The successful use of computational models depends upon several fundamental concepts and processes:

1. *mathematical (computational) model* – The model is a manifestation of a scientific theory cast in mathematical structures that are intended to provide a meaningful abstraction of reality. Many examples are mentioned in the previous chapters. For a given theoretical framework, one can determine a number of models, each differentiated from the others by different hypotheses put forward to explain observations, different simplifying assumptions and then by specific values of the parameters that define the model. In a typical statistical setting, the model provides a map of parameters into observables and these observables can be recorded at several different levels: *in vitro* experiment, *in vivo*, etc.
2. *quantity of interest (QoI)* – It is important to specify in advance the particular QoI's of the physical event of interest. The notion of QoI's recognizes that the goal of a given prediction is not necessarily the global solution of the problem, but particular features of that solution. These QoI's represent the key drivers for the development and selection of mathematical models for computing.
3. *data* – Experimental observations are necessary for two fundamental purposes: 1) to identify the values of the model parameters for the specific physical environment in which the events of interest take place and 2) to determine, if only subjectively, whether the model is capable of faithfully predicting the QoI's with sufficient accuracy. The first of these is referred to as the *calibration process*. It involves solving an inverse problem for the parameters based on the observations. The second is referred to as the *validation process*. Validation involves experimental observations, obtained from more complex scenarios than those involved in the calibration process, in order to verify that hypotheses of the theory hold for regimes that are different from those considered during calibration. Roughly speaking, calibration generally is done with *in vitro* data while validation relies on *in vivo* behaviors, but exceptions to this exist.

Thus, implicit in predictive computational modeling is that experimental data must be acquired and integrated into computer codes in order to calibrate the models and test their validity. We describe a unique laboratory (the TEL) developed for tumor model calibration and validation in Chapter 4. One way to address uncertainties in data, parameters, and model selection is to call upon probability theory as a means of assigning probabilities to these objects. We adopt such probabilistic approaches throughout our investigations. But what probability theory? As is described in subsection 3.2, we subscribe to the logical probabilities of Cox [36] expanded by Jaynes [66] which provides a unified approach consistent with the “logical sciences”.

The treatment of uncertainty in predictive modeling involves three distinct processes: 1) the propagation of input uncertainties through the so-called forward model, itself a stochastic process, to quantify the uncertainties in QoI’s; 2) the statistical calibration process, in which probability densities of random model parameters and modeling errors in the theoretical structure are estimated using the measurement data, and 3) the validation process, which aims at determining whether or not the hypotheses of the model would hold for scenarios of interest and whether the model is capable of reliably predicting outputs with sufficient accuracy to be used in making critical decisions. Upon solving the stochastic forward problem for the QoI’s the uncertainties in the prediction must be quantified in some way to help establish a measure of confidence in the results.

For the purpose of determining the reliability of model predictions, we note that all parametric models, including those described in Chapter 2 along with boundary and initial conditions and constitutive relations, can be cast into an abstract problem, of finding a function u in a space of trial function ν , such that

$$A((\boldsymbol{\theta}, \mathcal{S}); u(\boldsymbol{\theta}, \mathcal{S})) = 0, \quad \boldsymbol{\theta} \in \Theta, \mathcal{S} \in \{\mathcal{S}_C, \mathcal{S}_V, \mathcal{S}_P\} \quad (3.1)$$

where A is the set of operators characterizing the model (e.g. (2.7)), $\boldsymbol{\theta}$ is a vector of parameters belonging to the parameter space Θ ($\subset \mathbb{R}^n$), \mathcal{S} is the scenario in which the model is implemented (the solution domain with boundary and initial condition), and $u(\boldsymbol{\theta}, \mathcal{S})$ is the solution vector for given $\boldsymbol{\theta}$ and \mathcal{S} . Various scenarios generally increasing in complexity, beginning with low-dimensional unit test environments (e.g. *in vivo* experiments) in the calibration scenario \mathcal{S}_C , progress to the full scale subsystem scenario (e.g. *in vivo* data) validation scenario, and progress to the full prediction scenario, \mathcal{S}_P . We shall refer to 3.1 as the *forward problem*. We may also consider classes of models A_i that could be employed to describe the different scales present in the physical system.

3.1 Parameter Sensitivity

Sensitivity analysis is a process designed to estimate the sensitivity of outputs to changes in parameters. Particularly, it determines how the change in input factors of a model, qualitatively and quantitatively, affects the variation and uncertainty in the model outputs. Quantitative sensitivity analysis may result in reduction in parameter space dimension, where the calibration is made, by providing the level of importance of each parameter than another. Parameters that do not appreciably influence outputs, particularly the QoIs can be discarded at given fixed (deterministic) values. Therefore, sensitivity analysis can be employed prior to calibration of complex models in order to decrease the large numbers of parameters or to determine the level of attention that must be given to experimental measurements of the calibration data.

A qualitative route to computing sensitivities is to construct scatterplots [115]. In this method, the parameters are randomly sampled and the computation model output $Y = Y(\theta_1, \theta_2, \dots, \theta_k)$ is computed. For each parameter, samples are compared directly to the value of Y . A parameter is considered to be “important” if a clear correlation between the parameter’s value and the output value can be seen in the scatterplot patterns.

Another approach is to employ variance-based methods in which the sensitivity pattern of a model is described by decomposing the variance $V(Y)$ of an output function into contributions from each of the parameters [40, 122, 123]. The total sensitivity indices are then estimated via,

$$S_{T_i} = \frac{E_{\theta_{\sim i}}(V_{X_i}(Y|\theta_{\sim i}))}{V(Y)}. \quad (3.2)$$

where, $\theta_{\sim i}$ is the input vector excluding the i th component θ_i , $V_{X_i}(Y|\theta_{\sim i})$ is the variance due to θ_i of the output produced by $\theta_{\sim i}$ and $E_{\theta_{\sim i}}$ is the conditional expectation of the model given $\theta_{\sim i}$. The indices S_{T_i} provide a measure of the sensitivity of each input factor on the total output variance.

Prior to calibration, sensitivity analyses can be employed for the tumor growth models described earlier. Variance-based sensitivity analysis are also important in designing calibration (*in vivo*) and validation (*in vivo*) experiments, as those parameters found to influence the QoIs (through sensitivity measures) must be capable of being measured in calibration and validation experiments.

3.2 A Bayesian Framework for Calibration, Validation and Prediction

Every stage of the calibration and validation processes encounters uncertainties in the model parameters $\boldsymbol{\theta}$, the scenario parameters \mathcal{S} , and the observational data \mathbf{D} . The problem of overriding importance is to characterize in a meaningful way all of these uncertainties, to trace their propagation through the various solution processes, and to ultimately determine and quantify the uncertainty in the target QoI's. We shall employ Bayesian approaches, based on contemporary treatments of statistical inverse analysis, such as those described in [19, 25, 26, 68, 80, 135, 137, 148]. One advantage of the Bayesian theory is that it provides an all-inclusive framework for identifying the essential features of a predictive model while also providing means to characterize uncertainty. The main premise of this theory is that of subjective or logical probability; the parameters $\boldsymbol{\theta}$, the observational calibration data \mathbf{D}_C , the observational validation data \mathbf{D}_V , and the theoretical model are not deterministic; they are random variables or processes characterized by probability density functions (pdf's), $\pi(\boldsymbol{\theta})$, $\pi(\mathbf{D}_C)$, and $\pi(\mathbf{D}_V)$. The model is thus transformed into a stochastic model. We express this by rewriting (3.1) symbolically in the form

$$A((\pi(\boldsymbol{\theta}), \pi(\mathcal{S})); u(\pi(\boldsymbol{\theta}), \pi(\mathcal{S}))) = 0 \quad (3.3)$$

which naturally implies that the solution u , and *a fortiori* the quantity of interest $Q(u)$, to be random as well.

Calibration: The calibration process enables one to identify model parameters based on calibration data \mathbf{D}_C obtained from a set of “simple” calibration scenarios \mathcal{S}_C . Since there are uncertainties in both the data and the model parameters, indicated by the vector $\boldsymbol{\theta}$, this becomes a statistical calibration process in which probability density functions given by Bayes’ formula [?]:

$$\pi_{\text{post}}^c(\boldsymbol{\theta}|\mathbf{D}_C) = \frac{\pi_{\text{like}}(\mathbf{D}_C|\boldsymbol{\theta}) \cdot \pi_{\text{prior}}(\boldsymbol{\theta})}{\pi_{\text{evid}}(\mathbf{D}_C)}. \quad (3.4)$$

In (3.4), $\pi_{\text{post}}^c(\boldsymbol{\theta}|\mathbf{D}_C)$ is the posterior pdf defining the Bayesian update of the prior information embodied in $\pi_{\text{prior}}(\boldsymbol{\theta})$, $\pi_{\text{like}}(\mathbf{D}_C|\boldsymbol{\theta})$ is the likelihood pdf, and the term

$$\pi_{\text{evid}}(\mathbf{D}_C) = \int \pi_{\text{like}}(\mathbf{D}_C|\boldsymbol{\theta}) \cdot \pi_{\text{prior}}(\boldsymbol{\theta}) d\boldsymbol{\theta}$$

the evidence seen to be the marginalization of the for given \mathbf{D}_C and a normalization factor (since $\int \pi_{\text{post}} = 1$).

Validation: The objective of the validation process is to challenge the model by testing the validity of the assumptions on which the full-system model is based; the process thus requires the consideration of new experimental scenarios \mathcal{S}_V designed to corroborate the model assumptions. A scenario \mathcal{S}_V provides new data \mathbf{D}_V that can be used for recalibrating the parameters. In the first step of validation, a new posterior pdf can thus be formed,

$$\pi_{\text{post}}^v(\boldsymbol{\theta}|\mathbf{D}_V, \mathbf{D}_C) = \frac{\pi_{\text{like}}(\mathbf{D}_V|\boldsymbol{\theta}) \cdot \pi_{\text{post}}^c(\boldsymbol{\theta}|\mathbf{D}_C)}{\pi_{\text{data}}(\mathbf{D}_V|\mathbf{D}_C)}. \quad (3.5)$$

where $\pi_{\text{data}}(\mathbf{D}_V|\mathbf{D}_C)$ is a new normalization constant. The prior is seen to be the posterior at the calibration scenario.

The second step of the validation process consists in comparing values of QoI's obtained from the stochastic model using $\pi_{\text{post}}^v(\boldsymbol{\theta}|\mathbf{D}_V, \mathbf{D}_C)$ and the observable value of this quantity obtained from experimental measurements and for a new scenario \mathcal{S}_P , the prediction scenario. If the differences between the values of QoIs is less than a given tolerance, we say the model is “not invalidated,” and one gains more confidence in the predictive capabilities of the mathematical model; otherwise, the model is invalid.

3.3 Model Selection: Posterior Plausibilities of Parametric Model Classes

Bayes' formula can be written to make explicit the whole set of assumptions underlying the modeling and inference efforts [15, 99, 103]:

$$\pi_{\text{post}}(\boldsymbol{\theta}_j|\mathbf{D}, \mathcal{P}_j) = \frac{\pi_{\text{like}}(\mathbf{D}|\boldsymbol{\theta}_j, \mathcal{P}_j) \cdot \pi_{\text{prior}}(\boldsymbol{\theta}_j|\mathcal{P}_j)}{\pi_{\text{evid}}(\mathbf{D}|\mathcal{P}_j)}. \quad (3.6)$$

In (3.6), \mathcal{P}_j denotes the j -th model class, which has associated with it a random vector $\boldsymbol{\theta}_j$ of model parameters, $j = 1, 2, \dots, m$. All m proposed model classes are “competing” to explain (match) the same collected data \mathbf{D} . A model class can be seen as the family of all possible values of $\boldsymbol{\theta}_j$, augmented with prior and likelihood pdfs.

In (3.6), the term

$$\pi_{\text{evid}}(\mathbf{D}|\mathcal{P}_j) = \int \pi_{\text{like}}(\mathbf{D}|\boldsymbol{\theta}_j, \mathcal{P}_j) \cdot \pi_{\text{prior}}(\boldsymbol{\theta}_j|\mathcal{P}_j) d\boldsymbol{\theta}_j \quad (3.7)$$

is denoted “model evidence”, and it reflects how likely one is to obtain a given data sample \mathbf{D} within the whole family of models $\boldsymbol{\theta}_j$ in \mathcal{P}_j . The model evidence can be used to update the ranking of model classes. Indeed, in

the set $\mathcal{M} = \{\mathcal{P}_1, \mathcal{P}_2, \dots, \mathcal{P}_m\}$ of competing model classes, let us say that we have an a priori plausibility $\rho_{\text{prior}}(\mathcal{P}_j|\mathcal{M})$ for each model class, with the constraint

$$\sum_{j=1}^m \rho_{\text{prior}}(\mathcal{P}_j|\mathcal{M}) = 1.$$

Having the experimental data, we can update such a priori ranking. The posterior plausibility $\rho_{\text{post}}(\mathcal{P}_j|\mathbf{D}, \mathcal{M})$ for each model class is also computed through a Bayesian updating procedure:

$$\rho_{\text{post}}(\mathcal{P}_j|\mathbf{D}, \mathcal{M}) = \frac{\pi_{\text{data}}(\mathbf{D}|\mathcal{P}_j, \mathcal{M}) \cdot \rho_{\text{prior}}(\mathcal{P}_j|\mathcal{M})}{\pi_{\text{data}}(\mathbf{D}|\mathcal{M})}. \quad (3.8)$$

In (3.8), the term

$$\pi_{\text{data}}(\mathbf{D}|\mathcal{M}) = \sum_{j=1}^m \pi_{\text{data}}(\mathbf{D}|\mathcal{P}_j, \mathcal{M}) \cdot \rho_{\text{prior}}(\mathcal{P}_j|\mathcal{M})$$

is the normalization value (for a given \mathbf{D}) that reflects how likely one is to obtain a given data sample \mathbf{D} within the whole family of model classes \mathcal{P}_j in \mathcal{M} .

3.4 The General Bayesian filtering

Bayesian methodology can be employed for real-time assessment of the system state evolution in the presence of dynamic data (i.e. the data that is acquired through time $t \in [0, \infty]$), so that we can inform ourselves for potential control actions to be taken on the system. For instance, the state might be concentration of tumor cells throughout a volume region and the control action can be a cancer treatment process. The initial state of the system is specified by the pdf $\pi(\boldsymbol{\vartheta}^{(0)})$. and the control is indicated by the vector $\mathbf{c} \in \mathbb{R}^{n_c}$, for some fixed positive integer $n_c > 0$. The measurement data $\mathbf{D}^{(1)}, \mathbf{D}^{(2)}, \dots$, are collected at instants $0 = t^{(0)} < t^{(1)} < t^{(2)} < \dots$. The Bayesian filtering consists of two steps:

- (a) [Prediction step] Having the calibrated (and validated) computational model, one might use an evolution equation in order to predict the state of the system, such as

$$\boldsymbol{\vartheta}_{\text{predict}}^{(k+1)} = \mathbf{f}^{(k+1)}(\boldsymbol{\vartheta}^{(k)}, \mathbf{c}^{(k+1)}, \mathbf{w}^{(k)}), \quad (3.9)$$

where $\mathbf{f}^{(k+1)}(\cdot, \cdot, \cdot)$ is an evolution function and \mathbf{w} denotes the state noise. Once the new state $\boldsymbol{\vartheta}_{\text{predict}}^{(k+1)}$ is predicted, one can also compute the next measurement $\mathbf{y}^{(k+1)}$.

- (b) [Correction step] Once the actual data $\mathbf{D}^{(k+1)}$ at $t^{(k+1)}$ arrives, Bayes' formula (3.10) is employed to statistically update the predicted state $\boldsymbol{\vartheta}_{\text{predict}}^{(k+1)}$, such as

$$\begin{aligned} & \pi_{\text{post}}(\boldsymbol{\vartheta}^{(k+1)} | \mathbf{D}^{(k+1)}, \mathbf{D}^{(k)}, \dots, \mathbf{D}^{(1)}) \\ &= \frac{\pi_{\text{like}}(\mathbf{D}^{(k+1)}, \mathbf{D}^{(k)}, \dots, \mathbf{D}^{(1)} | \boldsymbol{\vartheta}^{(k+1)}) \cdot \pi_{\text{prior}}(\boldsymbol{\vartheta}^{(k+1)})}{\pi_{\text{data}}(\mathbf{D}^{(k+1)}, \mathbf{D}^{(k)}, \dots, \mathbf{D}^{(1)})}. \end{aligned} \quad (3.10)$$

The recursive process (steps (a)-(b)) continue in order to real-time monitoring and control of the system state evolution. It is shown that this procedure, by addressing the noises in the data and uncertainty in the computational models, results in enhancement of predictive models of complex physical phenomena [104].

3.5 Example: Selection of Models of Tumor Growth

The Bayesian framework for model calibration and selection is employed by Oden et al. [99] to statistical assessment of continuum models of tumor growth. Particularly, two classes of tumor growth models based on phase-field theories of mixture are taken into account such as,

- \mathcal{P}_1 : Simple Proliferation
- \mathcal{P}_2 : Proliferation/Apoptosis, with Degenerate Mobility and Oxygen Dependence

In deriving both models, it is assumed that there are only two species, concentration $u(\mathbf{x}, t)$ of cancer cells in the tissue for any $\mathbf{x} \in \Omega_{\text{actual}}$ and any $t \geq 0$ and healthy cells n . For \mathcal{P}_1 , convective velocity is ignored and a simple, linear proliferation is assumed wherever there is species u . In \mathcal{P}_2 , the effects of oxygen are considered via a separate reaction diffusion-reaction equation, that is the tumor will only proliferate significantly if there is enough oxygen present.

The Bayesian methodology described above is then employed to determining the most plausible models in the set $\mathcal{M} = \{\mathcal{P}_1, \mathcal{P}_2\}$ of candidate models which compete to better simulate a given data set \mathbf{D} .

The reference data \mathbf{D} used in this study is fabricated with a model \mathcal{P}_{ref} that is different, and presumably more sophisticated, than the \mathcal{P}_1 and \mathcal{P}_2 . Particularly, \mathcal{P}_{ref} is a four species model accounting for tumor cells, healthy cells, nutrient-rich extracellular water, and nutrient-poor extracellular water. Figure 3.1 shows the simulation results of \mathcal{P}_{ref} in terms of the concentration of cancer cells u in the tissue.

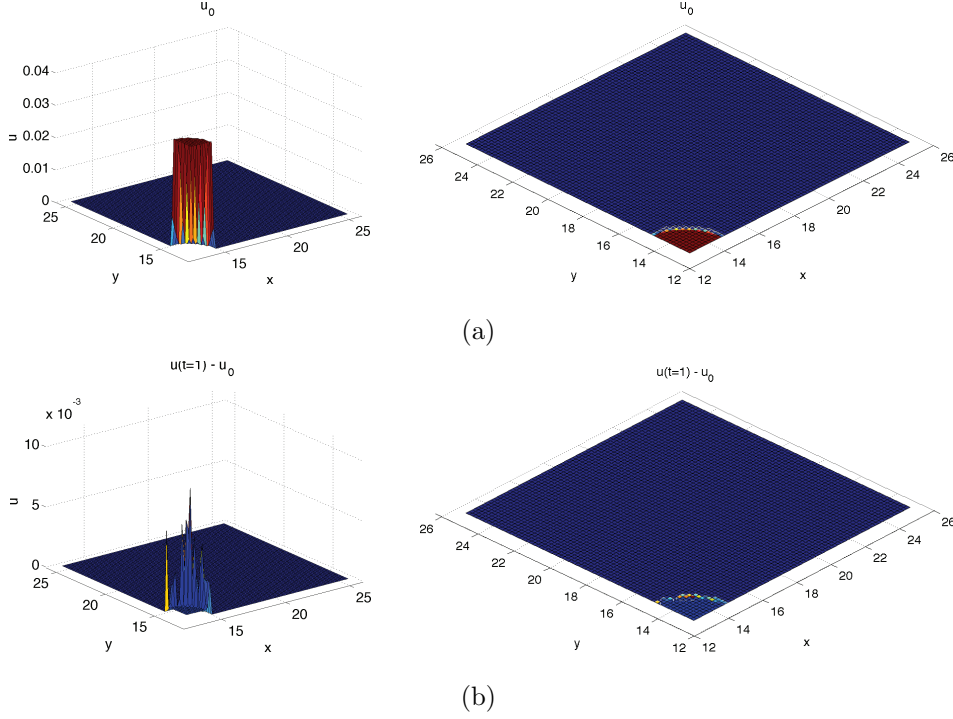


Figure 3.1: The synthetic images of the tissue obtained from \mathcal{P}_{ref} . The physical domain corresponding to a tissue is the square $\Omega_{\text{actual}} = (0, 25.6) \times (0, 25.6)$: (a) Initial state of tumor cells concentration $u_0 = u(\mathbf{x}, 0)$, the tumor is located in the left-lower corner of the domain. (b) Change in the tumor cells concentration over time $u(\mathbf{x}, t) - u_0$ at $t = 1$, the tumor cells grows in the domain [99].

This synthetic data, together with (3.4) are used for statistical calibration of the proliferation rate parameter P in both models. Figure 3.2 shows the computed posterior pdfs of the $\theta_1 = P$. Moreover, assuming equal prior plausibilities of $\rho_{\text{prior}}(\mathcal{P}_j | \mathcal{M}) = \frac{1}{2}$ for each model, the posterior plausibility is computed from (3.8) such as

$$\rho_{\text{post}}(\mathcal{P}_1 | \mathbf{D}, \mathcal{M}) \approx 1 \quad \text{and} \quad \rho_{\text{post}}(\mathcal{P}_2 | \mathbf{D}, \mathcal{M}) \approx 0$$

It should be noted that the worse posterior plausibilities of \mathcal{P}_2 should not be interpreted as a sign of the inappropriateness of the corresponding governing equation, but rather of our choices: which parameters to treat deterministically in \mathcal{P}_2 , as well as of which values to give them.

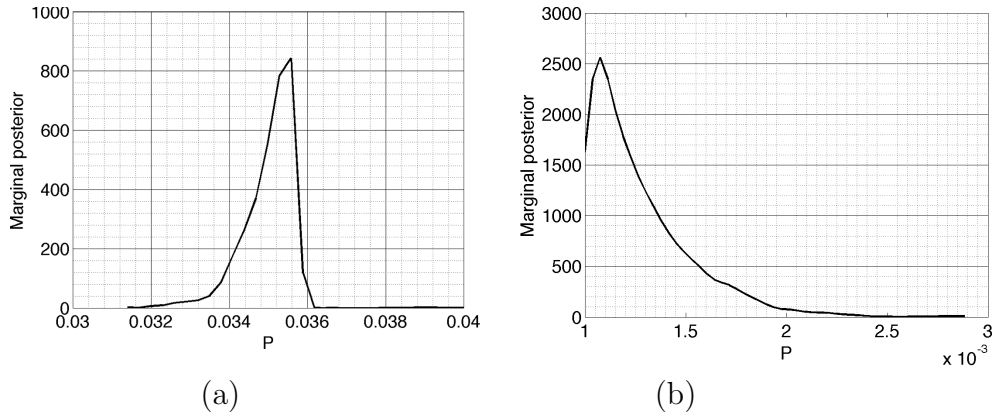


Figure 3.2: Posterior marginal pdfs for: (a) model \mathcal{P}_1 , (b) model \mathcal{P}_2 [99].

All the calculations, including the solution of the statistical inverse problems through Bayesian formula and calculating evidences and other integrals is performed using QUESO [105] that utilizes Markov Chain Monte Carlo (MCMC) methods. Parallel computing is employed in all computational steps. More specifically, the Lonestar computational platform at the Texas Advanced Computing Center (TACC [133]) is employed in this study.

4 Experimental Calibration and Validation of Tumor Growth Models: The Rylander Tumor Engineering Laboratory

A new research laboratory has been constructed to develop *in vitro* platforms specifically dedicated to calibration and validation of a wide collection of tumor growth models. The laboratory captures novel physiologically representative 3D tumor platforms (solid 3D matrices, single and dual channel vascularized microfluidic tumor platforms, and platforms with vascularized networks incorporated) for studying the influence of cell-cell and cell-matrix interactions and key biomechanics of tumors, including matrix stiffening due to desmoplasia, increased compressive force resulting from growth-induced solid stress, and greater interstitial fluid pressure and altered fluid flow patterns due to abnormal vasculature and lack of functional lymphatics. These platforms supersede traditional 2D cell monolayers, which do not recapitulate any of these features, and overcome the highly variable and frequently cost prohibitive use of animals for systematic and high throughput analysis critical for therapy development. These platforms are coupled with a high resolution confocal microscope to facilitate dynamic spatial and temporal imaging of tumor growth and response to stimuli in a controlled live cell incubation chamber for long term non-destructive analysis. The capability to perform high resolution spatial and temporal imaging with the confocal microscope is a very unique and new capability recently established at UT Austin. It is believed that the Rylander Tumor Engineering Laboratory can provide unparalleled insight into the dynamics and spatial nature of tumor growth. These first-of-their-kind platforms can be employed for unprecedented exploration of the influence of microenvironmental features on tumor growth and response to therapies while serving as an enabling technology for computational model development and refinement.

4.1 3D Solid Tumor Platform

Solid tumor platforms are based upon collagen I hydrogels seeded with MDA-MB-231 breast cancer cells, telomerase immortalized endothelial cells (TIME), and normal human dermal fibroblasts (NHDF) of varying densities as shown in Figure 4.1 [131, 132]. Briefly, MDA-MB-231 and NHDF cells are mixed in a neutralized collagen solution and allowed to polymerize at 37°C. Then, TIME cells are seeded on top of the collagen hydrogel and allowed to form a monolayer.

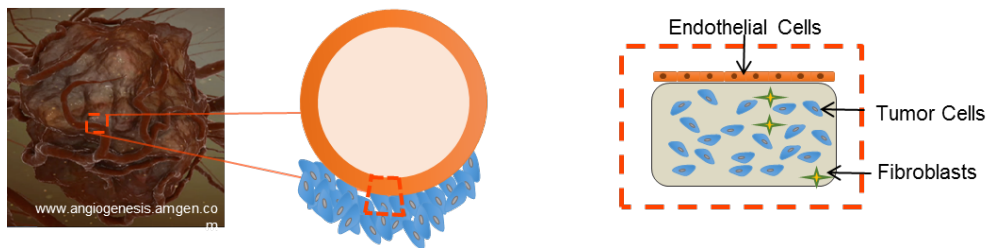


Figure 4.1: 3D collagen hydrogel composed of MDA-MB-231 breast cancer cells, NHDF fibroblasts, and TIME endothelial cells [131].

The hydrogel is composed of Collagen I, but can be customized to a stiffer or softer composition by changing the concentration of collagen used to compose the gel. Blends of other types of collagen can be incorporated to change the matrix mechanics. Additionally, the matrix can be customized by incorporating extracellular proteins such as fibronectin and laminin.

The current cellular system is composed of MDA-MB-231 breast cancer cells, NHDF fibroblasts, and TIME endothelial cells. This solid gel system can be altered to study behaviors of mono-culture, co-culture (MDA-TIME, MDA-NHDF, NHDF-TIME) and tri-culture cellular compositions. The growth characteristics of the tumor population can be varied by changing the initial seeding densities of each type of cell. Changes in cell density and compositions can dramatically influence cellular signaling and ultimately enable the influence of these conditions on hypoxia or angiogenesis to be investigated. Specifically by varying cellular composition from a mono-culture, co-culture, and tri-culture the effects of cell-cell interaction on cell proliferation, morphology, cell secretions, migration, and gene and protein expression can be elucidated. Other types of cancer cells such as brain or pancreatic cells can be incorporated and the matrix tuned to reflect the properties of these tumors.

4.1.1 Cell Viability, Proliferation and Morphology:

The population of live and dead cells can be determined by performing Calcein AM and Propidium Iodide staining which allows for simultaneous detection of live (fluoresce green) and dead cell (fluoresce red) populations. Calcein AM can be introduced in the system for 1 hr followed by a 10 min incubation with propidium iodide. Confocal microscopy will quantify the number and distribution of live/dead cells dynamically. Figure 4.2 shows the population of live and dead cells within a collagen platform. The properties of this platform have been tuned to create a necrotic core (red cells

throughout most the gel) with corresponding live cells (green) near the surface. **Toxicity** can be measured using Alamar Blue dye which is added to the system and incubated for 1-4 hrs at 37°C. Percent reduction in Alamar blue, which indicates the level of cellular activity, is analyzed with a plate reader. **Cell proliferation** can be determined by staining the cells with DAPI and counting the nuclei. **Cell morphology** can be analyzed by performing F-actin staining to denote cytoskeletal organization and imaged as published [131, 132].

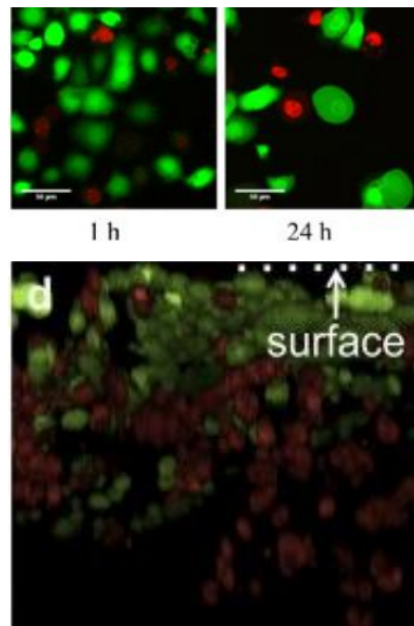


Figure 4.2: Live/dead staining of cancer cells Green: calcein, live cells; Red: Propidium Iodide, dead cells, Scale=50 μm .

4.1.2 Experimental Depictions of Angiogenesis

The solid gel collagen platforms can be cultured in a transwell system to study angiogenic sprouting. Transwell supports are hanging well inserts with a thin microporous permeable membrane on the bottom and impermeable side walls used for studies of anchorage dependent and independent cells. They utilize the permeable support to enable the physiologically representative transport, absorption, and secretion of signaling molecules and growth factors between different cell populations to explore the influence of their interactions on key processes such as angiogenesis, cell migration, and tumor growth. The transwell membranes are available in various sizes, diameters,

pore sizes, and membrane materials to permit fine tuning of them for specific applications and cell types.

A transwell-solid gel system with a co-culture of MDA-MB-231 and GFP fluorescently labeled TIME cells has been developed to study angiogenic sprouting (Figure 4.3a) [131, 132]. To create this system, MDA-MB-231 breast cancer cells and NHDF fibroblast cells were mixed in a neutralized collagen solution and allowed to polymerize in a transwell insert in a 12 well plate dish. After polymerization, endothelial cells were seeded on top of the collagen hydrogel and allowed to form a confluent layer. Media was then added to a well plate dish until it just passes the permeable membrane of the transwell insert and also on top of the endothelial layer in the insert as shown in Figure 4.3a. This system enables analysis of the secretion of factors associated with intercellular signaling between endothelial cells and breast cancer cells, and fibroblasts separately. Figure 4.3b illustrates other key applications such as cell migration/metastasis and angiogenesis that could be studied with this system. A transwell-solid gel system with a co-culture of MDA-MB-231 and GFP fluorescently labeled TIME cells has also been developed to study angiogenic sprouting. This system, has been used successfully to induce angiogenesis as shown in Figure 4.4. Sprouting was determined by imaging the system under a confocal microscope.

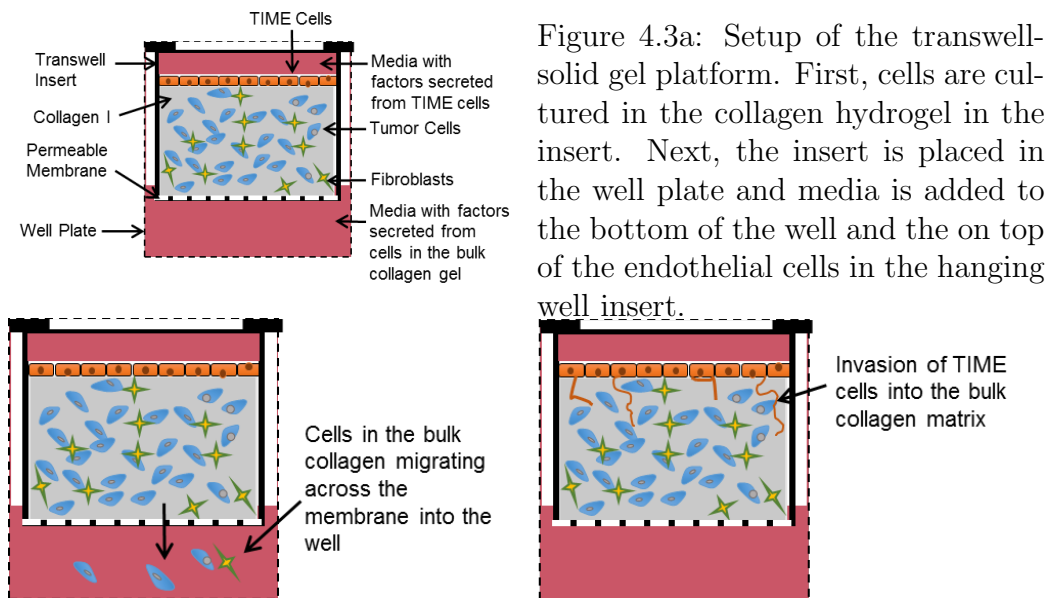


Figure 4.3b: Various applications for the Transwell-Solid-Gel platform. Left) Cell migration studies and Right) Angiogenesis characterization.

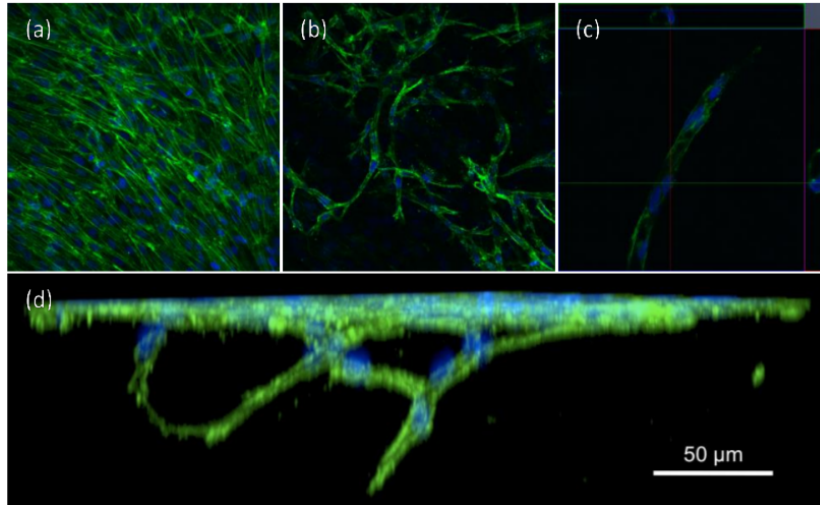


Figure 4.4: (a) TIME endothelial cells cultured on 2mg/ml collagen gel. (b) By day 7, significant angiogenic sprouting was observed beneath the surface. (c) Lumen formation was present without a bFGF growth factor supplement. (d) Z-stack confocal imaging reveals the vascular complexity that can be achieved when 10 ng/ml bFGF is added resulting in separate sprouts anastomosing and continuing to extend far into the tumors.

4.1.3 Hypoxia Measurement

By altering the number of cells seeded in the gel or properties of the gel (thickness, collagen concentration, porosity) hypoxia can be induced. Hypoxia is visualized by performing antibody staining for HIF-1a (Figures 4.5a and 4.5b) and performing real time PCR to determine the gene expression levels of HIF-1a (Figure 4.6) [131, 132]. With real time PCR, measured angiogenic gene expression (VEG-F, Ang-1, Ang-2) for a wide array of genes and under many platform conditions has been measured (not shown) [22, 23].

4.2 Single Channel Vascularized Platform

The laboratory contains a single channel microfluidic platform to determine the influence of flow on tumor progression. This platform is fabricated from type I collagen derived from excised rat tail tendon. The channel is fabricated by neutralizing collagen solution mixed with cancer cells into fluorinated ethylene propylene (FEP) tubing fitted concentrically with a stainless steel needle and capped with PDMS sleeves [21, 22, 23]. The FEP enclosure and a water bath are used to enable refractive matching allowing undistorted imaging in the center of the (transparent) hydrogel. Following polymerization of collagen with hydrochloric acid, the needle is removed, leaving a cylindri-

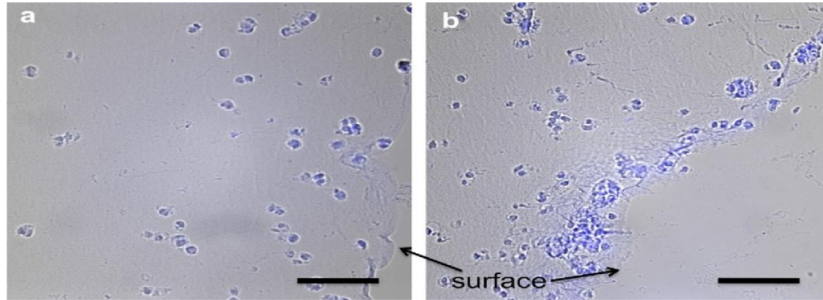


Figure 4.5: Hypoxia was detected using immunofluorescence for HIF-1a. (a) MDA-MB-231 cells were seeded at a density of 4 million cells/ml, and on day 1, the blue fluorescence indicated intra-cellular levels of hypoxia. (b) On day 5, the fluorescence intensity increased, in particular within the large cell clusters, signifying an increase in hypoxic oxygen levels. Scale bar is 100 μm .

cal microchannel embedded within the hydrogel which is subsequently seeded with endothelial cells (Figure 4.7B). Flow is introduced into the microfluidic channel generating target wall shear stresses ($0.01\text{-}10\text{ dynes/cm}^2$). Shear stresses and spatiotemporal velocity profiles in the vessel can be measured with micro-particle image velocimetry ($\mu\text{-PIV}$) [21, 22, 23]. In a microPIV measurement, fluorescent polystyrene tracer particles seeded in the flow are illuminated and imaged by a high-speed camera. Cross-correlation of image pairs are used to calculate statistical particle displacement, which, with the known image frequency, is used to compute the velocity field. This system demonstrates the capability for fabricating a 3D microfluidic collagen platform capable of sustaining cell proliferation [22], and has been used to study tumor and endothelial intercellular signaling in response to hemodynamic flow [23].

4.2.1 Matrix Composition

The influence of matrix composition (collagen types I, II, and IV) and collagen concentration on diffusivity and stiffness of the hydrogel, which ultimately affects cell-matrix interactions, including matrix remodeling and ultimately tumor development can also be assessed [8, 9]. Collagen types I, II, and IV can be isolated from rat tail tendons, articular cartilage, and livers/kidneys, respectively. Collagen concentrations of $2\text{-}8\text{ mg/ml}$ can be used to yield elastic moduli (as measured with dynamic mechanical analysis) representative of many tumors [9] with particular focus on matching that of breast and brain tumors. Material properties including stiffness, fiber structure, and porosity can be measured for varying matrix compositions

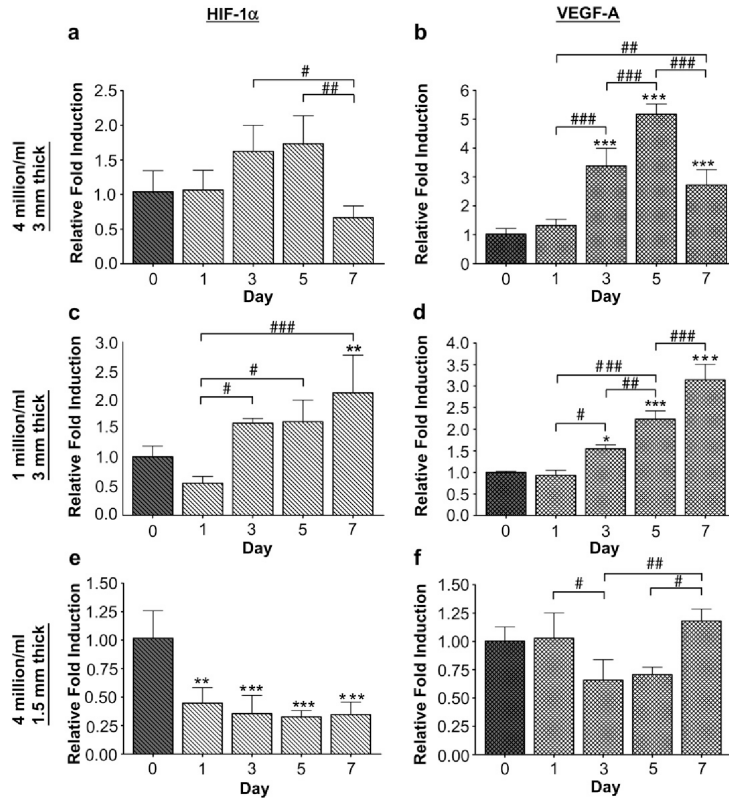


Figure 4.6: Quantitative RT-PCR was used to analyze the progression of HIF-1a expression in the tumor platforms over a 7-day period, with expression on day 0 used as the control. (a) MDA-MB-231 cells were seeded at a density of 4 million cells/ml in 3 mm thick hydrogels. HIF-1a was upregulated on day 3 and day 5 (c) When the initial cell seeding density was decreased to 1 million cells/ml, HIF-1a was significantly upregulated on day 7, (e.) When the cell seeding density was kept at 4 million cells/ml but a 1.5 mm thick hydrogel was used, HIF-1a was not upregulated over the 7-day period. * was used to indicate significance compared to day 0.*/#, **/##, and***/### denote $p < 0.05$, 0.01, and 0.001, respectively.

to verify the proposed platform mimics native tumors. The steady-state elastic modulus, E , measured as by confined uniaxial compression using a mechanical load frame (Bose ElectroForce) equipped with a precision load cell [9]. Each sample will be linearly displaced at a low speed to measure the quasi-steady state elastic modulus (Figure 4.8b). ECM structure (fibril density, size, orientation and hydrogel porosity), which is coupled with stiffness, is also relevant. Collagen fibrils are imaged using laser scanning confocal reflectance microscopy (CRM) with a 40x water immersion lens, which, in

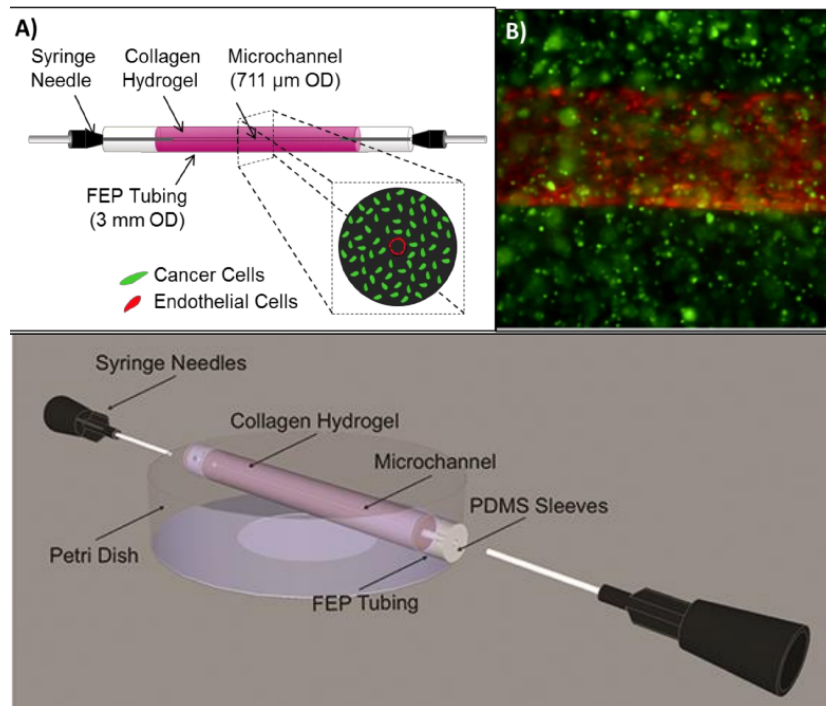


Figure 4.7: Single channel platform A) cancer cells (green) and endothelial cells (red). B) Co-culture of both cells in platform; scale=200 μm , Bottom) Embodiment of microfluidic device.

contrast to scanning electron microscopy, affords high-resolution images of collagen fibers while maintaining the hydrated structure. A Frangi Vesselness filter can be utilized to enhance fiber imaging for quantitative analysis of fiber structure metrics, including fiber diameter, length, volume fraction, orientation, and pore size. Figure 4.8 shows CRM images (a), compressive modulus at strain rate of 0.1%/s (b), fiber diameter (c), and pore diameter (d) as a function of collagen concentration, temperature, and pH [9].

4.2.2 Cellular Composition

Any type of tumor cell can be incorporated in the single channel platform. For all applications, a transformed human microvascular endothelial cell line, (TIME) will form the endothelialized microchannel. A human glioblastoma brain cancer cell line, U-87 MG, or breast cancer cell lines of varying aggressiveness (MCF-7, MDA-MB- 231 or 361) can be incorporated into the platform, in separate experiments to mimic the brain and breast tumor microenvironments respectively. Tumor cells (1×10^6 to 10×10^6 cells/ml) can

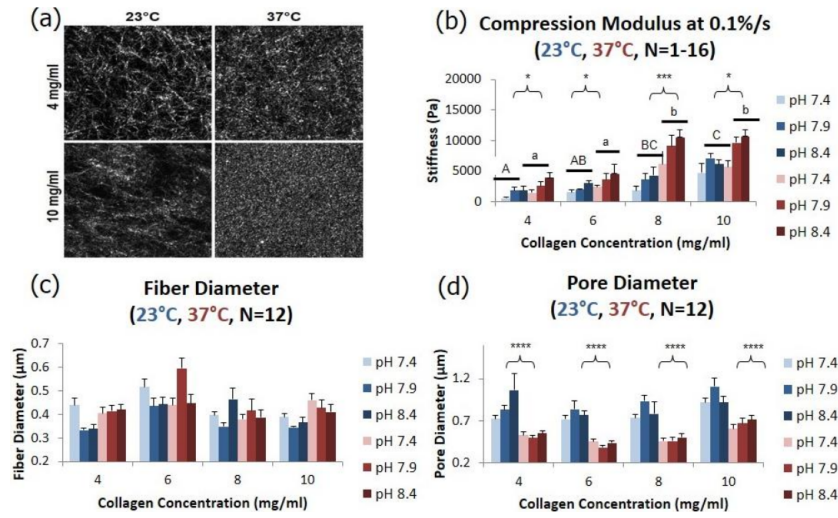


Figure 4.8: (a) CRM images for 4 mg/ml and 10 mg/ml hydrogel polymerized at 23°C and 37°C with pH 7.4 and (b) compressive modulus, (c) fiber diameter, and (d) pore diameter determined as a function of collagen concentration, polymerization temperature, and pH for collagen hydrogels.

be uniformly suspended in neutralized collagen solutions during polymerization. TIME cells can then be injected into the microchannel at a density of (10×10^6 cells/ml), a quantity sufficient to allow growth of a confluent lumen [22, 23]. To better mimic these native tumors and create matrices that are stromal cell initiated, fibroblasts of varying concentration can be introduced in the tumor matrix. Previous work has shown sufficient tumor-fibroblast proliferation and limited matrix contraction with ratios of 2:1:2 of endothelial:fibroblast:tumor cells.

4.2.3 Hemodynamics

Average shear stress in normal vessels is 4 dynes/cm²[132]. Inhibition of cancer cell growth and differentiation can occur after exposure to high shear stress of 12 dynes/cm² [132]. Flow can be introduced in the microfluidic channel with a syringe pump generating wall shear stresses of 1-15 dynes/cm². The effect of shear stress and associated velocity profiles on tumor growth and cancer cell metastasis can be determined. Flow rates and shear stress can be quantified with microparticle image velocimetry (μ -PIV) using published methods [22, 23]. Briefly, 1 μ m fluorescent microparticles, suspended in cell media, plasma, and heparinized whole blood will be injected in the channel at flow rates of 20 μ l/min-2 ml/min [132]. Channels will be illuminated with a 532 nm laser and microparticles will be imaged with a 20x microscope ob-

jective at 125 frames/second with a field of view of 1024x512 pixels. Velocity fields will be determined by ensemble robust phase correlation and processing with mean subtraction and high-pass Gaussian filters.

4.2.4 Endothelial Permeability

The number of cancer cells and magnitude of wall shear stress can be varied to cause cell-mediated and hemodynamic changes in permeability. To replicate the tumor vasculature, which is permeable and tortuous, and investigate the influence of vessel properties on tumor growth, varying red blood cells can be introduced. Vessel permeability are measured as follows: briefly, 70 kDa Oregon green-conjugated dextran is perfused into the channel and the width of the collagen (including the channel) imaged. The average fluorescence intensity over time can be used to find the effective permeability coefficient or the ability of the solute to escape uniformly from the lumen. The single-channel collagen microfluidic device has been employed to study signaling between breast cancer cells within the collagen gel (MDA-MB-231) and a complete endothelium on the lumen of the channel (TIME cells) in response to fluid shear and demonstrated the role of shear stress on angiogenic gene expression and endothelial permeability [22, 23] (Figure 4.9). From the quantitative data, it can be concluded that high wall shear stress down-regulates tumor-expressed angiogenic factors, and increases permeability of the endothelium in the MDA-MB-231 and TIME co-culture compared to monocultures [22, 23].

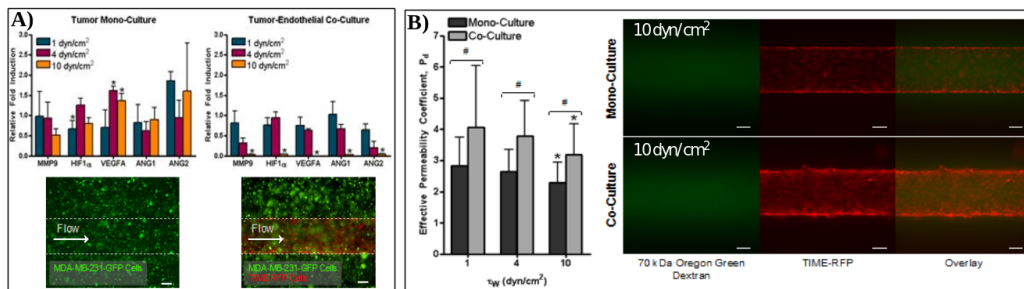


Figure 4.9: Tumor endothelial co-culture in preliminary A) Influence of shear stress on metastatic and angiogenic gene expression of MDA-MB-231 cells alone (green) and co-culture of MDA-MB-231 and TIME (red) cells; scale bar 200 μ m B) Influence of shear stress on permeability of endothelium (TIME cells) alone or co-cultured with MDA-MB-231 cells; scale bar 200 μ m

4.3 Dual Channel Vascularized Platform

Although the single channel platform enables the influence of hemodynamics, matrix properties, and endothelial permeability on tumor development to be studied, aggressive cancers (breast, brain and pancreas) require a more sophisticated system to fully mimic the complex and evolving pathological state driven by microenvironmental gradients which regulate tumor progression and limit therapy success. It is proposed that a dual channel system, shown in Figure 4.10, be developed that will enable microenvironmental factors such as pressure and matrix stiffness gradients to be independently and simultaneously applied. NPs, cancer drugs, immune cells, or physiological solutions (e.g. blood, plasma, patient-specific tumor cells) can be added to the channel to study multicellular response to different stimuli. This platform has great potential for modeling astrocytic brain tumors (glioblastoma multiforme (GBM)), exocrine pancreatic cancer, and breast cancer. Both GBM and pancreatic cancer are highly aggressive, invasive tumors which pervasively infiltrate healthy surrounding tissue and are not treatable with total resection, chemotherapy, and radiation. Breast and brain tumors are highly vascularized, which increases fluid pressure gradients across the interstitium. While pancreatic tumors also undergo desmoplasia and tissue stiffening, these tumors are hypovascular, with 80% lower microvessel density compared to normal pancreatic tissue [9]. Decreased vascularization alters pressure gradients, yet how these factors influence NP transport is unknown. Gradient trends for breast (i.e. \uparrow stiffness and \uparrow pressure) or pancreatic cancer (\uparrow stiffness and \downarrow pressure) will reflect native tumors. Figure 4.11 shows the embodiment of the dual channel microfluidic system in which two endothelialized channels (red) are on either side of a collagen platform containing tumor cells (green).

It is noticed that additional complex mechanical influences on tumor behavior can be reproduced in the laboratory set up described. These include characterizations and measurements of stiffness gradients by controlling concentrations, pH, and polymerizations pH and pressure gradients due to leaky tumor and poor lymphatic drainage, in which interstitial fluid pressure are elevated *in vivo*. An experimental configuration for hydrogels of different stiffness introduced in different channels is shown in Figure 4.12. A pressure gradient of 1 mmHg/mm can be achieved in a hydrogel by adjusting the relative flow rate in each perfusion channel (Q_1 and Q_2 in Figure 4.12).

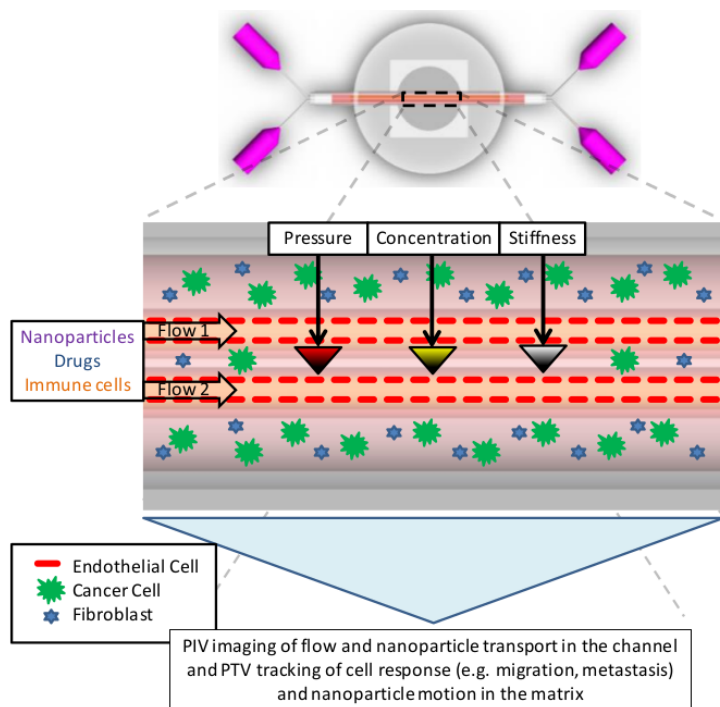


Figure 4.10: Schematic for a dual channel system. Microenvironmental gradients for matrix stiffness and pressure can be employed individually or simultaneously between channels fabricated in collagen. Multiple cell types such as fibroblasts and tumor cells can be seeded in the matrix, while microchannels can be seeded with endothelial cells and perfused with immune cells or platelets.

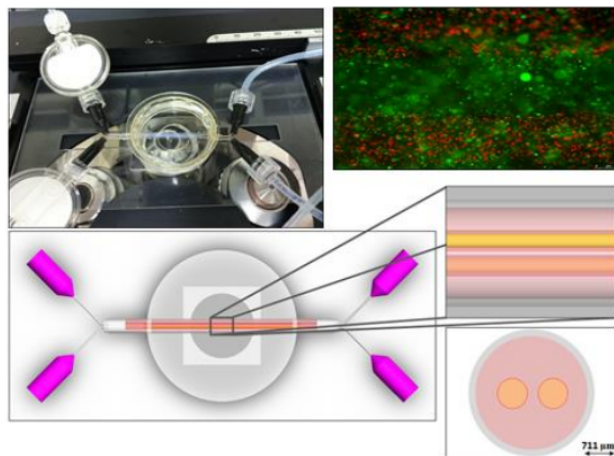


Figure 4.11: First generation-multichannel microfluidic device showing culture of endothelial cells (red) and cancer cells (green) dual flows using multiple syringe pumps.

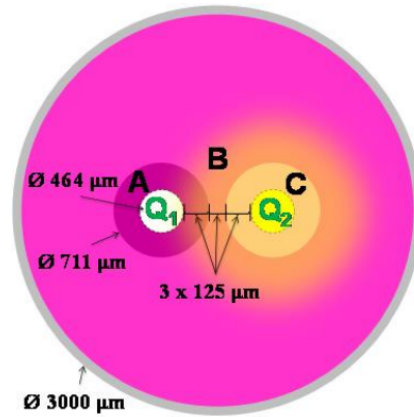


Figure 4.12: Configuration indicating stiffness gradient (pink, A-C), concentration gradient (yellow), pressure gradient obtained via flow rate (green, Q1 and Q2), and FEP constraining tubing (gray).

4.4 Surrogate Models of Branching Vascular Networks

To investigate the influence of physiologically representative branching and tortuosity of vessels found in tumors and associated flow patterns on tumor growth, a new microfluidic platform is being created. The approach to creating the branching network platform will utilize lithography techniques common to microfluidics in combination with sacrificial material methods implemented in tissue engineering. A collagen hydrogel seeded with cancer cells will be used to represent the tumor tissue and to encapsulate the designed vascular microfluidic network. This engineered platform can be used for studies involving the transport of materials through the hydrogel, the influence of cell-cell and cell-matrix interactions, and the evaluation of fluid flow patterns that supersedes two-dimensional models and can be tuned to investigate different tumor microenvironments. Figure 4.13 presents a CAD rendering of the type of engineered tumor platform that can be fabricated and used for *in vitro* studies.

Lithographic processing can be used to produce patterns representative of a vascular network found in tumors and subsequently that pattern may be utilized to produce microfluidic channels on the same scale as the blood vessels in a tumor. This is completed by producing a PDMS stamp from the lithographic pattern and then flowing gelatin into the resulting channel of the PDMS stamp. The gelatin is to be used as a sacrificial material, and once the gelatin has set it can be removed from the stamp and encased in a collagen hydrogel. By melting and flushing the gelatin from the hydrogel a network of microfluidic channels can be created in the hydrogel. This process creates

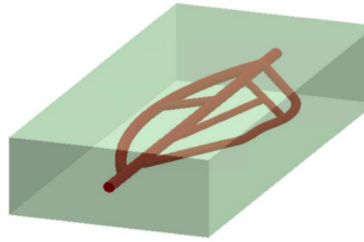


Figure 4.13: Engineered microfluidic channels lined with endothelial cells in a collagen matrix hosting cancer cells representative of a vascular network in a tumor.

channels that have a rectangular cross-section; however, once the channels have been seeded with an endothelial lining the resulting cross-section will be circular. The tumor model presented in Figure 4.13 can be fabricated and housed in a platform as presented in Figure 4.14. This platform consists of a PDMS well passively adhered to a glass microscope slide that can hold the designed tumor model. Once a PDMS lid is placed over the well materials can be passed through the platform with the use of coupling pins and tubing that attaches to a syringe. This platform will meet the experimentation and imaging needs of the group as more complex tumor environments are studied.

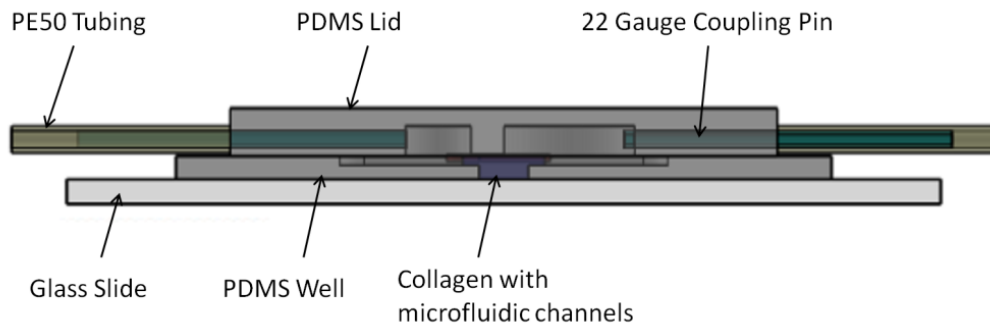


Figure 4.14: Platform for use in fabrication of and experimentation of an engineered tumor model.

5 Image Processing: Data Collection for the Validation Scenario, S_V

In this chapter, clinically practical image processing technologies are described that can be used to acquire data on the progression of tumor growth as viewed in longitudinal human clinical studies. These technologies, algorithms, and computing paradigms may provide a fundamentally new way for non-invasive model validation. This form of data collection on the ‘patient scale’ may be viewed as the validation scenario, S_V , within our notation and framework in Chapter 3. We argue that the heuristic statistical models routinely used in medical imaging studies to describe this ‘big data’ *complements* our first principle physics based approach and provides perspective on the canonical design decisions of accuracy versus efficiency.

Motivations of our tumor growth modeling efforts are rooted in the fundamental conservation equations of mass, momentum, energy, and entropy that all physical systems must obey. Being a physical phenomena, the evolution of tumor growth is no exception. Reliable computer representations for predicting the extremely complex cancer growth phenomena may be built from methodological model selection that is calibrated to representative experimental scenarios, S_C . However, the typical approach within routine medical imaging studies *strongly differs* from this approach. Prediction from first principles is viewed as a ‘daunting’ task with too many unknowns, complexity, and uncertainty. Heuristic statistical models are commonly chosen that best describe the data available. An Occam’s razor methodology is typically adopted in that simplicity is preferred and relatively few model input variables are considered for a specific output; the developed model is highly specialized for the task at hand.

For example, suppose that a multi-scale model is developed for predicting clinical quantities of interest on a macroscale; *what are sufficient conditions to calibrate this model in-vitro and to have confidence in applying this model to guide patient decisions ?*

- The model would incorporate each distinct cellular-scale signal pathway identified in the cancer hallmarks and strongly couple this to multispecies continuum mixture theory.
 - A sensitivity analysis of each cellular pathway needs to quantitatively demonstrate the importance of bridging the scales for including the influence of the cellular pathways on with respect to the macroscale QoI prediction.

- The clinically relevant quantity of interest must be clearly defined and is dependent on tumor type, anatomical location, and treatment history.

$$\text{QoI}(T, A, H)$$

$$T \in \{\text{glioma, hepatocellular carcinoma, melanoma, ...}\}$$

$$A \in \{\text{liver, brain, bone, ...}\}$$

$$H \in \{\text{chemotherapy, surgical resection, radiation, ...}\}$$

- A model of this sophistication would have at a bare minimum $\mathcal{O}(50)$ submodels and $\mathcal{O}(100)$ parameters (2 parameters per model). Given this number of parameters, overfitting is a significant concern and an equal number of data points would be needed to calibrate the model to guard against overfitting.
 - Calibration data would need to be provided on both the cellular and continuum scale of a *single* calibration scenario, \mathcal{S}_C , to validate the multiscale coupling.
 - At a minimum, one calibration scenario, \mathcal{S}_C , and one calibration dataset, \mathcal{D}_C would be needed per parameter. The scenario and dataset would need to be considered within the context of the particular clinical QoI.

$$(\mathcal{S}_C, \mathcal{D}_C)_{i,j} \quad i = 1, \dots, N_{\text{parameters}} \quad j = 1, \dots, N_{\text{QoI}}$$

- A **second** independent dataset is needed to evaluate the prediction accuracy for model selection.
- In the validation and prediction scenarios, assumptions of each sub-model would need to be verified to ensure applicability.
- For a particular clinical quantity of interest, QoI, a **third** independent dataset is needed in which the model has demonstrated in at least 95 out of 100 patients to accurately predict the clinical quantity of interest.
- Given the computer prediction of the QoI, the final clinical decision would be assessed within the context of game theory; the risk of false predictions would be factored into the decision.

With this in mind, the sheer combinatorics of the pathways in which a cancer may progress over multiple scales is seen to be simply too large to acquire the experimental data needed to confidently calibrate and validate each clinically relevant treatment scenario for each tumor type, anatomical

location and treatment history. Significant time and resource investment are needed to acquire all calibration data needed for *single* clinical QoI for a single tumor type, anatomical location, and treatment history. In fact, one may argue that the investment in the data acquisition for a particular set of relevant calibration scenarios *defines* the model and is worthy of consideration within the abstract form.

$$A(\theta, \mathcal{S}, \mathcal{D}) = 0 \quad \theta \in \Theta \quad \mathcal{S} \in \{\mathcal{S}_C, \mathcal{S}_V, \mathcal{S}_P, \} \quad \mathcal{D} \in \{\mathcal{D}_C, \mathcal{D}_M, \mathcal{D}_V, \mathcal{S}_P, \}$$

Given limited resources, missing data is an *unavoidable fact* that manifests within our approach as modeling uncertainties. Common statistical models of tumor growth go one step further and argue that the assumptions of physics based models are not practically applicable to the patient scenario, \mathcal{S}_P . Hence, heuristic models of the available data are the remaining options. The distinction between the lack of modeling detail and missing data is lost and considered jointly as ‘model uncertainty’. This chapter focuses on the image processing based data collection used as input to these heuristic models.

5.1 Image Processing Measurements

Data curating from both high-resolution longitudinal imaging (functional and anatomical) as well as gold standard pathology in humans is a necessity to validate model predictions. The clinically relevant data acquisitions facilitate meaningful analysis of the proposed advanced model calibration and validation efforts and provide a baseline for analyzing tumor progression as seen in existing imaging protocols.

5.1.1 Histopathology

Histopathology data provides a the gold standard for the classification of aggressive and indolent disease. Semi-quantitative data is graded on a 5-point scale by a board-certified pathologist. For example, in prostate, the range consists of aggressive (score 1) to indolent (score 5) disease. Intermediate scores (score 2-4) will allow for variations in volume fractions of heterogeneity between predominantly aggressive and indolent. Additional quantitative pathology measures such as mitotic index, Ki-67 index, IDH status, p53 status are also available.

5.1.2 Image Processing

Database Infrastructure: Technology to facilitate repeatable research and reproducible results is essential. Informatics considerations are non triv-

ial. An SQL database of the 1) patient identification data, 2) pulse sequence parameters, 3) raw imaging data for post-processing, 4) metadata (primary tumor location, treatment history, etc) and 5) classification results is typically required. Each data source must be reliably backed up for project safety and longevity. Analytics technology is needed to automate query and data retrieval (patient information and imaging data) from patient imaging databases and existing medical information big data infrastructure, Figure 5.1. Further, the database workflow must incorporate acquisitions from multiple clinically available imaging sequences such as T1W, T2W, Flair, DTI, DWI, DSC, and DCE.

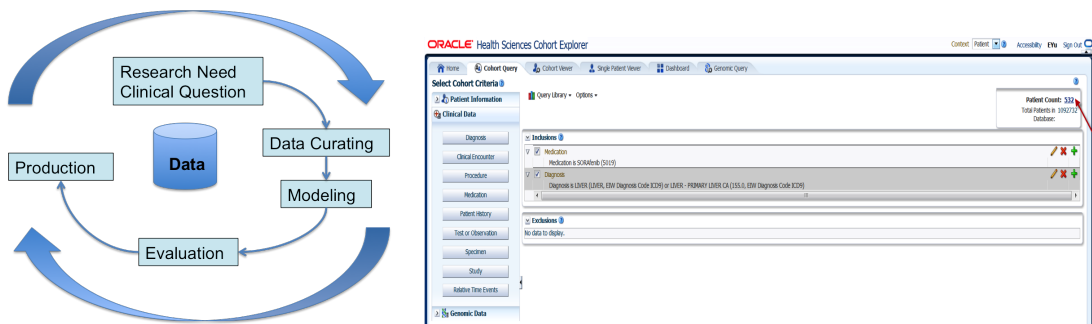


Figure 5.1: MD Anderson has invested significant resources to assist in imaging studies. Current database technology is built from Oracle[®] commercial infrastructure to ingest information from multiple sources throughout the institution including: pharmacy, radiology, surgery, and genomic medicine. PHI is anonymized. Query of the existing technology uses standardized codes for diagnosis, surgical procedures, medications, and patient history. The infrastructure interfaces with various commercial software including, but are not limited, to Montage, Epic, PACS, Power Scribe, Isite. Multiple relevant clinical trials are currently ongoing (NCT01861405, NCT01212237, NCT00392327, NCT00085735, NCT00336024). These cases are also ingested into to the database at regular intervals.

Data Post Processing: Multiple commercial and open source packages are available for processing the raw data from the DTI, DSC, and DCE pulse sequences. Commercial packages include: (1) NordicICE, version 2.3.14 (NordicNeuroLab AS, Norway), (2) Olea Sphere[®], version 2.3 (Olea Medical SA, France), and (3) the General Electric (GE) Advantage Workstation (AW), version 4.5 (GE Healthcare Technology, Waukesha, WI). Open Source packages include: (1) OsiriX DCE tool and (2) 3D Slicer modules. Multiple

pharmacokinetic models and diffusion models will be considered in optimizing the classification accuracy.

Image Processing: Image segmentation and registration, are fundamental image processing tasks for image guided therapy assessment in a variety of anatomical sites. An example data processing pipeline is presented for brain tumors (Figure 5.2). Brain tumor segmentation is particularly challenging and has been the subject of ongoing crowd sourcing challenges, BRATS MIC-CAI [89]. Incorporating spatial heterogeneities of the 1) grey matter, 2) white matter, 3) cerebrospinal fluid, 4) edema, 5) and tumor tissue are essential in creating realistic classification predictions. Deformable image registration methods [12], are needed to evaluate the structural response associated with disease progression as well as fuse anatomical with functional imaging (DTI, DWI, perfusion imaging). Mutual information distance measures are needed for multi-modality information. Random forest based tumor segmentation [140] are machine learning methods, Figure 5.3, that have gained popularity in delineating and measuring changes within particular anatomical features. Random forest predictors include multi-modality finite mixture model segmentation to detect distinct tissue types. Further details of the image registration and random forest segmentation are discussed in detail in Sections 5.2 and 5.3

5.2 Image Registration

Modern image registration methods have been significantly influenced by the mathematical formalism of large deformation diffeomorphisms [16, 33, 46]. The diffeomorphic formalism provides a rigorous framework for finding a deformation field that satisfies the physics of an elastic or fluid deformation and guarantees sufficient smoothness expected of biological deformations. Diffeomorphic registration techniques rely on defining a differentiable, bijective mapping between the fixed and moving image and guarantee that the inverse displacement fields and Jacobian based volume measurements will be well-defined. The regularity on the solution imposed within the diffeomorphic framework preserves the topology of the anatomy and prevents deformation in an uncontrolled manner which would otherwise make results difficult to interpret.

5.2.1 Diffeomorphic Registration

The motion, $\varphi(\mathbf{X}, t) : \Omega_0 \times \mathbb{R} \rightarrow \Omega_t$, maps the reference domain, Ω_0 , to the current configuration, Ω_t . We will assume that the motion is bijective

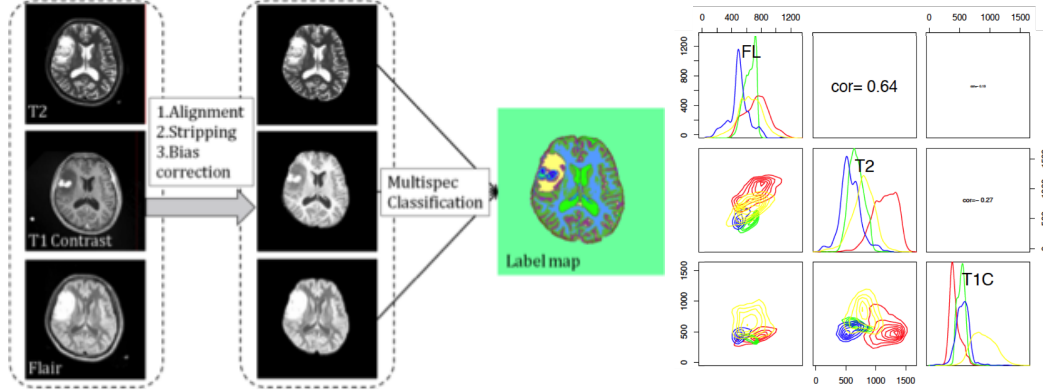


Figure 5.2: Multi-modality tumor segmentation. Representative image features of a tumor under T2, Flair, and T1 with contrast (T1C) are shown. Probability distribution of intensity for each image feature in the ground truth segmentation are in general non-Gaussian. The classification pipeline consists of: (1) Collecting dataset and transforming DICOM to analyze the volume; (2) Image Registration; (3) Brain striping; (4) Bias correction; (5) classification of multi-modality image data using random forest/mixture models; and (6) Finding connected components, relabeling, region merging.

and sufficiently smooth such that the inverse of the motion is well defined, $\varphi^{-1}(\mathbf{y}, t) : \Omega_t \times \mathbb{R} \rightarrow \Omega_0$.

The velocity of the material points is understood as the partial time derivative of the motion.

$$\dot{\mathbf{y}} = \frac{\partial \varphi}{\partial t}(\mathbf{X}, t)$$

The velocity $\mathbf{v}(\mathbf{y}, t)$ with respect to a spatial coordinate reference, $\mathbf{y} = \varphi(\mathbf{X}, t)$, may be understood as follows: For \mathbf{y} at a given t , $\varphi^{-1}(\mathbf{y}, t)$ will give you the material point, \mathbf{X} then $\frac{\partial \varphi}{\partial t}$ can be used to compute a velocity associated with the material point, \mathbf{X}

$$\mathbf{v}(\mathbf{y}, t) = \frac{\partial \varphi}{\partial t}(\varphi^{-1}(\mathbf{y}, t), t) \quad \text{or} \quad \mathbf{v} \circ \varphi(\mathbf{X}, t) = \frac{\partial \varphi}{\partial t}(\mathbf{X}, t)$$

Consider an image defined on the reference and current configuration

$$I_0 : \Omega_0 \rightarrow \mathbb{R} \quad I_t : \Omega_t \rightarrow \mathbb{R}$$

One possible metric to compare these images is defined by mapping the image defined on the reference domain to the current configuration

$$I_0(\varphi^{-1}(\mathbf{y}, t)) \equiv I_0 \circ \varphi^{-1}(\mathbf{y}, t) \quad \varphi^{-1} : \Omega_t \times \mathbb{R} \rightarrow \Omega_0 \quad I_0 \circ \varphi^{-1} : \Omega_t \times \mathbb{R} \rightarrow \mathbb{R}$$

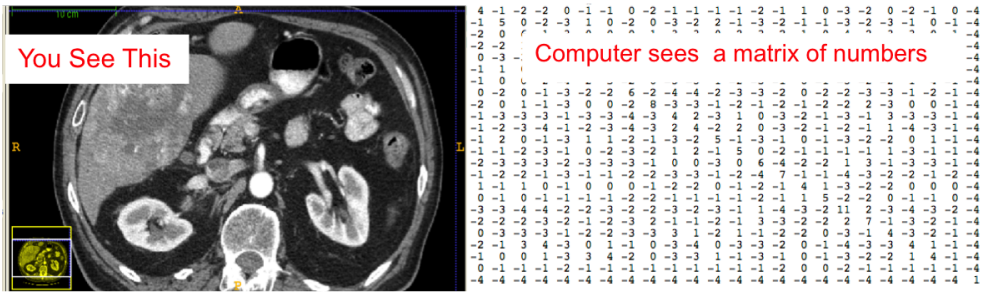


Figure 5.3: Machine Learning. In general, the problem of tissue classification (synonymous with image contouring and segmentation) is treated as a machine learning problem. As opposed to a conventional 1st principle physics based modeling paradigm in which the computer must be programmed to do something new with meticulous detail and line-by-line instruction, machine learning is a field of study that gives computers the ability to learn without being explicitly programmed. Machine learning is a supervised statistical learning technique that is beneficial when assumptions of alternative physics-models of complex phenomena do not provide the needed accuracy or are computationally prohibitive. While the human eye sees the inherent structure of a medical image, the machine merely sees an array of numbers. It is not possible to write an analytical expression within a single monolithic complex algorithm to identify the tissue structures. However, machine learning provides a mechanism train an algorithm to perform the complex task of tissue identification by assembling a group of relatively trivial tasks. Similar to the human cognitive process, the algorithm builds intuition by repetitively training the underlying mean and covariance functions that define a statistic model to match representative datasets.

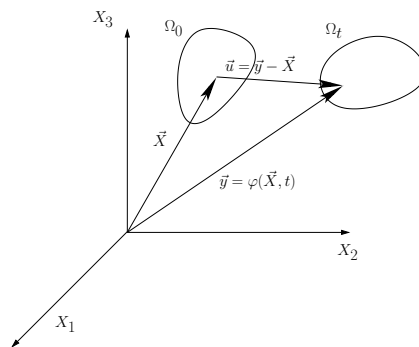


Figure 5.4: The motion φ tracks the motion of a particle \mathbf{X} over time.

The integration of the L_2 difference may be performed as a distance measure between the two images in the current configuration Ω_t .

$$\|I_0 \circ \varphi^{-1} - I_t\|_{L_2}^2 = \int_{\Omega_t} (I_0 \circ \varphi^{-1}(\mathbf{y}, t) - I_t(\mathbf{y}))^2 dy$$

Diffeomorphic Registration attempts to minimize the image misfit along with a penalty for the rate of change of the deformation.

$$\min_{\mathbf{v}} E(\mathbf{v}) \quad E(\mathbf{v}) = \left(\underbrace{\frac{1}{2} \int_0^t \|L\mathbf{v}(\cdot, \tau)\|_{L_2}^2 d\tau}_{\text{rate of change}} + \underbrace{\Pi(I_0 \circ \varphi^{-1}(\cdot, t), I_t)}_{\text{image misfit}} \right)$$

The space of diffeomorphic transformations on $\text{diff}(\Omega_0)$ is defined as the set of all transformations such that the inverse exists is continuous and differentiable.

$$\text{diff}(\Omega_0) \equiv \{\varphi : \varphi^{-1} \text{ exists and } \varphi^{-1} \in C^1\}$$

Typical operators for L are understood as approximations to the conservation laws of fluid flow

$$L = \begin{cases} -\alpha\Delta + \beta & \text{Regularized Stokes Flow} \\ -\mu\Delta + (\lambda + \mu)\nabla(\nabla\cdot) & \text{Low Reynolds, Compressible Flow} \end{cases}$$

5.3 Random Forest [37, 91]

Problem Statement: Given a labeled set of training data, learn a general mapping which associates previously unseen test data with their corresponding classes.

Tree Testing: A decision tree, Figure 5.5, is a series of tests that are organized in a hierarchical fashion. It is a data structure made of a collection of nodes that are divided into internal (or split) nodes and terminal (or leaf) nodes. All nodes (except the root) have exactly one incoming edge. A test is defined as ‘yes’/‘no’, ‘left’/‘right’, ‘0’/‘1’ through a series of so-called test functions, $h(v, \theta) : \mathbb{R}^d \times \tau \rightarrow \{0, 1\}$. During testing, we would like to compute the probability of a class label $c \in \mathcal{C} \equiv \{c_1, c_2, c_3, \dots, c_N\}$ given an input test data $v \in \mathbb{R}^d$. This conditional probability is denoted $p(c|v)$ and is obtained by optimizing an energy over a training set \mathcal{S}_0 of data and associated ground truth labels. Given a set of ‘trained’ parameters that are learned from the data, $\theta \in \tau$, test functions map feature space \mathbb{R}^d to binary

‘left’/‘right’ decisions. Given a set of feature points, \mathcal{S}_j , at the j -th decision node, the left and right sets are uniquely determined as

$$\mathcal{S}_j^L = \{v \in \mathcal{S}_j | h(v, \theta) = 0\} \quad \mathcal{S}_j^R = \{v \in \mathcal{S}_j | h(v, \theta) = 1\}$$

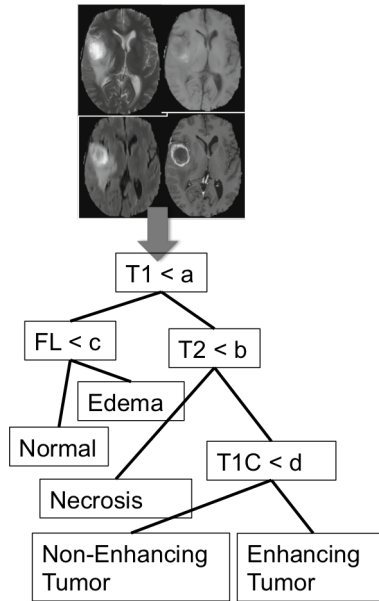


Figure 5.5: Decision Tree. A simplified version of a decision tree is shown for classifying tissue types given multi-parametric MR imaging in brain. Intuitively, the random forest may be understood as a collection of binary decision trees [37, 91].

Tree Training or Learning Tree training or learning is equivalent to model calibration. A popular choice of the objective function that defines the calibration function is the so-called “information gain”, I , when selecting model parameters θ .

$$I = H(S) - \sum_{i \in \{L, R\}} \frac{|\mathcal{S}^i|}{|\mathcal{S}|} H(S^i) \quad H(S) = - \sum_{c \in \mathcal{C}} p(c) \log(p(c))$$

The information gain is defined in terms of the entropy of the system, $H(S)$. Classically, entropy may be understood as proportional to the randomness of a system. The greater the spread of information in a set of classifiers, the greater the entropy. The entropy, $H(S)$, mathematically quantifies this idea. Parameters, $\hat{\theta}$ that optimize the information gain ‘calibrate’ the random forest model.

6 Numerical Algorithms and Parallel Computing

Developing numerical approximations of the various models described earlier and implementing the computational models on parallel computers is a daunting challenge to tumor growth modeling. Among issues that are encountered in such numerical implementations are the following:

- The development of effective numerical solvers for large coupled systems of nonlinear stochastic partial differential equations is a formidable undertaking standing at the forefront of computational science and mathematics. Techniques employing polynomial chaos or stochastic collocation have been implemented by the TMG group, which involve hybrid methods that couple mixed finite element approximations with special time-marching algorithms, and these with expansions in the random-variable spaces [55, 75, 154]. Recent work on a posteriori error estimates for model stochastic systems [6] has enabled the use of adaptive methods, which control error by mesh adaptivity as well as controlling the location and number of collocation points. Parallel versions of these algorithms are under development.
- The phase-field and Cahn-Hilliard models described in Chapter 2 lead to an unusual class of “stiff” ordinary differential equation in the temporal approximations. There is a growing literature on new algorithms for handling systems of this type. The basic source of difficulty lies in the fact that the associated energy function E (recall (2.9)) is non-convex. A family of algorithms, originally suggested by Eyre [49], partition E into a (non-unique) pair of energies, $E = E_{con} + E_{non-con}$, of a convex component and a non-convex part. Stable explicit schemes, such as forward Euler, can be constructed to handle the evolution of solutions related to $E_{non-con}$ while various implicit schemes are used to approximate E_{con} . Several generalizations of this idea have been suggested and successfully implemented [38, 39, 49, 60, 77, 78].
- Several relevant software packages have been developed at ICES that are in use in various phases of the work. One is LibMesh [73], a general purpose, parallel, adaptive Finite Element library that is extremely flexible and user friendly. It contains extensive element libraries, mesh generation and linear and nonlinear solver. Ready access to other general packages exist and are used regularly, including PETSc [13], Cubit and others.

- Implementation of Bayesian stochastic calibration and validation methods described in Chapter 3 must rely on efficient parallel sampling algorithms. One naturally-used software package used effectively for such calculation is QUESO [105] a technology developed at ICES. This tool employs multi-level Markov-Chain Monte-Carlo algorithms and versions of the Metropolis-Hastings algorithm [32, 68]. It has also been incorporated into the general-purpose stochastic solver DAKOTA [2]. The development of new parallel sampling methods is also a fundamental goal of current research in data analytics, data mining and classification methodologies.
- A host of computational tools are needed for implementation of the algorithms for solving large systems, often very stiff, of ordinary differential equations encountered in signaling models. Special methods are used in image recognition, segmentation, and in applying classification algorithms such as the Random Forest algorithm (described in Chapter 5).

Taken in full perspective, a substantial component of effort in developing mathematically sound, verified, robust, parallel algorithms and the associated software, all appropriately documented is critical to the success of multi-scale computational models of tumor growth.

Modern advances in modeling the complex phenomena underlying cancer can be made only if access to parallel high-performance computing (HPC) platforms is available. Fortunately, the TMG has immediate access to computers that are among the world's largest HPC systems. These include Stampede, managed by TACC, the Texas Advanced Computer Center.

The Texas Advanced Computing Center, located nine miles north of the main University of Texas campus, supports two critical HPC supercomputing systems that are available to ICES faculty and research staff as well as to the UT Austin research community, the UT System, and researchers supported by the National Science Foundation.

The larger of these two systems (shown in Figure 6.1a)) is called Stampede. This supercomputer is a Dell-Intel Cluster that includes 102,400 compute cores and has a peak performance of approximately 9 petaflops. Stampede placed 7th in the world Top500 supercomputer performance rankings in June of 2014. This system was brought on-line in January 2013 and was funded through National Science Foundation. A second large-scale HPC system maintained by TACC is called Lonestar (see Figure 6.1b)). This supercomputer is also a Dell-Intel Cluster and includes 22,566 compute cores and has a peak performance of approximately 302 teraflops. Lonestar placed 187th in the world Top500 supercomputer performance rankings in June of

2014. This system has been in operation since 2010 and was funded through a consortium including ICES, UT Austin, Texas A&M University, UT System, and the National Science Foundation.



(a) Stampede.

(b) Lonestar.

Figure 6.1: HPC systems maintained by TACC.

ICES and the TMG has direct access to TACC, and to Stampede, via 10-gigabyte connections. In addition, ICES offers seven clusters and employs a staff of seven systems experts to maintain these smaller-to-mid-level parallel nucleus.

7 The Future: Challenges and Opportunities

The work by the ICES Tumor Modeling Group described in this document has moved the field to a threshold at which special opportunities exist in the short term and substantial challenges loom in the more distant future. In short term, the elusive task of calibrating and validating a substantial class of tumor models of phenomena at different scales seems definitely within reach. The extraordinary laboratory facilities described in Chapter 4 is near completion and will provide a unique, first-of-its kind testing platform for detailed calibration scenarios for a variety of cancer lines using several different cellular and tissue models. It will provide a workplace where model developers and experimentalists work together to develop predictive models of tumor growth. In parallel, the extraordinary non-invasive imaging technologies and new classification and sampling algorithms discussed in Chapter 5 can be used to provide a remarkable *in vivo* observation data essential for model validation. These , as noted earlier, represent all of the components needed for predictive medicine, patient-specific diagnosis and ultimately, treatment-expansions of these capabilities to include signaling models, agent-based models of cell behavior, and models of tissue growth, decline, angiogenesis, and other aspects of the behavior of the microenvironment are underway and are likely to be available soon.

Challenges remain in several areas. Paradigms for full multiscale modeling of cancer have been discussed in some detail in Chapter 2, but the development of the full software libraries to implement these strategies has not been completed and will require much additional work. Another area awaiting deeper studies is the effective modeling of bio-chemotherapy, a subject also under study by the authors of this document. One approach, to be discussed more fully in later editions of this work, is to develop diffusion models of drug densities that couple appropriately with tumor-mass perfusion terms to control tumor growth. The development of models for indirect mechanism of drug action, involving modulation of endogenous factors and signaling pathways, can offer potential means to explore new therapeutic interaction with minimum toxicity and drug resistance. Exactly how such models can be validated and implemented within the framework of various models discussed here remains an open question.

A related area is the development of models of drug delivery, such as systems of nanoparticles, which provide bio-mechanical mechanisms that can focus drug concentration at lesions or provide mechanical features that enable treatments such as thermal ablation.

Then there is the challenge of developing accurate and predictive models

of metastases, which can trace reliably the introduction of cancer cells into the vascular system, their motion and ultimate location in the body; their reaction to chemotherapy drugs, and their growth and decline over time. The interplay between a primary tumor and its metastases remains a poorly understood process. Further improvement in prediction metastases may unfold new potential target for treatment strategies.

The cell modeling algorithms described in this exposition, such as the agent-based models of Section 2.4.1, should be extended to include the specific qualities of stem cells, their potential self-renewing and differentiation properties which provides high intra-tumor heterogeneity. This has also serious implications for designing treatment protocols.

The broad collection of topics relevant to modeling behavior of vascular tumor outlined in this preliminary review, survey the current work and research interest of the ICES TMG team and points to areas in which much additional work remains to be done. The team is confident that many of the building blocks for predictive modeling of this incredible complex system are now in place or will soon be accessible, and that the age of predictive medicine is close at hand.

References

1. F. F. Abraham, J. Q. Broughton, N. Bernstein, and E. Kaxiras. Spanning the continuum to quantum length scales in a dynamic simulation of brittle fracture. *EPL (Europhysics Letters)*, 44(6):783, 1998.
2. B. M. Adams, L. E. Bauman, W. J. Bohnhoff, K. R. Dalbey, M. S. Ebeida, J. P. Eddy, M. S. Eldred, P. D. Hough, K. T. Hu, J. D. Jakeman, L. P. Swiler, and D. M. Vigil. Dakota, a multilevel parallel object-oriented framework for design optimization, parameter estimation, uncertainty quantification, and sensitivity analysis: Version 5.4 user’s manual. Technical report, Sandia Technical Report SAND2010-2183, 2009.
3. G. Albano and V. Giorno. A stochastic model in tumor growth. *Journal of Theoretical Biology*, 242(2):329 – 336, 2006.
4. G. Albano, V. Giorno, P. Román-Román, and F. Torres-Ruiz. Inference on a stochastic two-compartment model in tumor growth. *Computational Statistics and Data Analysis*, 56:1723–1736, 2012.
5. B. B. Aldridge, J. M. Burke, D. A. Lauffenburger, and P. K. Sorger. Physicochemical modelling of cell signalling pathways. *Nature Cell Biology*, 8(11):1195, 2006.
6. R. C. Almeida and J. T. Oden. Solution verification, goal-oriented adaptive methods for stochastic advection–diffusion problems. *Computer Methods in Applied Mechanics and Engineering*, 199(37–40):2472 – 2486, 2010.
7. A. R. A. Anderson and M. A. J. Chaplain. Continuous and discrete mathematical models of tumor-induced angiogenesis. *Bulletin of Mathematical Biology*, 60:857–899, 1995.
8. E. Antoine, P. Vlachos, and M. N. Rylander. Review of collagen i hydrogels for bioengineered tissue microenvironments: Characterization of mechanics, structure, and transport. *Tissue Engineering Part B*, 20(6):683–696, 2014.
9. E. Antoine, P. Vlachos, and M. N. Rylander. Tunable collagen i hydrogels for engineered physiological tissue micro-environments. *PLOS*, *Epub ahead of print*, 2015.

10. A. B. Ariffin, P. F. Forde, S. Jahangeer, D. M. Soden, and J. Hinchion. Releasing pressure in tumors: what do we know so far and where do we go from here? a review. *Cancer research*, 74(10):2655–2662, 2014.
11. A. G. Arroyo and M. L. Iruela-Arispe. Extracellular matrix, inflammation, and the angiogenic response. *Cardiovascular Research*, 86:226–235, 2010.
12. B. B. Avants, C. L. Epstein, M. Grossman, and J. C. Gee. Symmetric diffeomorphic image registration with cross-correlation: evaluating automated labeling of elderly and neurodegenerative brain. *Medical image analysis*, 12(1):26–41, 2008.
13. S. Balay, S. Abhyankar, M. F. Adams, J. Brown, P. Brune, K. Buschelman, V. Eijkhout, W. D. Gropp, D. Kaushik, M. G. Knepley, L. C. McInnes, K. Rupp, B. F. Smith, and H. Zhang. PETSc Web page. <http://www.mcs.anl.gov/petsc>, 2014. URL <http://www.mcs.anl.gov/petsc>.
14. A. Bao, W. T. Phillips, B. Goins, H. S. McGuff, X. Zheng, F. R. Woolley, M. Natarajan, C. Santoyo, F. R. Miller, and R. A. Otto. Setup and characterization of a human head and neck squamous cell carcinoma xenograft model in nude rats. *Otolaryngology–Head and Neck Surgery*, 135(6):853–857, 2006.
15. J. L. Beck and K.-V. Yuen. Model selection using response measurements: Bayesian probabilistic approach. *Journal of Engineering Mechanics*, 130(2):192–203, 2004.
16. M. F. Beg, M. I. Miller, A. Trouvé, and L. Younes. Computing large deformation metric mappings via geodesic flows of diffeomorphisms. *International journal of computer vision*, 61(2):139–157, 2005.
17. N. Bellomo, N. K. Li, and P. K. Maini. On the foundations of cancer modelling: selected topics, speculations, and perspectives. *Mathematical Models and Methods in Applied Sciences*, 18(4):593–646, 2008.
18. J. M. Berg, J. L. Tymoczko, and L. Stryer. *Biochemistry*. W. H. Freeman and Company, sixth edition edition, 2006.
19. J. O. Berger. *Statistical Decision Theory and Bayesian Analysis*. Springer Series in Statistics, 1985.

20. S. J. Boukhris. *Mathematical Modeling and Experimental Validation of Cancer Cell Migration in a Three-Dimensional Tumor Matrix*. PhD thesis, The University of Texas at San Antonio, 2014.
21. C. F. Buchanan and M. N. Rylander. Microfluidic culture models to study the hydrodynamics of tumor progression and therapeutic response. *Biotechnology and Bioengineering*, 110(B):2063–2072, 2015.
22. C. F. Buchanan, E. Voigt, C. S. Szot, J. W. Freeman, P. P. Vlachos, and M. N. Rylander. Three-dimensional microfluidic collagen hydrogels for investigating flow-mediated tumor-endothelial signaling and vascular organization. *Tissue Engineering Part C: Methods*, 20(1):64–75, 2013.
23. C. F. Buchanan, S. S. Verbridge, P. P. Vlachos, and M. N. Rylander. Flow shear stress regulates endothelial barrier function and expression of angiogenic factors in a 3d microfluidic tumor vascular model. *Cell Adhesion & Migration*, 8(5):517–524, 2014.
24. H. Byrne and D. Drasdo. Individual-based and continuum models of growing cell populations: a comparison. *Journal of mathematical biology*, 58(4-5):657–687, 2009.
25. D. G. Cacuci. *Sensitivity and Uncertainty Analysis: Theory*, volume 1. CRC Press, 2007.
26. D. Calvetti and E. Somersalo. *Introduction to Bayesian Scientific Computing: Ten Lectures on Subjective Computing*. Springer, 2007.
27. Y. Cao, Y. Jiang, B. Li, and X. Feng. Biomechanical modeling of surface wrinkling of soft tissues with growth-dependent mechanical properties. *Acta Mechanica Solida Sinica*, 25(5):483–492, 2012.
28. C. H. Chang, J. Horton, D. Schoenfeld, O. Salazer, R. Perez-Tamayo, S. Kramer, A. Weinstein, J. S. Nelson, and Y. Tsukada. Comparison of postoperative radiotherapy and combined postoperative radiotherapy and chemotherapy in the multidisciplinary management of malignant gliomas. *Cancer*, 52:997–1007, 1983.
29. M. A. J. Chaplain. Avascular growth, angiogenesis and vascular growth in solid tumours: The mathematical modelling of the stages of tumour development. *Mathematical and Computer Modelling*, 23(6):47–87, 1996.

30. G. Cheng, J. Tse, R. K. Jain, and L. L. Munn. Micro-environmental mechanical stress controls tumor spheroid size and morphology by suppressing proliferation and inducing apoptosis in cancer cells. *PLoS one*, 4(2):e4632, 2009.
31. M. W. Chevalier and H. El-Samad. A master equation and moment approach for biochemical systems with creation-time-dependent bimolecular rate functions. *The Journal of Chemical Physics*, 141:214108, 2014.
32. S. Chib and E. Greenberg. Understanding the metropolis-hastings algorithm. *The American Statistician*, 49(4):327–335, 1995.
33. G. E. Christensen, R. D. Rabbitt, and M. I. Miller. Deformable templates using large deformation kinematics. *Image Processing, IEEE Transactions on*, 5(10):1435–1447, 1996.
34. V. Cimmelli, A. Sellitto, and V. Triani. A generalized coleman–noll procedure for the exploitation of the entropy principle. In *Proceedings of the Royal Society of London A: Mathematical, Physical and Engineering Sciences*, volume 466, pages 911–925. The Royal Society, 2010.
35. B. D. Coleman and W. Noll. The thermodynamics of elastic materials with heat conduction and viscosity. *Archive for Rational Mechanics and Analysis*, 13(1):167–178, 1963.
36. R. T. Cox. Probability, frequency and reasonable expectation. *American Journal of Physics*, 14(1):1–13, 1946.
37. A. Criminisi and J. Shotton. *Decision forests for computer vision and medical image analysis*. Springer, 2013.
38. V. Cristini, X. Li, J. S. Lowengrub, and S. M. Wise. Nonlinear simulation of solid tumor growth using a mixture model: invasion and branching. *Journal of Mathematical Biology*, 58:723 – 763, 2009.
39. V. Cristini and J. Lowengrub. *Multiscale modeling of cancer: an integrated experimental and mathematical modeling approach*. Cambridge University Press, 2010.
40. R. I. Cukier, C. M. Fortuin, K. E. Shuler, A. G. Petschek, and J. H. Schaibly. Study of the sensitivity of coupled reaction systems to uncertainties in rate coefficients. i theory. *The Journal of Chemical Physics*, 59(8):3873–3878, 1973.

41. W. A. Curtin and R. E. Miller. Atomistic/continuum coupling in computational materials science. *Modelling and simulation in materials science and engineering*, 11(3):R33, 2003.
42. G. D’Antonio, P. Macklin, and L. Preziosi. An agent-based model for elasto-plastic mechanical interactions between cells, basement membrane and extracellular matrix. *Mathematical Biosciences and Engineering*, 10(1):75–101, 2013.
43. N. E. Deakin and M. A. J. Chaplain. Mathematical modeling of cancer invasion: the role of membrane-bound matrix metalloproteinases. In K. A. Rejniak and H. Enderling, editors, *Computational Models in Oncology: from Tumor Initiation to Progression to Treatment*. Frontiers Media SA., 2013.
44. T. S. Deisboeck and G. S. Stamatakos. *Multiscale Cancer Modeling*. Chapman & Hall/Crc Mathematical and Computational Biology Series. Taylor & Francis, 2010.
45. R. Demicheli, R. Foroni, A. Ingrosso, G. Pratesi, C. Soranzo, and M. Tortoreto. An exponential-gompertzian description of lovo cell tumor growth from in vivo and in vitro data. *Cancer Research*, 49:6543 – 6546, 1989.
46. P. Dupuis, U. Grenander, and M. I. Miller. Variational problems on flows of diffeomorphisms for image matching. *Quarterly of applied mathematics*, 56(3):587, 1998.
47. C. M. Elliot. The Cahn-Hilliard model for the kinetics of phase separation. In J. F. Rodrigues, editor, *Mathematical models for phase change problems*. Birkhauser, 1989.
48. C. M. Elliott and Z. Songmu. On the cahn-hilliard. *Archive for Rational Mechanics and Analysis*, 96(4):339–357, 1986.
49. D. J. Eyre. Unconditionally gradient stable time marching the Cahn-Hilliard equation. In J. W. Bullard and L.-Q. Chen, editors, *Computational and Mathematical Models of Microstructural Evolution*, volume 529 of *MRS Proceedings*, pages 39–46. Cambridge University Press, November 1998.
50. Y. Feng, S. J. Boukhris, R. Ranjan, and R. A. Valencia. Biological systems: multiscale modeling based on mixture-theory. In S. De,

- W. Hwang, and E. Kuhl, editors, *Multiscale Modeling in Biomechanics and Mechanobiology*. Springer, 2015.
51. P. C. Fife. Models for phase separation and their mathematics. *Electronic Journal of Differential Equations*, 48:1–26, 2000.
 52. H. B. Frieboes, J. S. Lowengrubb, S. Wise, X. Zheng, P. Macklin, E. Bearer, and V. Cristini. Computer simulation of glioma growth and morphology. *Neuroimage*, 37(Suppl 1):S59–S70, 2007.
 53. H. B. Frieboes, F. Jin, Y.-L. Chuang, S. Wise, J. Lowengrub, and V. Cristini. Three-dimensional multispecies nonlinear tumor growth - II: Tumor invasion and angiogenesis. *Journal of Theoretical Biology*, 264(4):1254–1278, 2011.
 54. S. Ganapathy-Kanniappan and J.-F. H. Geschwind. Tumor glycolysis as a target for cancer therapy: progress and prospects. *Molecular Cancer*, 12:152, 2013.
 55. R. G. Ghanem and P. D. Spanos. *Stochastic Finite Elements: a spectral approach, revised Edition*. Dover Publications, Inc., 2003.
 56. E. Gonçalves, J. Bucher, A. Ryll, J. Niklas, K. Mauch, S. Klamt, M. Rochad, and J. Saez-Rodriguez. Bridging the layers: towards integration of signal transduction, regulation and metabolism into mathematical models. *Molecula BioSystems*, 9:1576, 2013.
 57. D. Hanahan and R. A. Weinberg. The hallmarks of cancer. *Cell*, 100: 57–70, 2000.
 58. D. Hanahan and R. Weinberg. Hallmarks of cancer: The next generation. *Cell*, 144(5):646 – 674, 2011.
 59. A. J. Hawkins-Daarud. *Toward a Predictive Model of Tumor Growth*. PhD thesis, The University of Texas at Austin, 2011.
 60. A. Hawkins-Daarud, K. G. van der Zee, and J. Tinsley Oden. Numerical simulation of a thermodynamically consistent four-species tumor growth model. *International Journal for Numerical Methods in Biomedical Engineering*, 28(1):3–24, 2012.
 61. M. Heida, J. Málek, and K. R. Rajagopal. On the development and generalizations of Cahn-Hilliard equations within a thermodynamic framework. *Zeitschrift für angewandte Mathematik und Physik*, 63:145–169, 2012.

62. R. Hesketh. *Introduction to Cancer Biology*. Cambridge University Press, 1 edition, 2013.
63. A. A. Hyun and P. Macklin. Improved patient-specific calibration for agent-based cancer modeling. *Journal of Theoretical Biology*, 317:422–4, 2013.
64. T. L. Jackson, editor. *Modeling tumor vasculature - Molecular, cellular, and tissue level aspects and implications*. Springer, 2012.
65. R. K. Jain. Normalizing tumor microenvironment to treat cancer: bench to bedside to biomarkers. *Journal of Clinical Oncology*, 31(17):2205–2218, 2013.
66. E. T. Jaynes. *Probability Theory: The Logic of Science*. Cambridge University Press, Cambridge, 2003.
67. T. S. Jr. and K. Burrage. Stochastic simulation in systems biology. *Computational and Structural Biotechnology Journal*, 12(20–21):14 – 25, 2014.
68. J. Kaipio and E. Somersalo. *Statistical and Computational Inverse Problems*. Springer, 2005.
69. A. R. Kansal, S. Torquato, G. R. H. IV, E. A. Chiocca, and T. S. Deisboeck. Simulated brain tumor growth dynamics using a three-dimensional cellular automaton. *Journal of Theoretical Biology*, 203(4):367 – 382, 2000.
70. A. Kansal, S. Torquato, G. H. IV, E. Chiocca, and T. Deisboeck. Cellular automaton of idealized brain tumor growth dynamics. *Biosystems*, 55(1–3):119 – 127, 2000.
71. B. N. Kholodenko, J. F. Hancock, and W. Kolch. Physicochemical modelling of cell signalling pathways. *Nature Cell Biology*, 8(11):1195, 2006.
72. T. Kihara, J. Ito, and J. Miyake. Measurement of biomolecular diffusion in extracellular matrix condensed by fibroblasts using fluorescence correlation spectroscopy. *PLOS ONE*, 8(11):e82382, 2013.
73. B. S. Kirk, J. W. Peterson, R. H. Stogner, and G. F. Carey. libMesh: A C++ Library for Parallel Adaptive Mesh Refinement/Coarsening Simulations. *Engineering with Computers*, 22(3–4):237–254, 2006. <http://dx.doi.org/10.1007/s00366-006-0049-3>.

74. M. A. Knowles and P. J. Selby. *Introduction to the Cellular and Molecular Biology of Cancer*. Oxford University Press, fourth edition edition, 2005.
75. O. P. Le Maître and O. M. Knio. *Spectral Methods for Uncertainty Quantification*. Springer, 2010.
76. E. A. B. F. Lima and R. C. Almeida. A comparative study of some fem mixed formulations for the 1d cahn-hilliard equation. In *CILAMCE XXXII*, 2011.
77. E. A. B. F. Lima, J. T. Oden, and R. C. Almeida. A hybrid ten-species phase-field model of tumor growth. *Mathematical Models and Methods in Applied Sciences*, 24(13):2569–2599, 2014.
78. E. A. B. F. Lima, R. C. Almeida, and J. T. Oden. Analysis and numerical solution of stochastic phase-field models of tumor growth. *Numerical Methods for Partial Differential Equations*, 31(2):552–574, 2015.
79. L. A. Liotta, G. M. Saidel, and J. Kleinerman. Stochastic model of metastases formation. *Biometrics*, 32:535–550, 1976.
80. F. Liu, M. J. Bayarri, J. O. Berger, R. Paulo, and J. Sacks. A Bayesian analysis of the thermal challenge problem. *Computer Methods in Applied Mechanics and Engineering*, 197:2457–2466, 2008.
81. W. K. Liu, E. G. Karpov, and H. S. Park. *Nano mechanics and materials: theory, multiscale methods and applications*. Wiley, 2006.
82. C. F. Lo. Stochastic Gompertz model of tumour cell growth. *Journal of Theoretical Biology*, 248:317–321, 2007.
83. J. S. Lowengrub, H. B. Frieboes, F. Jin, Y. Chuang, X. Li, P. Macklin, S. Wise, and V. Cristini. Nonlinear modelling of cancer: bridging the gap between cells and tumours. *Nonlinearity*, 23(1):R1, 2010.
84. P. Macklin, M. E. Edgerton, A. M. Thompson, and V. Cristini. Patient-calibrated agent-based modelling of ductal carcinoma in situ (dcis): From microscopic measurements to macroscopic predictions of clinical progression. *Journal of Theoretical Biology*, 301(0):122 – 140, 2012.
85. P. Macklin, S. Mumenthaler, and J. Lowengrub. Modeling multiscale necrotic and calcified tissue biomechanics in cancer patients: application to ductal carcinoma in situ (DCIS). In A. Gefen, editor, *Multi-*

- scale Computer Modeling in Biomechanics and Biomedical Engineering*, chapter 13. Springer, Berlin, Germany, 2013.
86. D. G. Mallet and L. G. De Pillis. A cellular automata model of tumor-immune system interactions. *Journal of Theoretical Biology*, 239:334–350, 2006.
 87. N. Mantzaris, S. Webb, and H. G. Othmer. Mathematical modeling of tumor-induced angiogenesis. *Journal of Mathematical Biology*, 49:111 – 187, 2004.
 88. E. A. Martin, editor. *A Dictionary of Science*. Oxford University Press, 6 edition, 2010.
 89. B. H. Menze, A. Jakab, S. Bauer, J. Kalpathy-cramer, and Farahani et al. The Multimodal Brain Tumor Image Segmentation Benchmark (BRATS). *IEEE Transactions on Medical Imaging*, pages 1–32, 2014.
 90. F. Milde, M. Bergdorf, and P. Koumoutsakos. A hybrid model for three-dimensional simulations of sprouting angiogenesis. *Biophysical Journal*, 95:3146 – 3160, 2008.
 91. K. P. Murphy. *Machine learning: a probabilistic perspective*. MIT Press, 2012.
 92. A. Najafi1, G. Bidkhori1, J. H. Bozorgmehr, I. Koch, and A. Masoudi-Nejad. Genome scale modeling in systems biology: Algorithms and resources. *Current Genomics*, 15:130–159, 2014.
 93. National Cancer Institute. Dictionary of cancer terms, 2012. URL <http://www.cancer.gov/dictionary>.
 94. L. Naumov, A. Hoekstra, and P. Slood. Cellular automata models of tumour natural shrinkage. *Physica A: Statistical Mechanics and its Applications*, 390(12):2283 – 2290, 2011.
 95. L. Naumov, A. Hoekstra, and P. Slood. The influence of mitoses rate on growth dynamics of a cellularautomata model of tumour growth. *Procedia Computer Science*, 1:971–978, 2012.
 96. A. Niemisto, V. Dunmire, O. Yli-Harja, W. Zhang, and I. Shmulevich. Analysis of angiogenesis using *in vitro* experiments and stochastic growth models. *Physical Review E*, 72, 2005.

97. K. Norton, M. Wininger, G. Bhanot, S. Ganesan, N. Barnard, and T. Shinbrot. A 2d mechanistic model of breast ductal carcinoma in situ (dcis) morphology and progression. *Journal of Theoretical Biology*, 263(4):393 – 406, 2010.
98. J. T. Oden, A. Hawkins, and S. Prudhomme. General diffuse-interface theories and an approach to predictive tumor growth modeling. *Mathematical Models and Methods in Applied Sciences*, 20(3):477–517, 2010.
99. J. T. Oden, E. E. Prudencio, and A. Hawkins-Daarud. Selection and assessment of phenomenological models of tumor growth. *Mathematical Models and Methods in Applied Sciences*, 23(07):1309–1338, 2013.
100. J. Oden, T. Strouboulis, and P. Devloo. Adaptive finite element methods for the analysis of inviscid compressible flow: Part i. fast refinement/unrefinement and moving mesh methods for unstructured meshes. *Computer Methods in Applied Mechanics and Engineering*, 59(3):327–362, 1986.
101. M. J. Piotrowska and S. D. Angus. A quantitative cellular automaton model of in vitro multicellular spheroid tumour growth. *Journal of Theoretical Biology*, 258(2):165 – 178, 2009.
102. L. Preziosi. *Cancer modelling and simulation*. CRC Press, 1 edition, 2003.
103. E. Prudencio and S. H. Cheung. Parallel adaptive multilevel sampling algorithms for the bayesian analysis of mathematical models. *International Journal for Uncertainty Quantification*, 2(3):215–237, 2012.
104. E. E. Prudencio, P. T. Bauman, D. Faghihi, K. Ravi-Chandar, and J. T. Oden. A computational framework for dynamic data-driven material damage control, based on bayesian inference and model selection. *International Journal for Numerical Methods in Engineering*, pages n/a–n/a, 2014. ISSN 1097-0207. doi: 10.1002/nme.4669. URL <http://dx.doi.org/10.1002/nme.4669>.
105. E. E. Prudencio, S. H. Cheung, T. Oliver, and K. Schulz. The Parallel C++ Statistical Library ‘QUESO’: Quantification of Uncertainty for Estimation, Simulation and Optimization. in preparation, 2010.
106. M. Pyrz and J. Baish. Effect of tumor heterogeneity on interstitial pressure and fluid flow. In *ASME 2013 Summer Bioengineering Conference*,

- pages V01AT07A004–V01AT07A004. American Society of Mechanical Engineers, 2013.
107. V. Quaranta, A. M. Weaver, P. T. Cummings, and A. R. A. Anderson. Mathematical modeling of cancer: The future of prognosis and treatment. *Clinica Chimica Acta*, 357:173–179, 2005.
 108. I. Ramis-Conde, M. A. Chaplain, and A. Anderson. Mathematical modelling of cancer cell invasion of tissue. *Mathematical and Computer Modelling*, 47(5–6):533 – 545, 2008. Towards a Mathematical Description of Cancer: Analytical, Numerical and Modelling Aspects.
 109. T. Ricken, A. Schwarz, and J. Bluhm. A triphasic model of transversely isotropic biological tissue with applications to stress and biologically induced growth. *Computational materials science*, 39(1):124–136, 2007.
 110. H. L. Rocha, E. A. B. F. Lima, and R. C. Almeida. An agent based model of the avascular tumor growth. Congresso Latino Americano de Biomatemática - SOLABIMA (in portuguese), 2015.
 111. A. Roniotis, K. Marias, V. Sakkalis, G. D. Tsibidis, and M. Zervakis. A complete mathematical study of a 3d model of heterogeneous and anisotropic glioma evolution. In *Engineering in Medicine and Biology Society, 2009. EMBC 2009. Annual International Conference of the IEEE*, pages 2807–2810. IEEE, 2009.
 112. T. Roose, P. A. Netti, L. L. Munn, Y. Boucher, and R. K. Jain. Solid stress generated by spheroid growth estimated using a linear poroelasticity model. *Microvascular research*, 66(3):204–212, 2003.
 113. R. E. Rudd and J. Q. Broughton. Coarse-grained molecular dynamics and the atomic limit of finite elements. *Physical Review B*, 58(10):R5893–R5896, 1998.
 114. M. Rybinski. Analysis of mathematical models of signalling pathways. *Uniwersytet Warszawski, Master Thesis*, 2008.
 115. A. Saltelli, K. Chan, and E. Scott. *Sensitivity Analysis*. Number no. 2008 in Wiley paperback series. Wiley, 2009.
 116. S. Schnell, R. Grima, and P. Maini. Multiscale modeling in biology new insights into cancer illustrate how mathematical tools are enhancing the understanding of life from the smallest scale to the grandest. *American Scientist*, 95(2):134–142, 2007.

117. T. N. Seyfried, R. Flores, A. M. Poff, D. P. D'Agostino, and P. Mukherjee. Metabolic therapy: A new paradigm for managing malignant brain cancer. *Cancer Letters*, 356(2, Part A):289 – 300, 2015. Cancer Metabolism.
118. L. Shilkrot, R. Miller, and W. Curtin. Coupled atomistic and discrete dislocation plasticity. *Physical review letters*, 89(2):025501, 2002.
119. L. Shilkrot, R. E. Miller, and W. A. Curtin. Multiscale plasticity modeling: coupled atomistics and discrete dislocation mechanics. *Journal of the Mechanics and Physics of Solids*, 52(4):755–787, 2004.
120. A. S. Shirazi. Hierarchical self-organized learning in agent-based modeling of the MAPK signaling pathway. In *IEEE Congress on Evolutionary Computation*, CEC, pages 2245 – 2251, New Orleans, LA, 2011. IEEE.
121. S. M. B. Shrestha, G. Joldes, A. Wittek, and K. Miller. Modeling three-dimensional avascular tumor growth using lattice gas cellular automata. In *Computational Biomechanics for Medicine*, pages 15–26. Springer, 2014.
122. I. M. Sobol'. Sensitivity estimates for nonlinear mathematical models. *Matematicheskoe Modelirovanie*, 2:112–118, 1990.
123. I. M. Sobol'. Sensitivity analysis for non-linear mathematical models. *Mathematical Modeling and Computational Experiment*, 1:407–414, 1993.
124. C. L. Stokes and D. A. Lauffenburger. Analysis of the roles of microvessel endothelial cell random motility and chemotaxis in angiogenesis. *Journal of Theoretical Biology*, 152:377–403, 1991.
125. T. Stylianopoulos, J. D. Martin, V. P. Chauhan, S. R. Jain, B. Diop-Frimpong, N. Bardeesy, B. L. Smith, C. R. Ferrone, F. J. Hornicek, Y. Boucher, et al. Causes, consequences, and remedies for growth-induced solid stress in murine and human tumors. *Proceedings of the National Academy of Sciences*, 109(38):15101–15108, 2012.
126. T. Stylianopoulos, J. D. Martin, M. Snuderl, F. Mpekris, S. R. Jain, and R. K. Jain. Coevolution of solid stress and interstitial fluid pressure in tumors during progression: Implications for vascular collapse. *Cancer research*, 73(13):3833–3841, 2013.

127. S. Sun, M. F. Wheeler, M. Obeyesekere, and C. W. Patrick Jr. A deterministic model of growth factor-induced angiogenesis. *Bulletin of Mathematical Biology*, 67:313–337, 2005.
128. S. Sun, M. F. Wheeler, M. Obeyesekere, and C. W. Patrick Jr. Nonlinear behaviors of capillary formation in a deterministic angiogenesis model. *Nonlinear Analysis*, 63:e2237–e2246, 2005.
129. R. Sunyk and P. Steinmann. On higher gradients in continuum-atomistic modelling. *International Journal of Solids and Structures*, 40(24):6877–6896, 2003.
130. M. A. Swartz and A. W. Lund. Lymphatic and interstitial flow in the tumour microenvironment: linking mechanobiology with immunity. *Nature Reviews Cancer*, 12(3):210–219, 2012.
131. C. S. Szot, C. F. Buchanan, J. W. Freeman, and M. N. Rylander. Collagen 1 hydrogels as a platform for in vitro solid tumor development. *Biomaterials*, 32(32):7905–7912, 2011.
132. C. S. Szot, C. F. Buchanan, J. W. Freeman, and M. N. Rylander. In vitro angiogenesis induced by tumor-endothelial cell co-culture in bilayered, collagen i hydrogel bioengineered tumors. *Tissue Engineering Part C*, 19(11):864–874, 2013.
133. TACC. Texas advanced computing center, 2008-2015. URL <http://www.tacc.utexas.edu/>.
134. E. B. Tadmor, M. Ortiz, and R. Phillips. Quasicontinuum analysis of defects in solids. *Philosophical Magazine A*, 73(6):1529–1563, 1996.
135. S. M. Tan, C. Fox, and G. Nicholls. Lecture notes on inverse problems, 2005. Physics 707, Auckland University, New Zealand.
136. W. Y. Tan and C. W. Chen. Stochastic modeling of carcinogenesis: Some new insights. *Mathematical and Computer Modelling*, 28:49–71, 1998.
137. A. Tarantola. *Inverse Problem Theory and Methods for Model Parameter Estimation*. SIAM, 2005.
138. R. Thomas. Boolean formalization of genetic control circuits. *Journal of Theoretical Biology*, 42:5639 – 585, 1973.

139. R. D. M. Travasso, E. C. Poire, M. Castro, J. C. Rodriguez-Manzanegue, and A. Hernandez-Machado. Tumor angiogenesis and vascular patterning: A mathematical model. *PLoS ONE*, 6(5), 2011.
140. N. Tustison, M. Wintermark, C. Durst, and B. Avants. Ants andarboles. *Multimodal Brain Tumor Segmentation*, page 47, 2013.
141. E. Van der Giessen and A. Needleman. Discrete dislocation plasticity: a simple planar model. *Modelling and Simulation in Materials Science and Engineering*, 3(5):689, 1995.
142. C. Voutouri, F. Mpekris, P. Papageorgis, A. D. Odysseos, and T. Stylianopoulos. Role of constitutive behavior and tumor-host mechanical interactions in the state of stress and growth of solid tumors. *PloS one*, 9(8):e104717, 2014.
143. D. C. Wallace. A mitochondrial paradigm of metabolic and degenerative diseases, aging, and cancer: A dawn for evolutionary medicine. *Annual Review of Genetics*, 39:359 – 407, 2005.
144. R. Wang, A. Saadatpour, and R. Albert. Boolean modeling in systems biology: an overview of methodology and applications. *Physical Biology*, 9:055001 (14pp), 2012.
145. Z. Wang, L. Zhang, J. Sagotsky, and T. S. Deisboeck. Simulating non-small cell lung cancer with a multiscale agent-based model. *Theoretical Biology & Medical Modelling*, 4:50, 2007.
146. Z. Wang, C. M. Birch, and T. S. Deisboeck. Cross-scale sensitivity analysis of a non-small cell lung cancer model: Linking molecular signaling properties to cellular behavior. *Biosystems*, 92(3):249 – 258, 2008.
147. Z. Wang, C. M. Birc, L. Zhang, J. Sagotsky, and T. S. Deisboeck. Cross-scale, cross-pathway evaluation using an agent-based non-small cell lung cancer model. *Bioinformatics*, 25(18):2389–2396, 2009.
148. R. Winkler. *An Introduction to Bayesian Inference and Decision*. Probabilistic Publishing, 2003.
149. D. Wirtz, K. Konstantopoulos, and P. C. Searson. The physics of cancer: the role of physical interactions and mechanical forces in metastasis. *Nature Reviews Cancer*, 11(7):512–522, 2011.

150. S. M. Wise, J. S. Lowengrub, H. Frieboes, and V. Cristini. Three-dimensional multispecies nonlinear tumor growth - I model and numerical method. *Journal of Theoretical Biology*, 253:524– 543, 2008.
151. S. M. Wise, J. S. Lowengrub, and V. Cristini. An adaptive multi-grid algorithm for simulating solid tumor growth using mixture models. *Mathematical and Computer Modelling*, 53:1–20, 2011.
152. M. Wu, H. B. Frieboes, S. R. McDougall, M. A. Chaplain, V. Cristini, and J. Lowengrub. The effect of interstitial pressure on tumor growth: coupling with the blood and lymphatic vascular systems. *Journal of theoretical biology*, 320:131–151, 2013.
153. S. Xiao and T. Belytschko. A bridging domain method for coupling continua with molecular dynamics. *Computer methods in applied mechanics and engineering*, 193(17):1645–1669, 2004.
154. D. Xiu. *Numerical Methods for stochastic computations: a spectral method approach*. Pinceton University Press, 2010.
155. S. Zhang, R. Khare, Q. Lu, and T. Belytschko. A bridging domain and strain computation method for coupled atomistic–continuum modelling of solids. *International Journal for Numerical Methods in Engineering*, 70(8):913–933, 2007.

